Exploring the Safety Margin in Current Guidelines for Electromagnetic Exposure

Fatemeh Adibzadeh

Colofon:

The investigations presented in this thesis were carried out at the Department of Radiation Oncology, Erasmus MC - Daniel den Hoed Cancer Center, Rotterdam.

This research was financially supported by The Netherlands Organization for Health Research and Development (ZonMw). Financial support for the printing of this thesis was provided by ZonMw and the Erasmus University Rotterdam.

Address for correspondence:
F. Adibzadeh, Department of Radiation Oncology: Unit Hyperthermia, Erasmus MC Daniel den Hoed Cancer Center, PO box 5201, 3008AE Rotterdam, The Netherlands.
f.adibzadeh@erasmusmc.nl

ISBN: 978-94-6295-551-6

Printed by: Proefschriftmaken.nl, Uitgeverij BOXPress

Exploring the Safety Margin in Current Guidelines for Electromagnetic Exposure

Onderzoek naar de grootte van de veiligheidsmarge van de huidige blootstellingslimieten voor Elektromagnetische velden

Doctoral dissertation

for the purpose of being admitted to the degree of Doctor at
Erasmus University Rotterdam
on the authority of the
rector magnificus

Prof.dr. H.A.P. Pols

and in accordance with the decision of the Doctorate Board.

The public defence ceremony shall take place on
thursday 23 march 2017 at 15:30

by

Fatemeh Adibzadeh

born in Tehran, Iran

Erasmus University Rotterdam

Doctoral committee

Supervisor:	Prof.dr.ing. G.C. van Rhoon
Other members:	Prof.dr. R. Kanaar
	Prof.dr.ir. A. Burdorf
	Prof.dr.ir. A.P.M. Zwamborn
Co-supervisor:	Dr.ir. M.M. Paulides

Contents

CHAPTER 1

Introduction

1.1 Background

Electromagnetic fields (EMF) have been a vital part of our daily life for over a century now and their application in society is still increasing. EMF continuously surround us and are generated by many different sources in various situations like domestic devices, telecommunication systems, electric power transmission lines, but also in medical applications such as Magnetic Resonance Imaging (MRI), transcranial magnetic stimulation in psychological disorders, deep brain stimulation in Parkinson disease and hyperthermia treatment of cancer. The rapid increase worldwide in the use of EMF results in an increased awareness of the general public for the risks associated to exposure to EMF, which raised concerns about possible adverse health effects associated to exposure at the currently applied levels. In response to these public concerns, in 2006 the Dutch government initiated a research program on electromagnetic fields and health (EMF&H). The research presented in this thesis is performed within the framework of this program and was aimed at investigating the appropriateness of the currently applied safety limits in relation to the changes in organ functionality under controlled conditions and at well quantified exposure levels.
The current guidelines for maximum human exposure to EMF have been defined by the International Commission on Non-Ionizing Radiation Protection (ICNIRP) and the Institute of Electrical and Electronics Engineers (IEEE). These guidelines define basic restrictions (BRs) that protect against established adverse effects due to whole-body or partial body exposure to EMF. The BRs are conservative, i.e. incorporate large safety factors, to assure that threshold dose levels, at which biological effects have been established, are not exceeded. However, the selection of safety factors is an arbitrary process based on expert opinion rather than a rigorous quantitative process. In addition, the magnitude of the actual safety margin for various exposure scenarios is unknown since these exposure limits and safety factors have been obtained by animal experiments or from assessments that approximated the human anatomy by simple shapes and homogeneous materials. Therefore, it is questionable if the exposure limits are adequate or over restrictive. If over restrictive, this would imply that the limits can be increased for improving the functionality of the exposure purpose, e.g. EMF based diagnosis or therapy.

1.2 Electromagnetic exposure and health effects

To understand the biological effects of electromagnetic (EM) radiation, we should first understand the difference between ionizing radiation and non-ionizing radiation (Figure 1.1). Ionizing radiation is radiation that carries enough energy to remove an electron from an atom or molecule, thereby ionizing them. The Deoxyribonucleic acid (DNA) molecule of living cells is always susceptible to damage by ionizing radiation. Non-ionizing radiation refers to any class of electromagnetic radiation that does not carry enough energy to ionize. Still non-ionizing radiation excites the motion of the atoms or molecules when absorbed by matter.

The work described in this thesis is limited to localized exposure of humans to non-ionizing electromagnetic fields at the radio frequency (RF) spectrum, that is 100kHz to 3 GHz.

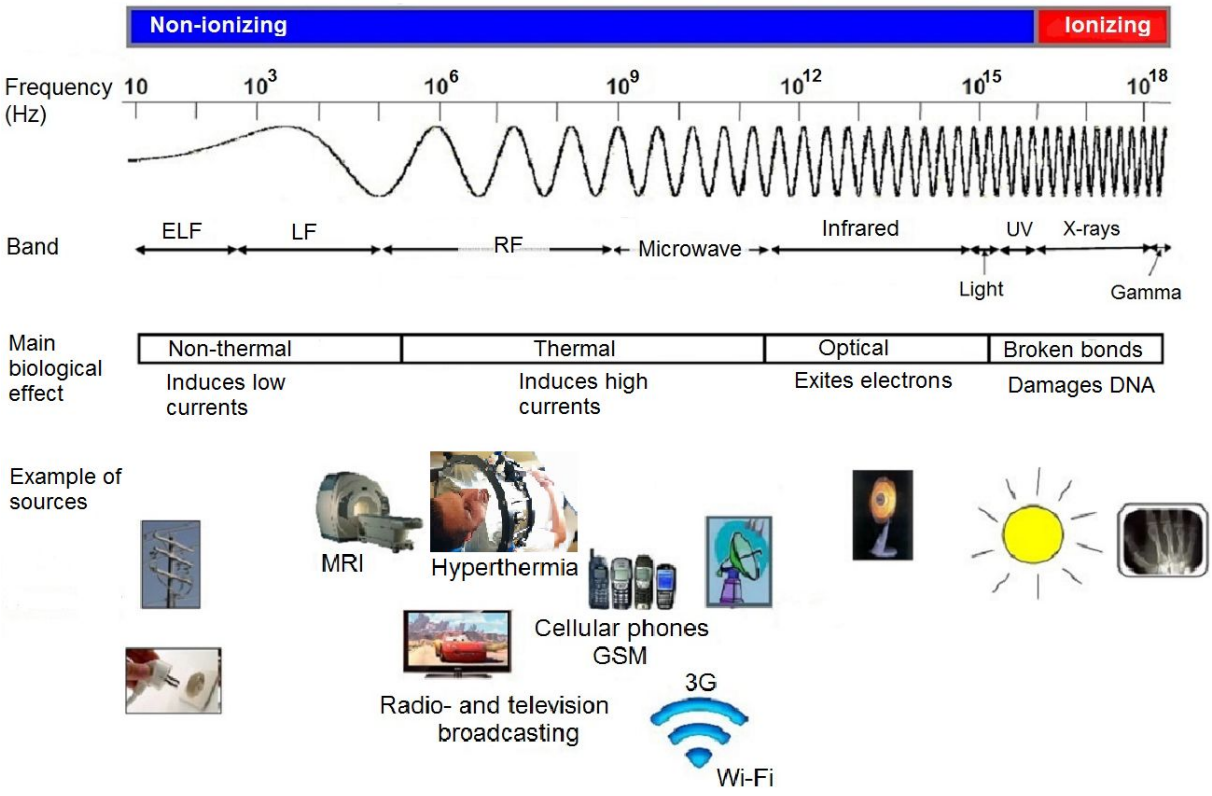

Figure 1.1: Electromagnetic spectrum classification, the associated biological effects and examples of exposure sources. Created using elements taken from www.wikipedia.org

1.2.1 Interaction mechanism

The interaction of EMF with materials, e.g. human tissues, depends on their frequency. In the RF range, the EMF energy absorption and subsequent tissue heating becomes the major mechanism[89].

RF EMF energy absorption is based on oscillating mechanical forces on electric charged particles or electric dipoles generated by the electric component, and, generated by the magnetic field component on particles with an inherent magnetic moment[88]. Depending on the particles mass and mobility, these forces may cause translatory, oscillatory and/or rotatory movement and hence conversion of field energy to particles kinetic energy. Particles kinetic energy is then distributed inside the material by collision with

other particles, hence causing irregular particle movement that on a macroscopic scale is phrased as "heat" (Browns molecular movement) and quantified by the physical term temperature.
A detailed description of bio-electromagnetics can be found for example in Durney[23].

1.2.2 Health effects of RF EMF

In 2011, the Working group at the International Agency for Research on Cancer (IARC) reviewed many studies regarding associations between use of wireless phones and glioma to assess the carcinogenicity of RF EMF. Overall, the Working Group concluded that there is "limited evidence" for the carcinogenicity of RF EMF. In view of the limited evidence in humans and in experimental animals, the Working Group classified RF EMF as "possibly carcinogenic to humans" (Group 2B)[27]. Most recently, the results of the major US National Toxicology Program (NTP) animal research project on the effects of chronic exposures to mobile phone signals were made public and an increased occurrence of malignant gliomas in the brain and schwannomas of the heart in male rats chronically exposed to RF EMF was reported[109]. The authors say, "These findings appear to support the IARC conclusions regarding the possible carcinogenic potential" of RF EMF. However, these effects were not observed in female rats and exposed male and female rats lived longer than the controls. This study is currently under review and the results are far from definitive at this point. Even before the IARC started its project, the EMF Committee of the Health Council of the Netherlands initiated a systematic analysis of the epidemiogical literature on this subject. Its conclusions are slightly different from those of IARC. The Committee concludes that from this evidence there is no established association between long-term and frequent use of a mobile telephone and an increased risk for tumors in the brain or head and neck. Such association can however also not be excluded. The Committee considers it unlikely that exposure to RF EMF associated with the use of mobile phones, causes cancer. At present, there is still much uncertainty and contradiction about the health risk of EMF and probably this confusion in both scientific and public community will not disappear on short notice.
Current guidelines for limiting RF EMF exposure have been developed only based on "established" effects. An established adverse health effect is referred to a biological effect characterized by a harmful change in health that is supported by consistent findings of that effect in studies published in the peer-reviewed scientific literature. The effect must be confirmed with evidence being demonstrated by independent laboratories and consensus in the scientific community that the effect occurs for the specified exposure conditions. To date, the only established effect attributed to RF EMF exposure is the acute thermal effect. The majority of studies that reported non-thermal effects were performed at high levels of RF exposure and it cannot be exclude that the effects observed are not the result of heating and elevated temperature[57]. The few studies that reported effects at low (non-thermal) exposure levels, i.e. below the recommended limits, are inconsistent and/or are counterweighted by the larger body of evidence reporting no effects at these exposure levels. In addition, many of these experiments have serious shortcomings in the dosimetry,

exposure control and technical lay-out.

1.2.3 Basic restrictions and safety factor

In accordance to IEEE* (2005)[57] and ICNIRP† (1998)[55], restrictions on exposure to time-varying electric, magnetic, and electromagnetic fields are termed "basic restrictions (BRs)". These restrictions are based on established acute health effects and biological considerations. Protection against acute health effects should be assured if the dose inside the human body does not exceed the basic restrictions. Depending upon the frequency of the field, the physical quantities used to specify these restrictions are magnetic flux density, current density, specific absorption rate (SAR), and power density. For the RF range, the limits are given in SAR and follow the ICNIRP guidelines from 1998[55] (Table 1.1). The basis for the the BRs for localized exposure (Table 1.1) is to limit induced temperature rise below 1°C over 30 minutes in any part of the body for all exposure scenarios.

Table 1.1: Basic restrictions for localized exposure at frequencies between 100 kHz and 3 GHz.*

	General public exposure Localized SAR (W/kg)	Occupational exposure Localized SAR (W/kg)
Head and Trunk	2	10
Extremities and pinnae	4	20

* Note:
1. All SAR values are to be averaged over any 6-min period.
2. Localized SAR averaging mass is any 10 g of tissue (defined as a tissue volume in the shape of a cube); the maximum SAR so obtained should be the value used for the estimation of exposure.
3. The extremities are the arms and legs distal from the elbows and knees, respectively.

In establishing the basic restrictions, large safety factors are employed to avoid any acute health effects during exposure with a sufficiently wide margin to account for uncertainty in the scientific data and interpersonal variability. The term "safety factor" is commonly interpreted to be the ratio of an exposure level causing an adverse effect to the corresponding defined exposure limit. For example, a whole-body averaged SAR (SAR_{wb}) of 4 W/kg for 30 minutes in an RF exposure experiment has been shown to induce a whole-body temperature increase of 1°C which can have adverse health effects such as heat exhaustion

*Institute of Electrical and Electronics Engineers
†International Commission for Non-Ionizing Radiation Protection

and heat stroke[76]. A traditional safety factor of 10 has been applied to this established SAR level, resulting in a SAR_{wb} of 0.4 W/kg for the basic restrictions concerning occupational environment, see Figure1.2. The occupational population consists of trained adults under controlled conditions whereas general public consists of individuals of all ages and various health status. Therefore, more strict restrictions for the public than for the occupational population is considered, i.e. an additional safety factor of 5 for the public. The tolerable SAR level for localized exposure is much larger than the SAR limit for a whole-body exposure. Experimental studies in the late 1970's have shown that the peak SAR in a biological body can be more than 20 times higher than the SAR_{wb} [38,42,44] with the same safety factor presumed but not verified or demonstrated to exist for whole-body exposure. These data form the basis for the localized SAR restrictions. It is believed that for localized RF exposure, these standards incorporate at least a safety factor of 10 and probably considerably more if the remarkable tolerance in human studies[1] is accepted as generally valid. However, the magnitude of the safety factors, as ratio between the level of local SAR that causes adverse effect and the BRs, are not known and quantified for various *localized* exposure scenarios.

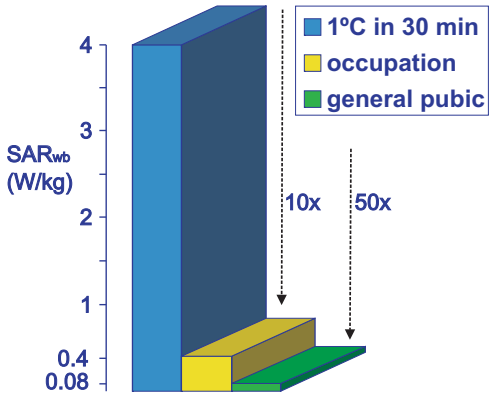

Figure 1.2: Illustration of lowering the established adverse effect SAR level to the defined SAR limits in the guidelines by applying safety factors on whole-body averaged specific absorption rate (SAR_{wb}), as an example. (Source: J.F.Bakker, 2012. *Dosimetry of exposure to electromagnetic fields in daily life and medical applications*. PhD Thesis, Erasmus MC.).

1.2.4 EMF Dosimetry

EMF Dosimetry is the assessment of the absorbed dose in tissue induced from exposure to EMF. The dose is measured, or predicted by computational simulations in quantities such as electric fields, SAR or temperature increase.
According to ICNIRP and IEEE guidelines, accurate dosimetry is essential for meaningful investigations for biological effects of EMF, since even uniform exposures lead to non-uniform absorption in almost all in-vivo and in-vitro exposure situations. Many studies in literature suffer from lack of scientific detail, defective measurements and inadequate

dosimetry. Absence of dosimetry makes a study impossible to evaluate, or replicate at comparable levels. Hence, while of interest, these studies cannot be applied to setting standards for maximum allowable human exposure to RF energy.
Dosimetry has become very reliable and successful by developments in numerical methods of calculation, e.g. the finite-difference time-domain (FDTD) technique, and by improvements in creating human models based on detailed MRI scans from the human anatomy. Advanced simulation tools can be used to estimate the induced SAR and temperature doses following RF energy deposition in human tissue. It is important to investigate the uncertainty associated with dosimetry when predicting the induced dose in tissues. Uncertainty is defined as the amount by which the estimated value may depart from the true value due to the uncertainties in input modelling parameters such as dielectric and thermal tissue properties and model discretization on the dosimetric results.

1.3 Topics of this thesis

The goal of this thesis is to explore the relevance of the current basic restrictions for functional tissue changes and to define SAR values for localized RF EMF exposure in different controlled scenarios above which tissue damage takes place.
This project[‡] started at Erasmus MC jointly with Technical University of Eindhoven (TU/e) in response to increasing public concern about potential adverse health effects of electromagnetic fields. The project was aimed to investigate possible hazardous impact of electromagnetic fields on humans by providing high quality dosimetric assessment.
Therefore, as a first step, we verified the dose accuracy in the studies that reported adverse health effects at the recommended level of EM exposure, i.e. below the maximum allowable exposure. Among various possible health effects, the risk of inducing brain cancer from exposure to mobile phone radiation has the strongest interest of laymen and health organizations. Some epidemiological studies on mobile phone RF EMF exposure raised questions regarding an increased risk of glioma in heavy users of mobile phones[11,12]. However, the investigation of risk of brain cancer associated with mobile-phone use poses complex methodological challenges in the conduct of the research and in the analysis and interpretation of the findings. The RF exposure assessments in the brain in those studies was based on a simple homogeneous phantom that approximated the human head morphology. In this thesis, we hypothesized that such an approach is bound to a large uncertainty in the assignment of the exposure level on an individual person. We showed that individual head morphology is highly diverse and therefore morphological variation should be taken as an important source of uncertainty into account to calculate an accurate dose estimation in the brain, .
As next steps, we retrospectively performed dose-effect relations studies at exposure levels above the guidelines for the brain and eyes, i.e. critical organs when determining safety guidelines for RF radiation. These organs receive a considerable dose of RF radiation during hyperthermia treatment of cancer in head and neck region. Hyperthermia (HT),

[‡]supported by the Netherlands Organization for Health Research and Development (ZonMw)

a powerful cancer treatment modality, which applies prolonged (60 minutes) intense RF energy to increase tumor temperature towards 40 to 44°C, is an example of a therapeutic application where potential acute effects of EMF on humans can be observed. This thesis shows that while exceeding the basic restrictions by up to at least 10 (brain[2]) and 14 (eyes[3]) times, no indication for any serious acute effect was found. Therefore, as a final step, the concept of functional SAR limits was developed to help decision making on how much the local SAR can be increased before acute effects take place.
The goal of this thesis was accomplished by quantifying the safety factor included in the basic restrictions and developing a concept for functional SAR limits for various localized exposure scenarios. The safety factors were calculated as a ratio between functional SAR limits, based on the lowest thermal dose required to induce tissue damage reported in the literature, and the basic restrictions. The numerical results demonstrate that the margin of safety in the current basic restrictions for localized exposure is large.

1.4 Outline of this thesis

Chapter 2 describes the assessment of the impact of head morphology on the induced local SAR in the brain from exposure to mobile phone radiation (below the basic restrictions).

Chapter 3 describes the evaluation of the conservativeness of the basic restrictions by retrospectively relating the induced EM dose in the human brain to the scored acute health effects from exposure to prolonged intense RF EMF during head and neck hyperthermia.

Chapter 4 describes the evaluation of the conservativeness of the basic restrictions by retrospectively relating the induced EM and thermal dose in the human eyes to the scored acute health effects from exposure to prolonged intense RF EMF during head and neck hyperthermia.

Chapter 5 describes the quantification of the incorporated safety factors in the basic restrictions by providing functional SAR thresholds associated to the thermal dose limits above which thermal tissue damage occur.

Chapter 6 provides the general conclusions and future perspectives.

CHAPTER 2

Impact of head morphology on the local brain specific absorption rate from exposure to mobile phone radiation

This chapter is based on:
F Adibzadeh,JF Bakker, MM Paulides, RF Verhaart and GC van Rhoon. Impact of Head Morphology on Local Brain Specific Absorption Rate from Exposure to Mobile Phone Radiation.
Bioelectromagnetics, Vol. 36(1), pp. 66-76, 2015.

Abstract

Purpose: *Among various possible health effects of mobile phone radiation, the risk of inducing cancer has the strongest interest of laymen and health organizations. Recently, the Interphone epidemiological study investigated the association between the estimated Radio Frequency (RF) dose from mobile phones and the risk of developing a brain tumor. Their dosimetric analysis included over 100 phone models but only two homogeneous standard head phantoms. So, the potential impact of individual morphological features on global and local RF absorption in the brain was not investigated. In this study, we performed detailed dosimetric simulations for 20 head models and quantified the variation of RF dose in different brain regions as a function of head morphology.* ***Materials and methods:*** *Head models were exposed to RF fields from generic mobile phones at 835 MHz and 1900 MHz in the 'tilted' and 'cheek' positions. To evaluate the local RF dose variation, we used and compared two different post-processing methods, i.e. the Talairach and field-sensor methods.* ***Results:*** *The results show that the variation in the averaged specific absorption rate (SAR) among the heads can reach up to 16.4 dB at a 1 cm^3 cube inside the brain (field-sensor method) and alternatively up to 15.8 dB in the medulla region (Talairach method). The maximum variation of 10g peak spatial SAR ($psSAR_{10g}$) was around 4 dB in the head and 7 dB in the brain.* ***Conclusions:*** *In conclusion, we point head morphology as an important uncertainty source for dosimetric studies of mobile phones. Therefore, any dosimetric analysis dealing with RF dose at a specific region in the brain (e.g. tumor risk analysis) should be based upon real morphology.*

2.1 Introduction

The possible health effects of mobile phone radio frequency (RF) exposure are subject of an ongoing debate in several scientific studies. Because brain tumor incidence has drawn the most attention, epidemiological approaches are being used to investigate the potential association between mobile phone RF exposures and the risk for developing brain tumors. The largest and the most recent study was the Interphone study[11,12], in which Cardis and her colleagues analyzed the risk for brain tumors as the total cumulative specific RF energy, or dose, absorbed at the tumor locations. By taking more parameters into account (e.g. telephone type, network characteristics, and amount and conditions of phone use), they greatly improved on the dose estimation provided by the previous Japanese Interphone study[93]. However, the shortcoming of the Interphone study is that dosimetric measurements were limited to two generic head phantoms, which excluded the potential impact of head morphological differences on the RF dose in the brain.

Morphological differences in models is an important source of variation as it has been illustrated in several studies which employed more than one human model, e.g. (Hirata et al 2007, Buccella et al 2007).
The main objective of our study was to investigate the variation in averaged specific absorption rate (SAR) in specific brain-regions due to morphological changes, i.e. changes in head size and shape. To be able to quantify the relative importance of morphology compared to other previously investigated dosimetric uncertainty sources (e.g. type of the mobile phone, phone positioning, age-dependent dielectric properties and pinna thickness), we also assessed the variation in 10g peak spatial-averaged SAR ($psSAR_{10g}$) in the brain and head. Finally, additional simulations with altered settings were used to assess the expanded numerical uncertainty of the results.

2.2 Materials and methods

In this study, detailed dosimetric simulations were performed using SEMCAD X*. We used and compared two different methods to evaluate the local RF dose variation from exposure to generic mobile phones at 835 and 1900 MHz and for 'tilted' and 'cheek' positions. First, we assessed the averaged SAR over various brain regions. Second, we compared the SAR of each specific region between 20 head models and calculated the SAR variation. Third, we assessed the influence of morphology on $psSAR_{10g}$ which is the frequently used parameter in mobile phone dosimetric studies. Finally, to investigate the overall uncertainty of the numerical modeling, we determined the influence of various modeling parameters on the obtained result (in terms of $psSAR_{10g}$).

2.2.1 Anatomical head models

Anatomical head models of 20 patients, including 13 males and 7 females, were obtained from Computed Tomography (CT) images (imaging resolution ranging from 0.58x0.58x1.5 mm^3 to 0.97x0.97x2.5 mm^3). Each set of CT images was segmented into nine different tissue types (air, bone, fat, muscle, brain, spinal cord, eye, cartilage and lung) with the segmentation protocol as described in[98], using iSeg†. Note that with this protocol the brain was segmented as one homogeneous tissue.
Table 2.1 includes more detailed information on the physical characteristics of the head models relative to human variation. To avoid the impact of imaging methods e.g. CT vs magnetic resonance imaging (MRI) and to have an equal number of segmented tissues for all models, we did not include other models (e.g. Virtual Family models). Hence, number and types of tissues as well as the assigned properties were the same for all of the models.

*SEMCAD X EM Simulation, version 14.8.4 (www.semcad.com).
†iSeg version 3.5 (www.zurichmedtech.com/products/sim4life/iseg/iseg/).

Table 2.1: Physical characteristics of the anatomical head models in this study with comparison to literature values ([4] and [84]).

	Brain vol		ANT 1*		ANT 2**		ANT 3***		Subjects	
	Avg	std	Avg	std	Avg	std	Avg	std	Sex	Age
Poston 2000	-	-	21.4	0.8	22.5	0.9	14.0	0.6	2208 F 1774 M	17%≤20 21≤57%≤30 17%≤20
Allen 2002	1.2	0.1	-	-	-	-	-	-	23 F 23 M	Avg=32.1 std=8.8
This study	1.4	0.1	22.2	0.6	20.7	0.9	15.4	0.5	7 F 13 M	Avg=61.8 std=11.1

Head Anthropometry (ANT):
*Pronasale to back of head **Menton to top of head ***Bitragion breadth
Dimensions:
Brain vol.: (l), ANT: (cm), Age: (yr)

2.2.2 Phone models

The generic mobile phone model and the positioning procedure of the phone against the anatomical heads were as defined in[60], in which the authors defined the standard 'cheek' and 'tilted' phone positions for anatomical head models by determining reference points and reference planes based only on the anatomical characteristics of the head model (Figure 2.1). The phone was modeled as a flat metallic plate representing the printed circuit board (PCB) inside a plastic box, and a mono-pole antenna. For generality, details of real phones were not included.

2.2.3 Electromagnetic modeling

The dielectric properties of tissues were assigned to the segmented tissues according to the ITIS material parameter database*[48]. The dielectric property of the homogeneous brain was set to the average for the white matter, grey matter and cerebellum. The brain permittivity and conductivity were equal to 47.94 and 0.80 (S/m) respectively at 835 MHz and equal to 45.44 and 1.27 (S/m) at 1900 MHz. For all evaluations we used the finite difference time domain (FDTD) solver of SEMCAD X. The mesh resolution was between 0.5 mm and 2 mm for the head region and up to 12 mm in air. For all simulations the mobile phone was fixed and aligned with the grid, and the head model was rotated to obtain 'cheek' or 'tilted' positions (Figure 2.1). The mobile phone was on the left side of the heads. The antenna was excited by a sinusoidal signal of 10 periods, where steady

*http://www.itis.ethz.ch/database

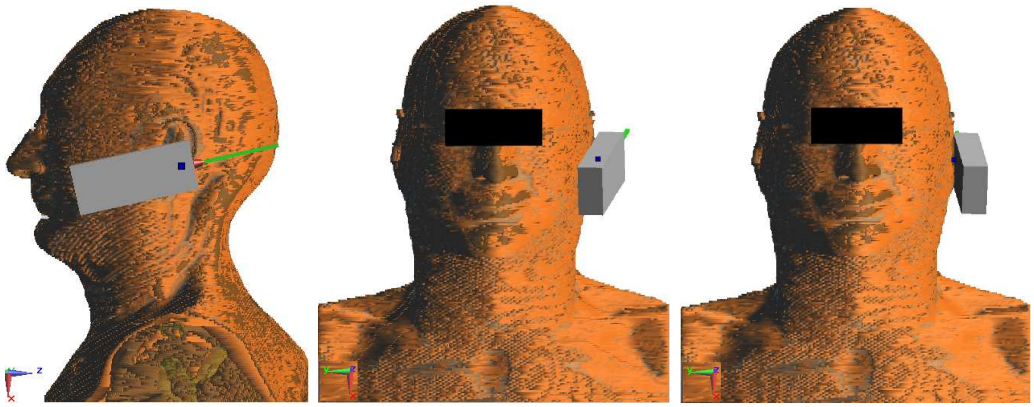

(a) sagittal view (b) cheek (c) tilted

Figure 2.1: Overview of phone positions against the head in (a) sagittal view (b) 'cheek' and (c) 'tilted' positions.

state conditions were reached after 6 periods.

2.2.4 Post processing

For post-processing, we used two different evaluation methods.

Field-sensor

In this method, we placed cube field sensors in the brain of each model, i.e. 16 sensors were used as a compromise between capturing spatial variation in the entire brain and complexity of the analysis. The size and shape of the sensors were selected to match the estimated volume of the tumor-center in[12], which was a $1cm^3$ cube. The rationale for the sensor location was to capture the area where the brain tumor occurrence is more frequent. Therefore, since the number of gliomas located at frontal and temporal lobes are substantially higher than for other lobes in adults[66], we put more field sensors in these regions to increase the probability of capturing the center of a possible tumor. In addition, we put some sensors in other locations (e.g. occipital lobe) to assess the variation in other brain regions as well.
The field sensors were placed inside the brains prior to phone positioning and based on the CT image registration using optimized settings from[28]. Based on this method, we defined the brain of model number 12 as reference, and registered all the other brains to that. As a result, spatial correspondence was obtained between all brain models, meaning that the field sensors were at equivalent locations in the brains. Figure 2.2a shows the location of the sensors in the brain.
We calculated the average SAR in these sensors as total loss divided by the total lossy mass, and compared the result per sensor between all head models.

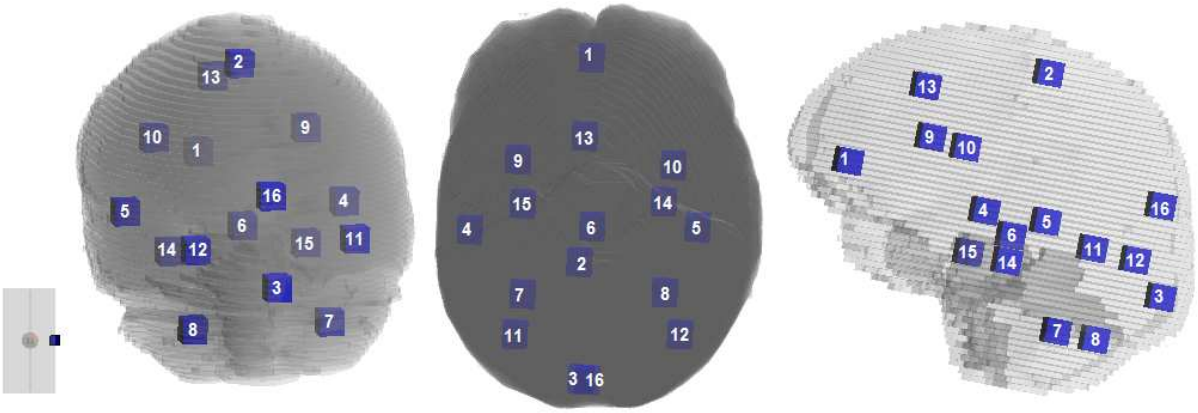

(a) Positions of the field sensors in the brain.

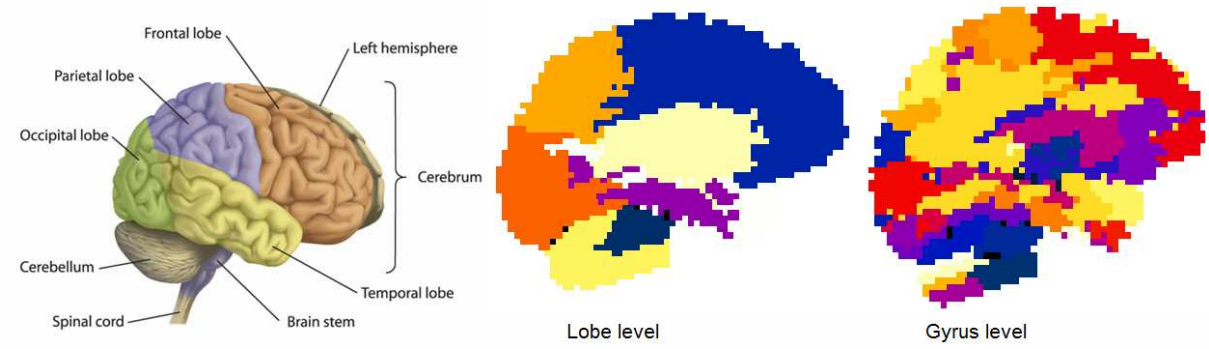

(b) Basic brain anatomy [†]and segmentation of the brain in 'Lobe' and 'Gyrus' levels.

Figure 2.2: Overview of our 2 post-procession methods: (a)field-sensor (b)Talairach.

Talairach atlas

To evaluate the result of field-sensor method and to be able to extend the SAR variation assessment to all brain regions, with different shapes and sizes of the averaging volume we used the Tailarach Atlas tool, available in SEMCAD X package. This tool is based on a set of landmarks for mapping every position in the brain model into the Talairach atlas[67] and vice versa. The location of these landmarks is determined by the brain boundaries and the position of some inner brain structures[16]. Since in the models, detailed brain tissues were not segmented, we aligned and slightly scaled the brain of Duke from the virtual family (VF)[¶] to each brain of our anatomical head models in order to artificially locate the position of some brain tissues to be able to post-process the data. Note that the VF model was inserted after simulation and therefore had no influence on the power absorption in the brain.
The Talairach tool can identify over a thousand different regions in the brain for the

[†]Source: (http://skpascoe.hubpages.com/hub/Know-Your-Loaf)
[¶]http://www.itis.ethz.ch/vip

purpose of characterizing the electromagnetic exposure of anatomical and functional brain regions[16]. It subdivides the brain into 1150 different sub-regions, and, according to each of the five defined levels, assigns a volume occupancy Talairach (VOT) label to each sub-region. For example, according to hemispherical level, 7 labels are assigned to the sub-regions, the lobe level defines 12 labels, the gyrus level 55, the tissue level 3, and the cell level 71. Figure 2.2b provides an overview of the brain subdivision of the lobe and also of the gyrus levels.
For levels like cell or gyrus, the brain sub-regions are small and mapping the location of the Talairach regions is more affected by the EM simulation grid or the brain delineation error[16]. Therefore, we excluded these levels from our analysis and reported the results only for the hemispherical, lobe and tissue levels.
We calculated the variations among the heads for each defined region per Talairach-level.

2.2.5 Additional analyses

Peak spatial-average SAR

The psSAR_{10g} in the head and brain were evaluated in a cubic volume according to the procedure defined in[58]. We derived it directly in SEMCAD X and compared its values between different models.

Numerical uncertainty

To investigate the uncertainty of the numerical modeling, we determined the influence of various modeling parameters on the head psSAR_{10g} for the first model in cheek position and at 835 MHz as defined in[94]. The variation of the outcome was assumed predictive for the overall effect of modeling parameters. The investigated parameters were:
(1) Model discretization: The effect of spatial resolution in the model discretization was investigated by simulating the maximum grid steps between 1.4 mm and 12 mm.
The effect of using a uniform grid step was also investigated by using additional simulations with uniform grid steps of 0.8, 1 and 2 mm.
(2) Absorbing boundary: We investigate the effect of UPML efficiency by changing the level of strength in SEMCAD X (low, medium, high, very high).
(3) Simulation time: Additional periods of the harmonic wave, from 10 periods to 50, were used.
(4) Padding: We increased the padding from $\lambda_{air}/4$ to $\lambda_{air}/2$.
(5) Tissue dielectric properties: The individual tissue properties deviate from the mean literature values proposed by Gabriel[33,36,37]. Different sources are defined for this deviation such as age-dependent, tissue assignment, the 4-Cole-Cole dispersion model[37] uncertainty and post mortal changes. The most effective source however is the age-dependent tissue property variation[6]. Bakker mentioned that although the influence of other sources is unknown, we know that the variations are much smaller than the age-dependent dielec-

tric changes. The influence of age-dependent changes of tissue dielectric properties on $psSAR_{10g}$ for mobile phone exposure was calculated by[13], who used age-dependent dielectrics of grey matter for all brain sub-regions and found that at 900 MHz, the $psSAR_{10g}$ variation is approximately 0.5 dB.
(6) Image resolution: The CT scan of the first head-model ($0.97\times0.97\times2.5$ mm^3) was re-sampled into the resolutions of the other models: $0.97\times0.97\times1.5$, $0.88\times0.88\times2.5$, $0.86\times0.86\times1.5$, $0.76\times0.76\times1.5$, $0.68\times0.68\times1.5$, $0.58\times0.58\times2.5$ and $0.58\times0.58\times1.5$ mm^3.
(7) Segmentation of brain tissues: The influence of detailed brain tissue (grey, white matter and cerebrospinal fluid) segmentation on our results was calculated by comparing the value of head $psSAR_{10g}$ for three of the patients (model number 12, 13 and 14) for whom MR scans were also provided. Thus for each of these three models the difference in $psSAR_{10g}$ was calculated between heterogeneous- versus homogeneous-brain models. The average of the differences is reported in table 2.2.

Table 2.2: Evaluation of the standard combined uncertainty u_c and the expanded uncertainty U of the $psSAR_{10g}$. k is the coverage factor for the confidence interval.

	$psSAR_{10g}$	
	%	dB
Discretization		
(a) non-uniform grid	9.79	0.40
(b) uniform grid	6.56	0.27
Absorbing boundary (ABC)	0.26	0.01
Simulation time	0	0
Padding	0.04	0
Tissue dielectric properties	12.20	0.5
Image resolution	6.15	0.26
Segmentation of brain tissues	0.63	0.03
u_c	16.82	0.67
U (k=2)	33.64	1.26

2.2.6 Quantification parameters

The dosimetric variation is quantified by two parameters, i.e. the coefficient of relative variation (CRV) and the ratio of the maximum to the minimum.
The CRV is the standard deviation of a variable normalized to its mean. This measure is used to give a sense of how large the standard deviation is. (CRV=(std/mean)$\times$100%).

The CRV was selected because it describes the spread of a data distribution. But if the distribution is not gaussian, it does not contain information about the maximum and the minimum of the data values. Therefore, we also report the maximum of the data variation as the ratio of the maximum SAR values divided by the minimum SAR values in dB. (dB=10log(SAR_{max}/SAR_{min}))

2.3 Results

We first report the calculated SAR variations per evaluation method (field-sensor and Talairach). Next we assessed the $psSAR_{10g}$ variation. Finally the results of the uncertainty analyses are demonstrated. The SAR values were normalized to the net input power (1 W).

2.3.1 SAR variation using the field-sensor method

Left plots in Figure 2.3 and Figure 2.4 show the mean and std of the averaged SAR in the inserted field sensors (i.e. $1cm^3$ of brain tissue in 16 different locations); The right plots in the figures show the calculated variation for each field sensor. The figures indicate that variations are higher at 1900 MHz than at 835 MHz. They also show that the SAR values in the brain regions are lower at 1900 MHz compared to 835 MHz which is due to smaller penetration depth at 1900 MHz than 835 MHz. The average and the min-max range of the variations per exposure setup are shown in Figure 2.5. Table 2.3 summarizes Figure 2.3 and Figure 2.4 by providing the amount and location of maximum detected variation.

Table 2.3: The maximum variation in the averaged SAR in different sensors.

Exposure configuration	dB_{max} *	Sensor of dB_{max}	CRV_{max} *	Sensor of CRV_{max}
835 MHz-cheek	16.0	1	78.1	9
1900 MHz-cheek	15.6	16	107.32	16
835 MHz-tilted	15.4	10	93.0	1
1900 MHz-tilted	16.4	16	104.8	16

dB_{max}= maximum of the dB values. CRV_{max}= maximum of the CRV values.

2.3.2 SAR variation using the Talairach method

Figure 2.5 shows the amount of the SAR variation based on the levels defined in the Talairach hierarchy. In order to compare the results of our two post-processing methods, we also included the SAR variations based on the field-sensor method in this figure. Here, the average of the CRV or the dB values over all regions in the brain and the max-min range of the variations between defined regions at each level are indicated. For

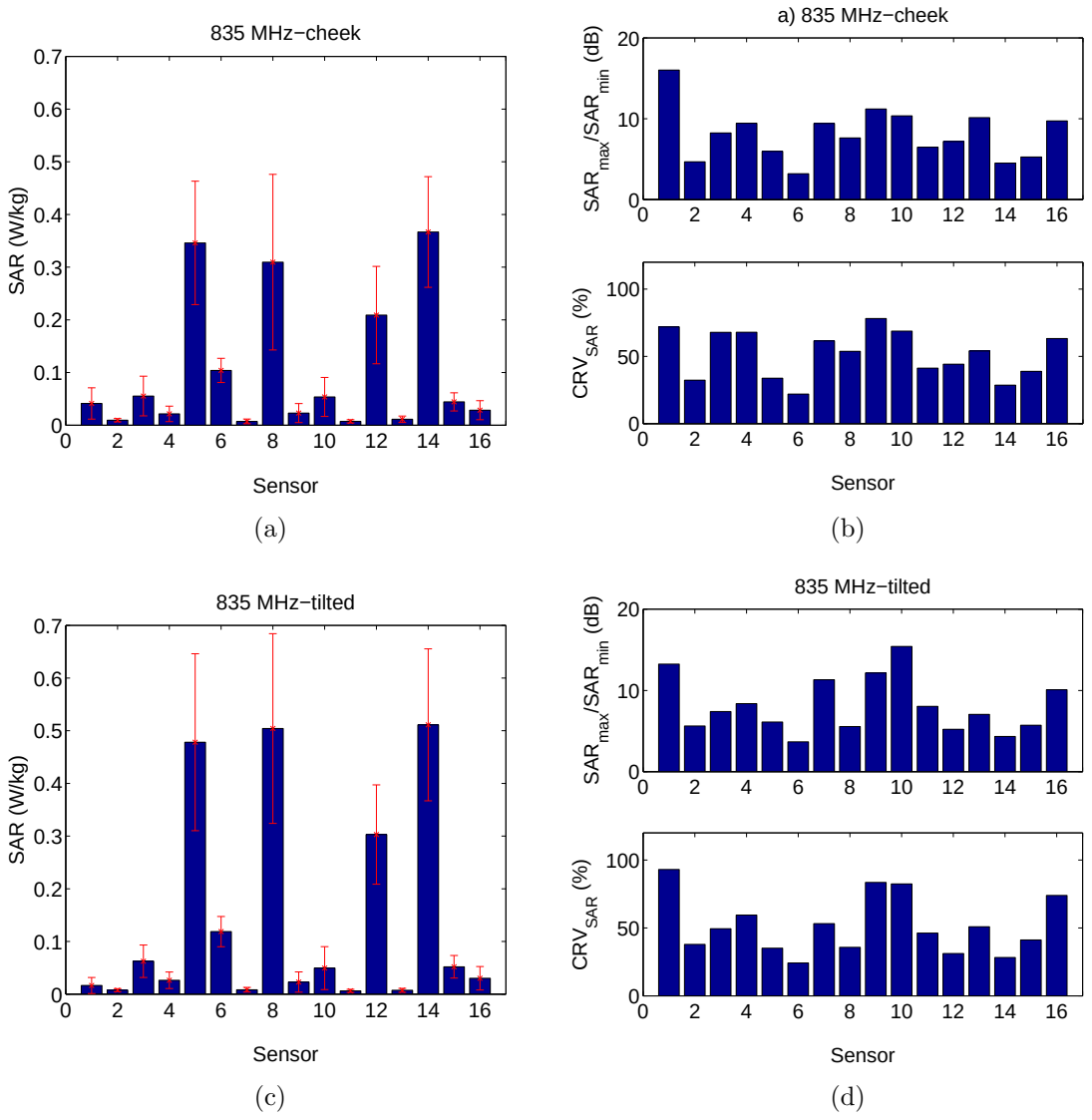

Figure 2.3: Left: Mean and standard deviation of the averaged SAR in the inserted field sensors at 835 MHz; Right: Calculated variations in terms of ratio of (max/min) and CRV (std/mean).

example the bar with square marker at 1900 MHz-cheek configuration indicates that the variations between heads range from 8.20 dB, in 'left Cerebrum' region, to 13.63 dB in 'right Brainstem' region and the average of variations over all brain regions is 10.76 dB (the brain regions in the hemispherical level are left cerebellum, right cerebellum, left cerebrum, right cerebrum, medulla, left brain stem and right brain stem). The differences between the levels in Figure 2.5 and Table 2.4 show that as expected, the amount of SAR variation depends on the size of averaging volume and as shown, by increasing the size (from lobe to tissue levels), the variation will decrease. Figure 2.5 indicates that the

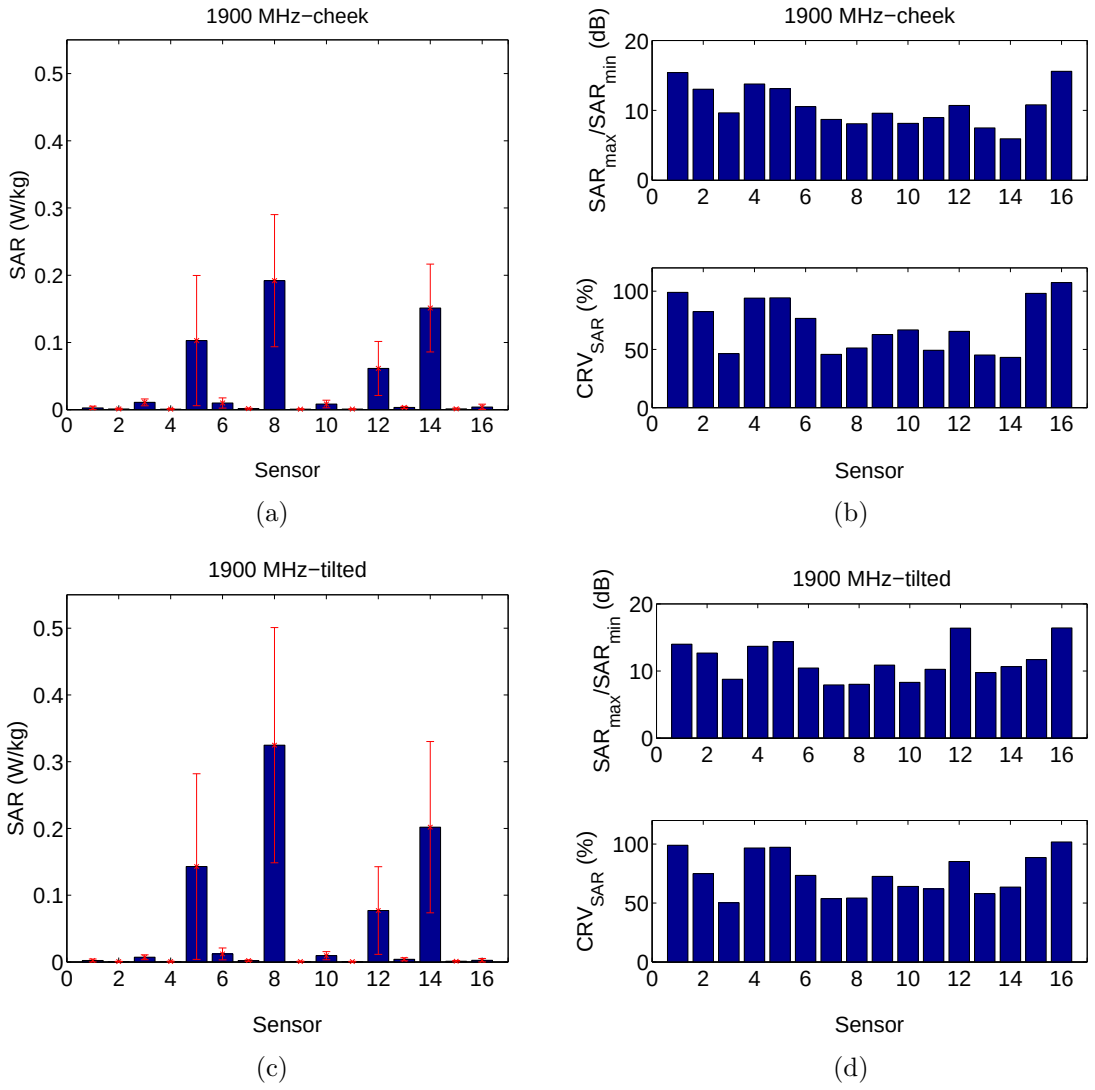

Figure 2.4: Left: Mean and standard deviation of the averaged SAR in the inserted field sensors at 1900 MHz; Right: Calculated variations in terms of ratio of (max/min) and CRV (std/mean).

results of our two methods are consistent and the average of variations is higher (around 4.9 dB in 'cheek' position and 4.7 dB in 'tilted' position) at 1900 MHz than at 835 MHz. The mean of variation in SAR, based on the Talairach method, over all brain regions is around 5 dB for 835 MHz and 10 dB for 1900 MHz. The maximum variation of SAR between the brain regions is in the medulla, which belongs to the lobe type level of Talairach hierarchy, and reaches an order of magnitude of 15.8 dB. Table 2.4 shows the amount of dB_{max} and also the assigned labels of the region with the largest dB, per exposure setup and per Talairach level.

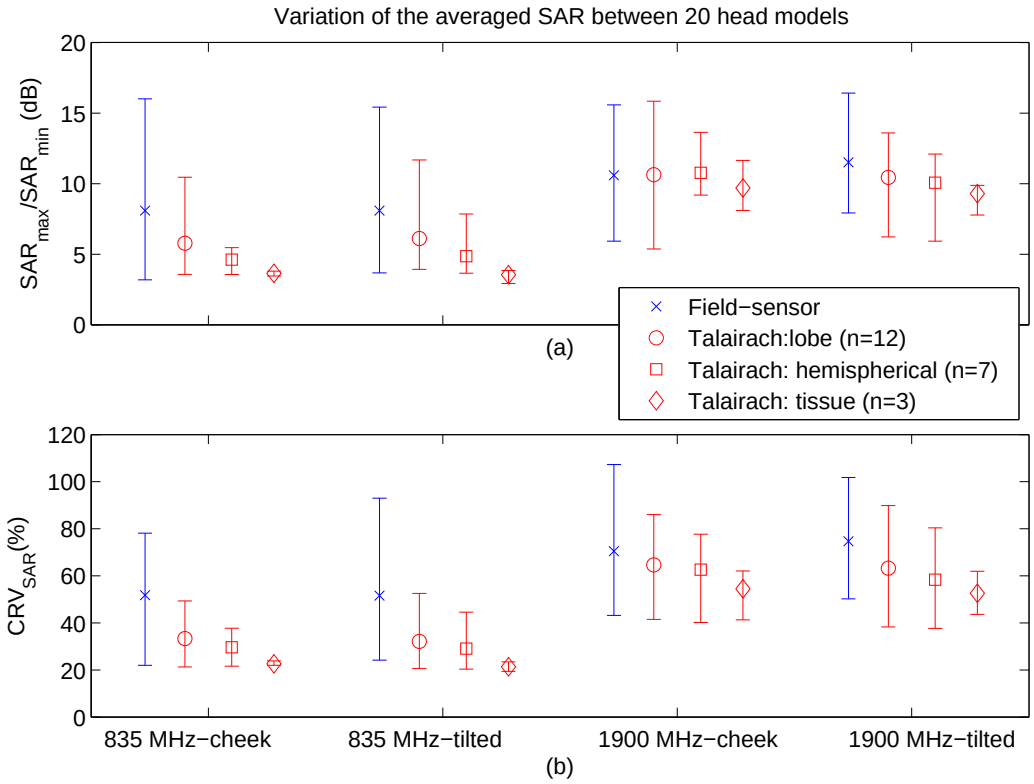

Figure 2.5: Variation of the average SAR between the head models based on our two post-processing methods: Field-sensor (blue) and Talairach (red), in terms of a) ratio of (max/min) and b) CRV (std/mean). The markers show the mean of variation over all brain regions and the error bars show the max-min range per exposure setup.

2.3.3 Variation of peak spatial average SAR

Figure 2.6 presents the mean and std of psSAR_{10g} values in the head and brain for the 20 head models. Table 2.5 summarizes the calculated variation and indicates that the psSAR variation is around 4 dB in the head and can reach up to 7 dB in brain tissue at 1900MHz and in the cheek position. Variations in the spatial locations of psSAR values in the heads and brains are calculated as the distances between the furthermost peak-points. Table 2.5 shows that the maximum spatial variation in the location of psSAR is around 8 cm in the heads of various models.

2.3.4 Numerical uncertainty

To evaluate the expanded uncertainty U of the numerical modeling and simulation settings with 95% confidence, we assessed the influence of various modeling parameters on the simulation results for psSAR_{10g} in the head. Table 2.2 shows that, for non-uniform grid

Table 2.4: The amount and the label of the region where the maximum deviation in SAR per Talairach level was registered.

	Label of region with dB_{max} , level of dB_{max}			
Level	835 MHz-cheek	835 MHz-tilted	1900 MHz-cheek	1900 MHz-tilted
Lobe	Frontal-Temporal Space, 10.45	Frontal-Temporal Space, 11.67	Medulla 15.84	Medulla 13.59
Hemispherical	Right Cerebellum 5.46	* 7.85	Right Brainstem 13.63	Right Brainstem 12.10
Tissue	Cerebro-Spinal Fluid, 3.81	White Matter 3.84	Cerebro-Spinal Fluid, 11.65	Cerebro-Spinal Fluid, 9.87

*non-labeled regions. No VOT label was assigned to these brain regions.

Table 2.5: Variations of $psSAR_{10g}$ in the brain and head between the head models.

	835 MHz-cheek		835 MHz-tilted		1900 MHz-cheek		1900 MHz-tilted	
	Head	Brain	Head	Brain	Head	Brain	Head	Brain
CRV	21.31	25.28	34.98	18.97	26.31	35.34	26.73	34.60
max/min (dB)	4.37	3.49	4.88	2.78	4.00	7.21	4.17	6.14
spatial var.(mm)	69.74	49.08	43.41	60.89	84.43	60.93	30.95	56.06

discretization and by assuming normal distribution and uncorrelated combination, U is 1.26 dB for $psSAR_{10g}$.

2.4 Discussion

In this study, we investigated the variation of local power absorption in the brain caused by morphological changes in 20 head models. We used two different evaluation methods and found that the variation of the averaged SAR in specific brain regions can reach up to 15.8 dB in the medulla region (Talairach method) and up to 16.4 dB in a $1cm^3$ cube (field-sensor method). This large variation is due to the fact that, in different heads, the distance from the source (mobile phone antenna) to that specific brain region is different, i.e. although the equivalent regions are in relatively similar positions in all brains, their absolute distances from the source differ.

From Figure 2.3 and Figure 2.4, one may think that large variation in low exposure area is less of interest. We note, however, that the main objective of this study is to investigate the influence of morphological changes on the RF dose in the area where the brain tumor would preferentially occur. Therefore, it is highly relevant to mention that three of the

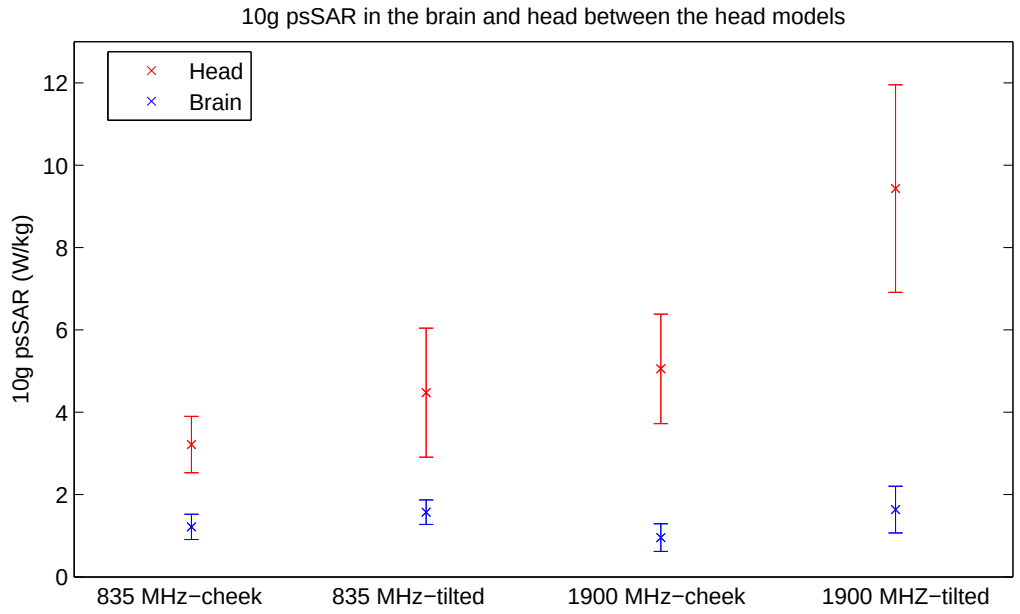

Figure 2.6: Mean and standard deviation of the psSAR_{10g} in the brain and head.

four sensors with the maximum variations (Table 2.3 sensors 1, 9 and 10) are located in the areas in which brain tumors are most frequently found, i.e. the frontal and temporal lobes. In addition, the calculated variations in high exposure area (over sensors 5, 8, 12 and 14) are also large with maximum of 16.3 dB which is related to sensor 12 and 1900 MHz-tilted configuration.

We also found that the variations in morphology lead to larger differences in SAR at a higher frequency. The smaller penetration depth at a higher frequency leads to a lower absorption in the deeper regions of the brain, and consequently to less uniform exposure of the brain. Therefore, a certain variation in the distance between the region of interest and the source causes a greater SAR-variation in a less uniform field than the same deviation does in a uniform field.

Comparison of the results in Figure 2.5 and Table 2.4 shows that an increase in the size of the averaging volume (from sensors in the field-sensor method to tissue level in the Talairach method), will reduce the variation.

To compare our two evaluation methods, we would say that the accuracy of the brain-registration in the field-sensor method was 2.4 mm in terms of the averaged mean surface distance (MSD). This means that the position of a specific sensor in the brains varies by an average of 2.4 mm (error falls within image resolution). However, the results may be underestimated by this method because only parts of the brain are included. On the other hand, while the Talairach method is more complete and covers the whole brain, the definition of Talairach landmarks in our study, as explained in section 2.2.4, might induce some uncertainty in mapping the brain positions into the Talairach atlas and vice versa.

From the fact that the results of the both methods are similar (maximum SAR variation: 15.8 vs. 16.4 dB), we conclude that our results are robust and the conclusion is justified. To investigate the influence of simulation parameters, the numerical uncertainty evaluation was also included. The results show that the $psSAR_{10g}$ variation caused by modeling parameters is equal to 1.26 dB, which is very small relative to the magnitude of the SAR variations obtained. Therefore, our results are also robust to simulation parameters.
The secondary end-point was to assess the variation in $psSAR_{10g}$ caused by morphological changes in the heads. The head $psSAR_{10g}$ variation was 4 dB, which is slightly larger than the variation of $psSAR_{10g}$ reported in previous studies (3 dB) that used several head models and configurations[13,60,105]. This increase may be due to the fact that we used a larger number of head models and consequently more variant head morphologies. Furthermore, these studies either had a limited number of head models[13] or they used scaled models, which lead to large uncertainties in the prediction of local brain exposure[60,105]. To the best of our knowledge, the current is based on the highest number of different anatomical head models in dosimetric studies involving mobile phone exposure.
To be able to evaluate the potential impact of our results on the Interphone study, we must apply the same restrictions as the Interphone and therefore apply the same matching variables between case and controls, i.e. age (within 5 years), sex, and region of residence[11]. If we restrict our population to these conditions, the SAR variations will decrease in the sensors with an average of 5 dB. The maximum variation of 16.4 dB among 20 individuals therefore decreases to 11.8 dB among 4 males (e.g. models 12, 13, 17, 19) in the same field sensor.
Finally we should mention that our study had a number of limitations. First, the sample of 20 selected head models is not representative for the general population, however our results indicate that head morphology can have a high impact on the local RF dose in the brain. This is important for the cases investigated in the Interphone study. Furthermore, as observed in Table 2.1, we conclude that the head characteristics of our samples are in line with human variation.
Second, as mentioned previously, the brain tissues were not segmented in this study, i.e. the brain was considered as a homogeneous tissue. We expect that the segmentation of brain tissues will add to the local dose variation between individuals. In this case, the SAR variation would not only be governed by morphological differences but also by the large differences in the dielectric properties. To verify this, we performed additional simulations for three of our models (patients number 12, 13 and 14) for whom MR-scans were also available. The results confirmed our expectation and showed that the SAR variations, when taking the average over the field sensors, increased from 3 dB between CT-models (homogeneous brain) to 4 dB between MR-models (heterogeneous brain); The impact of full brain segmentation is the topic of our ongoing study.
Third, the phone model which was used in this study was generic and simplistic. However, as mentioned in section 2.2.2, it is the model developed for the same purpose (i.e. comparison of the SAM to 14 anatomical head models) by[60]. The authors mentioned that the phone model was agreed upon with members of the MMF (Mobile Manufacturers Forum) as the standard model for comparative studies. By using the same phone model we are

able to compare our results to that study which helps for understanding the variation found in both studies and to have an accumulation of knowledge. In addition, the impact of various phone models has already been shown by[40].

In summary, if we consider a total uncertainty budget for dosimetry of mobile phone radiation in head and brain, we find the following sources of uncertainty in literature (Table 2.6):

1. Mobile phone model: the variation in brain region-specific exposure is typically around 5 dB, but can reach up to 18 dB[40]

2. The relative position of the mobile phone and head: the maximum variation of $psSAR_{10g}$ in the head was around 4 dB at 900 MHz and 6.6 dB at 1900 MHz over 80 different relative phone positions[39]

3. Age-dependent changes in the dielectric tissue parameters: the differences in $psSAR_{10g}$ due to the age-dependent changes of the tissue dielectric are approximately 0.5 dB at 900 and 1.5 dB in 1800 MHz[13].

4. Pinna compression: the reduced distance caused by pinna compression led to an increase of approximately 2dB in $psSAR_{10g}$ if the maximum exposure is located at the pinna[14].
Here, we introduce a new source of uncertainty which is:

5. Individual morphological properties: the variation in brain region-specific exposure is typically around 5 dB for 835 MHz and 10 dB for 1900 MHz but, according to

Table 2.6: Comparison of uncertainty sources in mobile phone dosimetry.

	Source	Paper	studied parameter	Max var. (dB)
1	Phone type	Gosselin et al. 2011	Region-specific SAR	18
2	Phone position	Ghanmi et al. 2011	$psSAR_{10g}$	6.6
3	Age-dependent dielectric properties	Christ et al. 2010	$psSAR_{10g}$	1.5
4	Pinna compression	Christ et al. 2010	$psSAR_{10g}$	2
5	Head morphology	This study	$psSAR_{10g}$ Region-specific SAR	4 16.4

Talairach tool, can reach up to 15.8 dB and, according to field-sensor method, up to 16.4 dB. Maximum variation of $psSAR_{10g}$ is around 4 dB in the head and 7dB in the brain.

Table 2.6 summarizes the uncertainty sources and their impacts on mobile phone studies.

2.5 Conclusions

Differences in head morphological properties caused up to 16.4 dB variation in the averaged SAR in specific brain regions between 20 head models (Sample: 13 males and 7 females aged between 36-76 years) and 11.8 dB limited to the Interphone's restrictions (sub-sample: 4 males aged between 65-69 years). Thus, estimation of local RF averaged SAR in the brain on the basis of generic phantoms and not on the real morphology is subject to a considerable variability and therefore head morphology should be taken into account for estimation of cumulative RF dose in the brain. The extent of this variability depends on the exposure setup (mobile phone frequency and position) and on the size and position of the brain region in question.

CHAPTER 3

Association of acute adverse effects with high local SAR induced in the brain from prolonged RF head and neck hyperthermia

This chapter is based on:
F Adibzadeh, RF Verhaart, GM Verduijn, V Fortunati, Z Rijnen, M Franckena, GC van Rhoon and MM Paulides. Association of acute adverse effects with high local SAR induced in the brain from prolonged RF head and neck hyperthermia.
Phys Med Biol, Vol. 60, pp. 995-1006, 2015.

Abstract

Purpose: *To provide an adequate level of protection for humans from exposure to radio-frequency (RF) electromagnetic fields (EMF) and to assure that any adverse health effect is avoided, the basic restrictions in terms of specific energy absorption rate (SAR) were prescribed by IEEE and ICNIRP. An example of a therapeutic application of non-ionizing EMF is hyperthermia (HT), in which intense RF energy is focused at a target region. Deep HT in the head and neck (H&N) region involves inducing energy at 434 MHz for 60 minutes on target. Still, stray exposure of the brain is considerable but to date only very limited side-effects were observed. The objective of this study is to investigate the stringency of the current basic restrictions by relating the induced EM dose in the brain of patients treated with deep head and neck (H&N) HT to the scored acute health effects.* ***Materials and methods:*** *Hereto, we performed a simulation study to calculate the induced peak 10 g spatial-averaged SAR ($psSAR_{10g}$) in the brains of 16 selected H&N patients who received the highest SAR exposure in the brain, i.e. who had the minimum brain-target distance and received high forwarded power during treatment.* ***Results:*** *The results show that the maximum induced SAR in the brain of the patients can exceed the current basic restrictions (IEEE and ICNIRP) on $psSAR_{10g}$ for occupational environments by 14 times.* ***Conclusions:*** *Even considering the high local SAR in the brain, evaluation of acute effects by the common toxicity criteria (CTC) scores revealed no indication of a serious acute neurological effect. In addition, this study provides pioneering quantitative human data on the association between maximum brain SAR level and acute adverse effects when brains are exposed to prolonged RF EMF.*

3.1 Introduction

The application of non-ionizing electromagnetic field (EMF) in the radiofrequency (RF) range of the spectrum is not only limited to telecommunication systems such as radio and television broadcasting, mobile phone and WiFi, but also many biomedical applications use RF EMF for diagnosis and therapy such as magnetic resonance imaging (MRI) and hyperthermia (HT). During HT cancer treatment, the tumor temperature is increased by $3-8\,^{\circ}\mathrm{C}$, which has shown to enhance treatment outcome without increasing toxicity when added to radiotherapy (RT) and/or chemotherapy (ChT)[59,96,104]. Besides depositing energy at the target region, stray radiation leads to unwanted exposure of other normal tissues (Figure 3.1). Deep hyperthermia in the head and neck region, especially for target regions in the nasopharynx and paranasal sinuses, involves heating very closely to the brain. Hence, there is a relevant risk of HT-related acute effects in the brains. In this

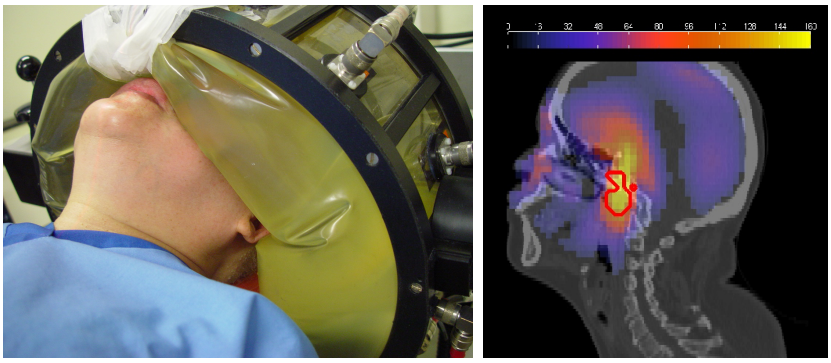

Figure 3.1: Picture of the HYPERcollar system (left). Example of the SAR distribution inside the head (right), the red line indicates the target region.

study, we investigated the association of relatively high localized SAR in the patients brain with the acute health effects observed after H&N HT treatments.
To protect against excessive temperature rises from localized exposure in any part of the body, basic restrictions have been developed by a number of international and national organizations, including the ANSI, IEEE and ICNIRP. Based on the current common criteria for human exposure to electromagnetic fields[55,57], exposure should not result in peak spatial average SAR (psSAR) that exceeds 10 W/kg as averaged over any 10 g of tissue (psSAR_{10g}). This level applies to exposure of persons in occupational environments, i.e. trained adults under controlled conditions. The exposure limit has been reduced by a factor of 5 for public environments, i.e. individuals of all ages and various health statuses, leading to a psSAR_{10g} limit of 2 W/kg. The exposure limits incorporate safety factors that account for uncertainties in the data and that provide a large margin of safety for other limiting conditions such as high ambient temperature, humidity, or level of physical activity. The safety factors, which are generally selected arbitrarily, are conservative so that exposures that exceed the basic restrictions are not necessarily harmful. All guidelines for limiting exposure are based on established adverse health consequences induced by RF exposure. To date, at RF frequencies above 100 KHz, only acute thermal effects have been observed but current findings are almost entirely data obtained by animal experiments (IEEE 2005). Therefore, human data is of vital importance for assessment of the induced health hazards that are the basis of the development of safe RF exposure restrictions.
The main objective of our study was to evaluate the association of acute adverse effects with HT-induced dose in the brain from prolonged (60 minutes) RF HT in patients in order to investigate stringency of the current basic restrictions. To achieve this goal, we firstly assessed the maximum induced psSAR in the brain of 16 patients during H&N HT treatment and compared the results with the common basic restrictions. Anatomical models of these 16 patients were generated from tissue segmentation based on CT-scans. Segmenting white matter regions on CT-scans is not possible and the total brain is segmented as one structure. Therefore, we also assessed the influence of brain segmentation detail on the induced psSAR in the brain. Finally, we assessed the common toxicity criteria

(CTC) data reported for the treated patients to evaluate the association of HT-induced SAR in the brain with acute health effects.

3.2 Methods

3.2.1 Head and neck hyperthermia

Hyperthermia treatments of 60 minutes each were given after radiotherapy once or twice a week at intervals of at least 72 h[85,96]. Hyperthermia was delivered using the HYPERcollar[78,79]. The HYPERcollar is a phased array applicator that consists of twelve electromagnetic patch antennas operating at 434 MHz. To enhance the efficiency of the energy coupling into the patient and to cool the skin, the space between the HYPERcollar antennas and patient is filled with a waterbolus (Figure 3.1). The amplitudes and phases of the sinusoidal signals applied at all 12 antennas are independently controlled. To maximize power delivery at the target region the signals (powers and phase-differences) and patient positioning are optimized using hyperthermia treatment planning (HTP). HTP is based on electromagnetic simulations using 3D patient-specific models for optimization and tissue dose assessment[80,85]. To account for differences in patients and thermal properties, the antenna signals are adapted during clinical treatment based on an online steering procedure[85].

3.2.2 Anatomical phantoms

Computational simulations using anatomically detailed models of adults and children have been used in several studies to predict electromagnetic exposure of humans for various exposure applications and environments[6,13,21,47,53,75,102,105]. In the current study, we used detailed 3D models of patients to assess the EM dose in the brain during H&N HT. These patient models are generated by segmenting tissue regions using Computed Tomography (CT) scans, which encompass the whole head and part of the shoulders. Seven different tissue types (internal air, bone, fat, muscle, spinal cord, brain and lung) were segmented manually[99]. We assessed the induced psSAR_{10g} in the brain of 16 patients selected from 45 patients treated with HT that far (September 2014). The CT-based models of these 16 patients were selected, as they received the highest forwarded power during treatment and had the minimum target-brain distance. Tumors were primarily located in the nasopharynx and oropharynx (nasal and oral cavity).
Note that it is impossible to segment detailed brain structures on CT-scans, so the brain is modelled as one homogeneous mass with grey matter properties. Therefore, SAR assessment is based on a rough model of the brain. To evaluate the influence of detailed brain segmentation, we compared the psSAR_{10g} values between CT-based (homogeneous) and MR-based (detailed) brain models of 12 patients. Among these 12 patients, of which MR scans were also available, only the first one was treated with HT. Fortunately this case

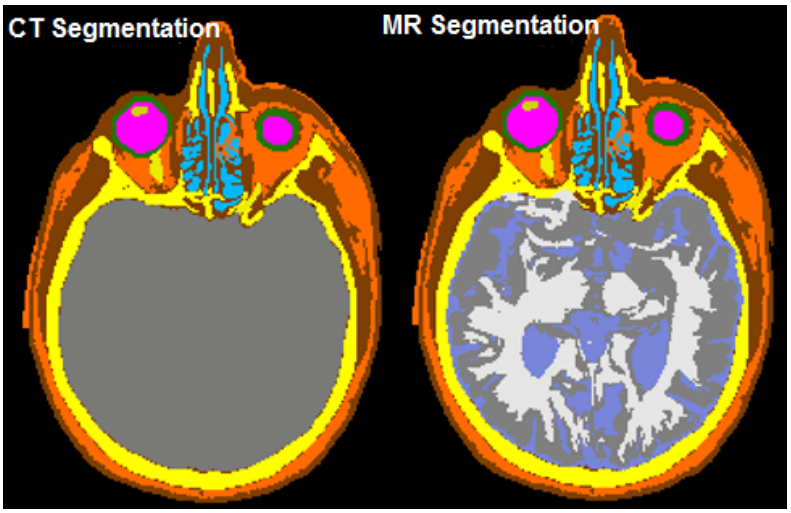

Figure 3.2: homogeneous (CT-based) versus detailed (MR-based) brain model, as used in this study to investigate the influence of brain segmentation details.

turned out to be the worst-case in terms of SAR exposure in our study, i.e. the patient with the highest SAR in the brain.

3.2.3 Influence of brain segmentation details

To evaluate the influence of brain tissue distribution on the induced SAR in the brain, we calculated the $psSAR_{10g}$ using homogeneous (CT-based) and detailed (MR-based) brain models and assessed the differences. Mean and standard deviation of these differences give the systematic and random errors caused by modelling the brain as a homogeneous tissue (as used in HTP) instead of using detailed segmentation.
A state of art method[15,17] has been applied for the automatic segmentation of the brain tissues, i.e. cerebro-spinal fluid (CSF), grey matter (GM), and white matter (WM) from T1-weighted (T1w) and T2-weighted (T2w) MR images. This method consists of a supervised segmentation using the k-nearest neighbor (kNN) classifier. The training of such a classifier is automatically obtained using atlas registration. The detailed segmented brain was registered to the CT model using optimized settings[29]. Figure 3.2 shows the brain tissues in both the homogeneous and the detailed model.

3.2.4 EM-modeling

EM computations were performed using the finite difference time domain (FDTD) solver of SEMCAD X *. A uniform gridsize of 1.3 mm, a 15 mm padding and medium strength

*SEMCAD X EM Simulation, version 14.8.4 (www.semcad.com).

UPML boundaries were chosen. Antennas were excited by a sinusoidal signal of 15 periods, using optimized phase and amplitude settings that correspond to the maximum forwarded power during HT treatment. In this study, we calculated the maximum psSAR over treatment. Dielectric tissue properties were assigned to each tissue according to the ITIS material parameter database[48]. The value of psSAR_{10g} in shape of a cube, as calculated in SEMCAD X, was used for SAR dosimetry.

3.2.5 Validation of EM-modeling results

The predicted SAR distributions that are induced by the HYPERcollar were evaluated in a cylindrical muscle phantom by comparing the measurements to simulations[77,78]. We demonstrated that the measured SAR distributions were well predicted by simulations. However, in clinical applications most of the applicator inefficiency, as defined in this study, stems from the waterbolus shape variations over patients (anatomical phantoms). To assess this impact we calibrated the SAR predictions by deriving a scalar 'applicator efficiency'. Hereto we used invasive temperature measurements obtained from clinical treatments for those 14 H&N patients of which temperature data from interstitially placed probes was obtained. The power-off method[87,103] was applied to reconstruct the SAR values from temperature decay measurements, as described in[86]. In addition, we developed an accurate probe reconstruction procedure to obtain the simulated SAR corresponding to the measurement of each temperature probe[86,100]. Next, the applicator efficiency factor was optimized such that the error between reconstructed and simulated SAR values per patient and per waterbolus-shape was minimized. Finally, we computed the mean and distribution of the differences between measurements and simulations, on a patient-specific and treatment-specific basis, to obtain the best assessment of the mean applicator efficiency and its variation in the clinic.

3.2.6 Sensitivity analysis

We performed a sensitivity analysis to determine the changes in psSAR_{10g} that result from changes in EM simulation and patient modeling parameters. Model discretization (gridsize) and dielectric tissue properties were reported as the most significant influence quantities (i.q.)[6,41,99]. The effect of these parameters was determined based on a previous study using 7 patient models, balanced per tumor site[99]. The uncertainty is quantified in $|\Delta psSAR_{10g}|$ and the individual uncertainty was obtained by taking the square-root of the sum of squares of the mean value over 7 patients. In the current study, the uncertainty due to detailed brain segmentation and applicator efficiency were also investigated.
The effect of the gridsize variation was investigated by changing the gridsize from 1 to 5 mm with stepsize of 0.5 mm, with an addition of gridsize 1.3 mm. For each gridsize $|\Delta psSAR_{10g}|$ was determined by using the HTP with gridsize = 1 mm as reference.
The variation in tissue properties (σ_{eff}, ϵ_r and ρ) was determined for the brain tissue. For each tissue property, three different HTPs were generated, i.e. using average and $\pm$

one standard deviation of the literature value. $|\Delta psSAR_{10g}|$ was determined by using the HTP for the average literature value as reference.
The variation in psSAR values between homogeneous and detailed models of the brain was calculated for 12 patients, as mentioned in section 3.2.2. Mean and standard deviation of this variation give the systematic error and the uncertainty of modeling the brain as a homogeneous tissue, respectively.
We derived the uncertainty due to the applicator efficiency by optimizing the applicator efficiency factor which, as defined in this paper, is a scalar that captures not only the losses in the conductors and antennas, but also all effects of non modelled radiation losses in the waterbolus (section 3.2.5). Note that the impact of the waterbolus on superficial levels is very inhomogeneous but deep in the brain this approximation becomes valid. psSAR values were calculated for each applicator efficiency factor, i.e. using mean and standard deviation of the optimized value. $|\Delta psSAR_{10g}|$ was determined by using the average value as reference.
The individual standard uncertainty (u_i) of the gridsize, dielectric properties, detailed segmentation and applicator efficiency was obtained by determining the confidence interval from plus to minus one standard deviation. The combined standard uncertainty (u_c) was obtained by taking the square-root of the sum of squares of the individual uncertainties. The coverage factor (k) of 2 was used to obtain the expanded uncertainty (U) with 95% confidence interval. The uncertainties were determined using a normal (N) or rectangular (R) probability distribution for each i.q.: N for dielectric properties according to[6], R for gridsize according to[41] and R for applicator efficiency and brain segmentation details because this distribution provides the most conservative estimate when minimum knowledge is available.

3.2.7 HT-related acute health effect

To investigate the possibility of serious HT-related acute health effects, we studied the Common Toxicity Criteria (CTC) scores of the selected patients. CTC is a standardized classification of adverse effects used in cancer therapy evaluation, developed by the National Cancer Institute [†]. Any treatment-related adverse event experienced by a patient is graded by clinicians using the specific terms in the CTC. Table 3.1 shows the general definition of the grades 0 to 5 with their unique clinical descriptions of severity. Grading is not modified based on patient's condition at baseline. Baseline data, including laboratory data and signs and symptoms, should be collected at treatment entry. If a given adverse event is experienced more than once in a treatment session, only the most severe event is graded. Adverse events not included in the CTC (v3.0) should be reported under the 'Other 'adverse events and graded according to the general grade definition.
All HT patients are questioned by physicians before a treatment starts (baseline) and after each treatment session, leading to CTC scores for toxicity and pain. In addition, at

[†]http://ctep.cancer.gov/protocolDevelopment/electronic_application/ctc.htm.

Table 3.1: CTC Grades definition

Grade	definition
0	No adverse event or within normal limits
1	Mild adverse event; asymptomatic or mild symptoms; clinical or diagnostic observations only; intervention not indicated.
2	Moderate adverse event; minimal, local or noninvasive intervention indicated; limiting age-appropriate instrumental ADL*.
3	Severe or medically significant but not immediately life-threatening; hospitalization or prolongation of hospitalization indicated; disabling; limiting self care ADL**.
4	Life-threatening consequences; urgent intervention indicated.
5	Death related to adverse event

Activities of Daily Living (ADL)
*Instrumental ADL refer to preparing meals, shopping for groceries or clothes, using the telephone, managing money, etc.
**Self care ADL refer to bathing, dressing and undressing, feeding self, using the toilet, taking medications, and not bedridden.

the beginning of each HT session, patients are asked to describe how the treatment has affected them (active open questioning).

3.3 Results

3.3.1 Influence of brain segmentation details

Figure 3.3 shows the difference in $psSAR_{10g}$ when the brain is modeled as homogeneous GM (model 1) and GM+WM+CSF (model 2). This figure indicates that the induced $psSAR_{10g}$ in the brain decreases in detailed models (model 2) compared to homogeneous models (model 1) by 21.5%, averaged over the models. Inclusion of CSF in the tissue list for calculation of psSAR, increases the $psSAR_{10g}$ value by 15.1% averaged over the models, compared to the homogeneous model. Hence, the predicted dose in the detailed model is particularly dependent on the presence of CSF.

3.3.2 Applicator efficiency

We obtained the applicator efficiency factor, which minimized the difference between measured and simulated SAR values, per treatment session and per patient. The optimized efficiency factor ranges from 0.29 to 0.71 with mean and standard deviation of 0.40 and 0.14, respectively, averaged over all waterbolus-shapes.

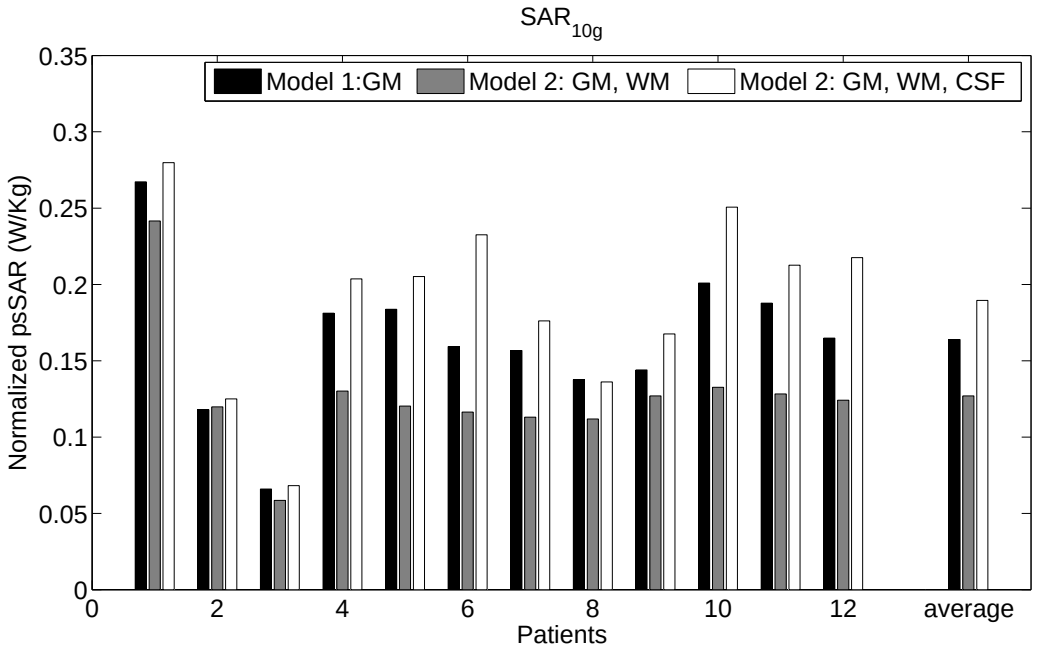

Figure 3.3: Variations of the $psSAR_{10g}$ in the brain between homogeneous and detailed brain models across 12 patients. The results are normalized to the net input power (1 W).

3.3.3 Sensitivity analysis

Table 3.2 summarizes the impact of various modeling parameters on the obtained results. The uncorrelated standard combined uncertainty u_c is 11.7% and the expanded uncertainty U is 23.4% for $psSAR_{10g}$. Note that the impact of applicator efficiency variation overrules the other uncertainties studied.

3.3.4 HT-related acute health effect

Table 3.3 contains the CTC grades of the observed acute toxicity occurred during all HT treatment sessions for the selected patients. No grade 4 or 5 toxicities were observed and the three CTC grade 3 incidents were all subcutaneous burns that healed without any further medical attention. Other observed toxicities did not exceed CTC grade 2 in any of the patients.

3.3.5 Induced psSAR in the brain versus scored acute effects

Figure 3.4 shows the scatter plot of maximum obtained $psSAR_{10g}$ in the brain during H&N HT treatments versus maximum CTC grade. The maximum CTC grade, scored for each patient is related to the maximum induced psSAR in the brain providing a dose-response

Table 3.2: Evaluation of the standard combined uncertainty (u_c) and the expanded uncertainty (U) as measured with $|\Delta psSAR_{10g}|$. Div. is the division factor to obtain the standard uncertainty (std. unc.) and k is the coverage factor for the confidence interval. The sensitivity coefficients c_i equals one for all influence quantities.

	SAR unc.[%] $\|\Delta psSAR_{10g}\|$	prob. dist.	Div	SAR std. unc.[%] $\|\Delta psSAR_{10g}\|$
Gridsize	3.7	R	$\sqrt{3}$	2.1
Dielectric tissue properties				
(a) σ_{eff}	3.4	N	1	3.4
(b) ϵ_r	2.8	N	1	2.8
(c) ρ	3.3	N	1	3.3
Brain segmentation details	10.9	R	$\sqrt{3}$	6.3
Applicator efficiency	13.9	R	$\sqrt{3}$	8.0
u_c				11.7
U (k=2)				23.4

picture. Note that data in Table 3.3 and Figure 3.4 are different. Table 3.3 includes all incidents of acute effects whereas Figure 3.4 demonstrates the maximum scored CTC grade per patient. For instance, Table 3.3 includes 3 incidents of CTC grade 3 but 2 incidents were for the same patient therefore, the number of CTC grade 3 in Figure 3.4 is 2. The cross markers (Figure 3.4a) display the CNS-related adverse effects (headache, pain in eye, dizziness, nausea, vomiting, pns. motory and pns. sensory) versus psSAR_{10g} in the brain and the circle markers (Figure 3.4b) show the maximum CTC-grades for the remaining effects (subcut skin, fat, muscle and bone) versus the psSAR_{10g} in the corresponding tissue types. The psSAR values are corrected for the systematic error calculated in section 3.3.1 (brain segmentation details) and 3.2 (applicator efficiency). Since patients are treated under supervision of medical physicians, the results are only compared to the ICNIRP and IEEE basic restrictions for occupational environment (controlled environment). Figure 3.4 shows that the basic restriction on psSAR_{10g} is exceeded for all patients.

3.4 Discussion

Published experimental data on adverse RF effects in humans is very scarce, but is of great potential value to health and standards agencies for developing safe limits of RF exposure. At present, the basic restrictions rely almost entirely on much less satisfactory animal experimental data which is more difficult to interpret, contributing to a rather unsystematic approach in setting the safety factors of RF exposure limits. In this study, we addressed concerns about temperature increases in the human brains from a prolonged

Table 3.3: Observed acute toxicity for the selected HT patients. Note that the number of incidents were counted, i.e. not just one incident per patient, so every treatment session always led to one score.

Nr of patients: 16
Total Nr of HT sessions:74

	CTC-grade	0	1	2	3	4	5
CNS-related	Pns motory	74	0	0	0	0	0
	Pns sensory	71	1	2	0	0	0
	Headache	73	1	0	0	0	0
	Pain in Eye	73	1	0	0	0	0
	Dizziness	73	1	0	0	0	0
	Nausea*	71	2	1	0	0	0
	Vomiting*	72	2	0	0	0	0
Subcut burns	Subcut skin	70	2	0	2	0	0
	Subcut fat	72	0	2	0	0	0
	Subcut muscle	72	0	2	0	0	0
	Subcut bone	69	1	3	1	0	0

*Nausea and vomiting may stem from reactions in the CNS but also from many other causes. In this study they are considered as CNS-related acute effects.

(60 minutes) and relatively high localized exposure during head and neck HT and the association of such exposure with acute health effects. The results show that the maximum induced $psSAR_{10g}$ in the brain of the selected patients exceed the basic restrictions[55,57] for occupational environments up to 14 times. The results obtained can even be regarded as conservative estimates since we used the applicator efficiency factor reconstructed from temperature decay measurements, i.e. 0.4. This factor may be affected by measurements adjacent to external or internal skin, leading to overestimates of tissue cooling. In addition, this factor is lower than the efficiency obtained experimentally using a cylindrical phantom and a symmetrical waterbolus shape, i.e. 0.7. Hence the SAR values may have been 75% higher. In future, we aim to investigate the association between SAR and functional brain changes using our new HYPERcollar3D[95], which has been used for three patients, that has a much more predictable waterbolus shape leading to improved SAR predictions.
The condition of the patients at baseline, during and after each treatment section were checked by the physicians using the CTC guidelines. These data indicates that there is no evidence of serious (CTC grade 3 and more) acute HT-related neurological toxicity for any of the selected patients (Figure 3.4 and Table 3.3). Moreover, in multimodality therapies such as radiotherapy combined with hyperthermia, adverse events may also be caused by the multimodality combination: in this study we allocated all of them to only

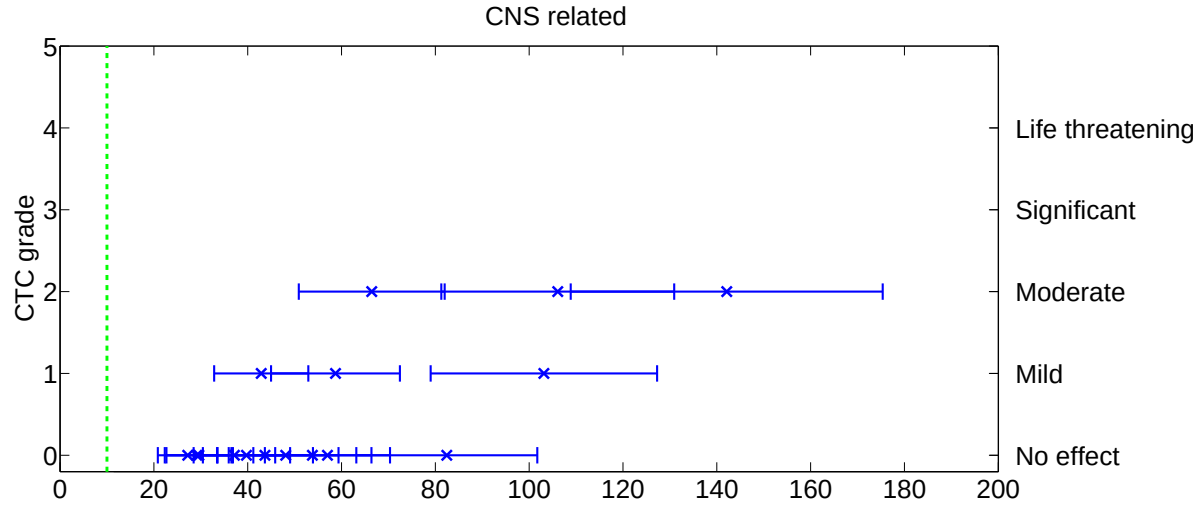

(a)

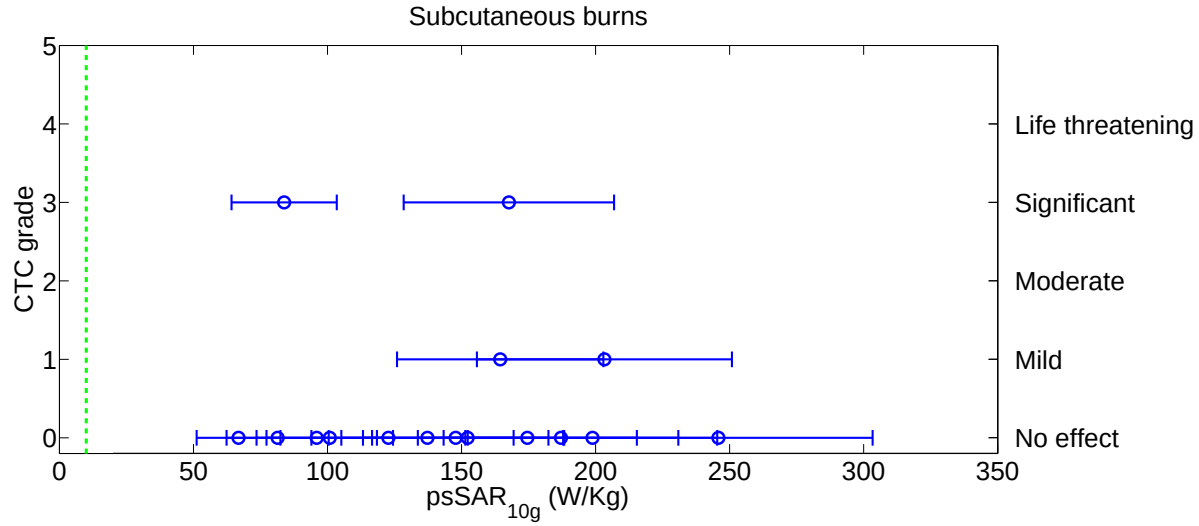

(b)

Figure 3.4: Scatter plot of the **maximum** CTC grade vs the maximum induced psSAR_{10g} for the selected patients during H&N HT treatment. (a) The maximum CTC-grades for CNS-related adverse effects versus the psSAR_{10g} in the brain. (b) The maximum CTC-grades for the subcutaneous burns versus the psSAR_{10g} in the corresponding tissue types. The results are compared to the occupational basic restrictions (green dashed line). The psSAR_{10g} values are corrected for the systematic errors, due to homogeneous brain modeling and applicator efficiency. Errorbars indicate the calculated 95% confidence interval of the uncertainty.

the EMF exposure during hypethermia.

We also investigated the influence of the brain segmentation details in a 3D patient-specific model and found that the detailed segmentation reduces the $psSAR_{10g}$ in the brain tissues (WM and GM) compared to homogeneous brain model by 21.5%, averaged over the patients. The decrease in SAR for the detailed model is consistent with the fact that the CSF surrounding the brain is highly conductive, i.e. its electrical conductivity is five and three times larger than that of WM and GM respectively. Therefore, CSF absorbs a large portion of the incident EM power leading to less power absorption in the brain tissues (GM and WM). Hence, more detailed segmentation affects local tissue dose predictions.
A sensitivity study showed an expanded uncertainty of 23.4% in $psSAR_{10g}$ due to variations in simulation settings and patient modelling parameters (Table 3.2). However, even taking into account these uncertainties, the results are still valid, i.e. even for the lower uncertainty bound the basic restrictions are exceeded for all patients.
Finally, we note that, based on this study, we do not claim that exposure of the brain to the RF EMF during deep H&N HT has no influence on human health and biology. However, based on the current CTC data, we observed no indication that any serious neurological acute effect is induced at SAR levels above the assumed thresholds.

3.5 Conclusions

This study provides pioneering quantitative human data on the association between the maximum brain SAR level and acute effects when brains are exposed to RF EMF. Such information is pivotal input for establishing dedicated $psSAR_{10g}$ restrictions to avoid adverse effects in occupational and public EMF exposure conditions. Evaluation of acute adverse effects from prolonged exposure to deep RF head and neck hyperthermia reveals that although the brain was exposed up to 14 times the common basic restriction on $psSAR_{10g}$, there is no indication of any induced serious neurological adverse effect. This study provides initial data that enables to determine the basic restrictions based on the functional change that is to be prevented and the level of safety to ensure prevention. Expanding upon this data, a library of associations between exposure level and effect-level can be created for continuously tailoring the basic restrictions.

CHAPTER 4

Absence of acute ocular damage in humans after prolonged exposure to intense RF EMF

This chapter is based on:
F Adibzadeh, GC van Rhoon, GM Verduijn, NC Naus-Postema and MM Paulides. Absence of acute ocular damage in humans after prolonged exposure to intense RF EMF.
Phys Med Biol, Vol. 61, pp. 488-504, 2016.

Abstract

Purpose: *The eye is considered to be a critical organ when determining safety standards for radio-frequency (RF) radiation. Experimental data obtained with animals showed that RF heating of the eye over a specific threshold particularly can induce cataracts. During hyperthermia treatment of cancer in the head and neck, the eyes receive a considerable RF dose due to stray radiation of the prolonged (60 minutes) and intense exposure at 434 MHz of this region. In the current study, we verified the exposure guidelines for humans by determining the association between the electromagnetic and thermal dose in the eyes with the reported ocular effects.* ***Materials and methods:*** *We performed a simulation study to retrospectively assess the specific absorption rate (SAR) and temperature increase in the eyes for 16 selected patients (encompassing 74 total treatment sessions) whose treatment involved high power delivery as well as a minimal distance from the tumor site to the eye.* ***Results:*** *Our results show that the basic restrictions on the peak 10 g spatial-averaged SAR (10 W/kg) and peak tissue temperature increase (1 °C) are exceeded by up to 10.4 and 4.6 fold, on average, and by at least 6.2 and 1.8 fold when considering the lower limit of the 95% confidence interval.* ***Conclusions:*** *Evaluation of the acute effects according to patients feedback (all patients), the common toxicity criteria scores (all patients) and an ophthalmology investigation (one patient with the highest exposure) revealed no indication of any serious acute ocular effect, even though the eyes were exposed to high electromagnetic fields, leading to a high thermal dose. We also found that, although there is a strong correlation (R^2=0.88) between the predicted induced SAR and temperature in the eye, remaining uncertainties in temperature-SAR relationship are large. Given this large uncertainty (129%) compared to the uncertainty of 3D temperature simulations (61%), we recommend to use temperature simulations as dosimetric measure in electromagnetic exposure risk assessments.*

4.1 Introduction

To avoid any adverse health effect from exposure to radio frequency (RF) electromagnetic fields (EMF), basic restrictions for the SAR levels in humans are developed by a number of international and national organizations, including the ANSI, IEEE and ICNIRP. The restrictions are based on keeping the body temperature increase under 1 °C. Based on the current common criteria for human exposure to electromagnetic fields[55,57], exposure should not result in peak spatial average SAR (psSAR) that exceeds 10 W/kg as averaged over any 10 g of tissue (psSAR_{10g}). This level applies to exposure of persons in occupational

environments, i.e. trained adults under controlled conditions. These guidelines incorporate large safety factors to assure that any effect, reversible and non-reversible is avoided. To date, the only known adverse effect for radiofrequency (RF) exposure above 100 KHz are acute temperature dependent effects. Heat tolerance varies between tissues and the eyes have been regarded as one of the most thermo-sensitive tissue in the ICNIRP guidelines. A number of reversible and non-reversible ocular effects by heat have been reported. In a recent overview of heat-induced normal tissue effects by Yarmolenko et al., they concluded that a CEM43°C of only 21.3 minutes leads to adverse effects in cornea of rabbits[110]. Using the CEM43°C definition[19] and the duration of steady-state temperatures during a hyperthermia treatment, i.e. 60 minutes, the thermal dose can be rearranged to 42.2 °C. Elder specifically reviewed the effects of RF waves on eye structures[25]. He summarized that the non-reversible effects reported are cataracts, corneal lesions, retinal effects, and changes in vascular permeability. However, the majority of studies were about cataracts and, furthermore, basing a threshold on the other effects is hampered by conflicting data and the absence of functional changes. Following this data, guidelines for exposure to RF exposure are based on avoiding the induction of cataracts.

The two most cited studies with respect to cataracts are by Guy and Kramar et al[45,63]. They showed that the minimum SAR required to produce a lens cataract in rabbits is between 100 and 150 W/kg for up to 100 minutes in the vitreous body of the eye[45]. The results also indicated that the temperature behind the lens must exceed 41 °C for production of posterior lens opacities. By numerical simulations they established that the temperature rise was caused by a peak SAR in the eye, right behind the lens. However, when temperatures remained below 41 °C by means of reduction of the whole-body temperature, the same SAR levels did not produce any opacity in the lenses of exposed animals[63]. These findings suggest that it is really the temperature that induces the cataracts. The same group also showed that equal, and higher, exposure levels do not lead to cataracts formation in rhesus monkeys, which was allocated to different energy absorption patterns in the eyes of monkeys from those in rabbits[70]. Furthermore, they deduced that 43 °C was required to form cataracts in the lenses of monkeys.

With respect to therapeutic applications, Bollemeijer et al reported the effect of RF-induced heat on the eye using their 2450 MHz stripline applicator[7,65]. Healthy eyes of nine rabbits were heated to a fixed temperature in the range of $42 - 46$ °C for 30 minutes as predicted using a thermal model. Histology based analysis 12 days after the exposure revealed a transition at $44 - 45$ °C, above which local necrosis, pigment disruption and local cataract developed. These observations were confirmed in vivo by comparative fluorescein angiography and anterior segment fluorophotometry that showed fluorescein leakage of the iris vessels. In[65], in agreement with the experiments, no cataract was observed upon heating the lens of a patient to 44 °C for one hour. Note that this study only assessed acute effects and cataracts can appear up to one year after treatment. Hence, these data do not exclude the existence of a lower threshold for long term effects.

These studies show that extrapolation of the results from animals to humans may not be valid. Therefore, human data is of vital importance for assessment of the association between exposure and induced health hazards as foundation for the development of im-

proved RF exposure restrictions. In the current study, we investigated the association of relatively high induced SAR and temperature in the human's eye with the acute health effects observed after head and neck (H&N) hyperthermia (HT) cancer treatments. In H&N HT, the tumor temperature is elevated towards $39-44\,^{\circ}\mathrm{C}$ by applying focused RF energy to tumors in the head and neck region[78]. Besides depositing energy at the target region, stray radiation leads to unwanted exposure of other normal tissues (Figure 4.1), especially for target regions in the nasopharynx, nasal cavity and paranasal sinuses, which are adjacent to the eyes. Hence, there is a relevant risk of HT-related acute effects in the eyes.
In the previous chapter, we showed that there is no indication for association of neurological acute effects and the high excessive local SAR in the brain from exposure to H&N HT. In the current study, we verified the validity of this finding for ocular effects and also expand the data to peak temperature rise estimation to determine if the thermal dose, i.e. peak temperature over a prolonged duration of exposure, induced by such high local SAR values leads to acute thermal effects.

The main objective of our study was to evaluate if there exist an association of acute ocular damage with HT-induced psSAR and temperature rise in the eye from prolonged (60 minutes) exposure to RF HT. In order to determine the suitability of psSAR_{10g} as an appropriate metric for safety guidelines, we verified the correlation of induced psSAR_{10g} to peak temperature increase. To achieve these goals, we firstly calculated the maximum induced psSAR and the peak temperature increase in the eye of 16 patients during H&N HT treatment and compared the results with the common basic restrictions and the eye thermal threshold. Secondly, in order to assess and understand the reliability of the results, we performed an extensive sensitivity analysis. Finally, to investigate the possibility of HT-related ocular damage, we studied the common toxicity criteria (CTC) data reported for the treated patients and the results of opthalmology tests for one patient.

4.2 Methods

4.2.1 Head and neck hyperthermia

Hyperthermia treatments of 60 minutes each were given after radiotherapy once or twice a week depending on the radiotherapy radiation schedule[85,96]. Hyperthermia in the head and neck region was delivered using the HYPERcollar applicator[78,79]. The HYPERcollar is a ring-shape phased-array applicator that consists of twelve electromagnetic patch antennas symmetrically distributed on 2 antenna rings and operating at 434 MHz. To cool the skin and to enhance transfer of the electromagnetic waves into the patient, the space between the HYPERcollar antennas and patient is filled with a waterbolus (WB). For all patients, patient-specific hyperthermia treatment planning (HTP) is done prior to the first treatment to determine the optimal position of the applicator as well as the optimal settings of phase and amplitude per individual channel. In our current HTP, electromagnetic simulations are used to predict the energy deposition, i.e. SAR, in the patient[80,85].

(a)

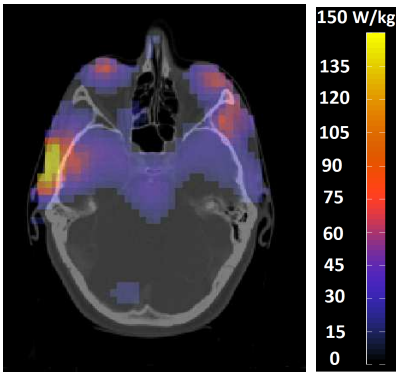

(b)

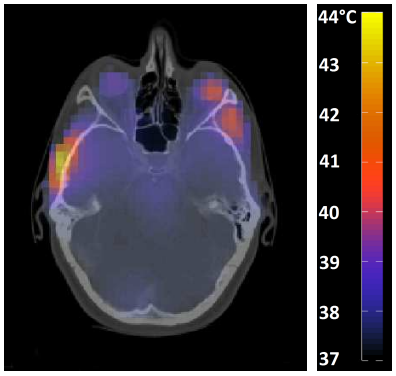

(c)

Figure 4.1: Picture of the HYPERcollar system in clinical use (a). Example of the predicted SAR (b) and Temperature (c) distribution on the planning CT.

To account for differences in patients and thermal properties, the antenna signals are adapted during clinical treatment based on an online complaint-adaptive steering strategy[85]. It is worth mentioning that the patients are not under anesthesia during treatment. Hence, the patients have their full thermophysiological response and pain sensation.

4.2.2 Anatomical phantoms

3D models of 16 patients were selected from a group of in total 49 patients treated with H&N HT until January 2015. In these patients, the SAR was assumed to be the highest in the eye since they had the smallest eye-target distance and received the highest averaged forwarded power during treatment. The patient models were generated by automatically segmenting ten different tissue types (internal air, bone, fat, muscle, spinal cord, brain, sclera, vitreous humor, lens and optical nerve) on Computed Tomography (CT) scans[99].

Table 4.1: dielectric and thermal properties of tissues at 434 MHz.

Tissue	ϵ_r	σ(S m^{-1})	ρ(kg m^{-3})	c(W m^{-1} °C^{-1})	Q(W/kg)	k(J kg^{-1} °C^{-1})	ω(ml min^{-1} kg^{-1})
Internal air	1	0	1.2	-	-	-	-
Bone	13.1	0.09	1908	1313	0.15	0.32	10.0
Fat	11.6	0.08	911	2348	0.51	0.5[a]	255.0[a]
Muscle	56.9	0.81	1090	3421	0.96	0.4[a]	442.8[a]
Tumour	59.0	0.89	1050	3950	-	1.5[a]	848.0[a]
Spinal cord	35.0	0.46	1075	3630	2.48	0.41[b]	1815.5[c]
Brain	56.8	0.75	1045	3696	15.5	0.44[b]	8644.6[c]
Sclera	57.4	1.01	1032	4200	5.89	0.47[b]	4303.4[c]
Vitreous humor	69.0	1.53	1005	4047	-	0.48[b]	-
Lens	37.3	0.38	1076	3133	-	0.35[b]	-
Optical nerve	35.0	0.46	1075	3613	2.48	0.40[b]	1815.4[c]

Note: Q is the metabolic heat generation rate. [a]Derived from patient-group optimization of thermal tissue properties based on invasively measured temperatures[101].
Value in[48] scaled 0.8-fold[b] or 11.3-fold[c] to account for thermal stress.

4.2.3 EM modeling

EM computations were performed using the finite difference time domain (FDTD) solver of SEMCAD X *. A uniform gridsize of 1.3 mm, a 40 mm padding and medium strength UPML boundaries were chosen. Antennas were excited by a sinusoidal signal of 15 periods, using optimized phase and amplitude settings that correspond to the maximum forwarded power during HT treatment. Dielectric tissue properties were assigned to each tissue according to the ITIS material parameter database[48] (Table 4.1). We used the applicator efficiency ($\eta_{HYPERcollar}$) of 0.4 for the HYPERcollar system which was calculated by using the interstitial temperature measurements obtained from clinical treatments[2].
In the current study, we calculated the maximum psSAR$_{10g}$, in shape of a cube, over treatment for SAR dosimetry.

4.2.4 Thermal modeling

The SAR-induced temperature rise was calculated for the selected patients using transient temperature simulations in SEMCAD X according to Pennes bioheat equation. We applied a mix of convective and Neumann (fixed flux) boundary conditions at the tissue-surrounding air, tissue waterbolus and tissue-internal air interfaces. The initial temper-

*SEMCAD X EM Simulation, version 14.8.4 (www.semcad.com).

ature in the tissues was set to 37 °C while the temperature of the surrounding air and the waterbolus was set to 20 °C as measured during hyperthermia treatments. To apply actual treatment power steering in the temperature simulation, user-defined sources were created for which the treatment phase and amplitude settings were applied to each antenna and the combined EM field was used to compute the SAR. The scaling factor of the source was the applicator efficiency factor (0.4). The assigned thermal tissue properties are shown in Table 4.1. We took thermal tissue properties under thermal stress into account. The assigned properties for muscle, fat and tumour were derived from[101], in which thermal conductivity (k) and perfusion (ω) values for these tissues were optimized based on invasive thermometry in ten H&N patients. Since the k and ω of the brain and eye tissues under thermal stress are unknown, we mimicked this variation by applying the same variation as the variation in muscle tissue. Going from a baseline value (no thermal stress)[48] to the optimized value under thermal stress[101] an increase of 0.8 fold (k) and 11.3 fold (ω) was applied (Table 4.1). This scaling for eye and brain tissues is reasonable because our current study shows that high local EM and thermal doses are induced in the eyes and our previous study on the brain exposure[2] shows very high psSAR levels (up to 140 W/kg). Note that the values of (k) and (ω) were optimized by applying the same applicator and applicator efficiency as used in this study ($\eta_{HYPERcollar}$=0.4).
Besides the absolute temperature, thermal tissue damage is also determined by the exposure time[30,31,97,110]. Therefore, the temperature increase averaged over the steady-state duration (60 minutes) of HT treatment at the location of the maximum achieved temperature ($T_{ss}(@T_{max})$) was used for thermal dosimetry:

$$T_{ss}(@T_{max}) = T_{ss}(\overline{r} = \overline{r}_{T_{max}}), \overline{r} = (x, y, z), \tag{4.1}$$

4.2.5 Sensitivity analysis

We investigated the influence of the modeling parameters and simulation settings on the induced $psSAR_{10g}$ and $T_{ss}(@T_{max})$ in the eyes for the patient with the worst case exposure of the eye, i.e. with the highest SAR and temperature in the eye. The investigated influence quantities and their studied range of variations are indicated in Tables 4.2 and 4.3. For each influence quantity, three different values were studied, i.e. a HTP was performed using average and ± one standard deviation of the literature value. The individual standard uncertainty (u_i) was quantified in $|\Delta psSAR_{10g}|$ and $|\Delta T_{ss}(@T_{max})|$ and obtained by determining the confidence interval from plus to minus one standard deviation, using the average literature value as reference. The square-root of the sum of squares to the u_i values was applied to obtain the combined standard uncertainty (u_c). The uncertainties were determined based on the assumption that the applied variations can be described by Gaussian probability functions. A coverage factor k of 2 was used to obtain the expanded uncertainty U within the 95% confidence interval.
For the standard uncertainty of the source power, we used the uncorrelated combined standard uncertainty of the induced SAR from Table 4.2.
An important source of uncertainty is the WB connection with the eyes during treatment

Table 4.2: EM modeling parameters and their uncertainties as used in the sensitivity analysis. ϵ_r is the relative dielectric permittivity, σ is the effective electric conductivity, ρ is the volume density of mass. The uncorrelated standard uncertainty (u_c) and the expanded uncertainty (U) is measured with $|\Delta psSAR_{10g}|$ in Eye-tissues. k is the coverage factor for the confidence interval.

Parameter	value	studied range	$\lvert\Delta psSAR_{10g}\rvert(u_i)$[%]
Applicator efficiency	0.4[a]	14%[a]	13.9
WB-eye connection	-	No - full contact	5.5
Discretization	1.3 (mm)	1-1.3 (mm)	2.3
Eye-tissue properties			
(a) ϵ_r	Table 1	15%[b]	3.6
(b) σ	Table 1	25%[b]	12.7
(c) ρ	Table 1	6%[b]	3.2
u_c (Source power)			20.3
U (k=2)			40.6

[a]Derived from[2]. [b]Derived from the ITIS Foundation tissue database[48].

which varies from the simulated model due to WB shape variations. Because the WB shape is difficult to define and varies considerably between and during treatments, we studied the worst case scenario by comparing the results of simulations with full versus no WB-eye connection.

The effect of the spatial discretization was determined by simulating the grid step 1 mm as reference, assuming that $\Delta_{grid} \to 0$ leads to the most accurate result. Decreasing the gridsize increases the computation time dramatically so we selected the reference of 1 mm as a balance between computational time and accuracy.

Tissue properties in patients deviate from literature values, e.g. due to age-dependency, post-mortem changes, and measurement uncertainty. In the current study, we derived the uncertainty of all tissue properties from literature[48]. Under thermal stress the blood perfusion of the tissues increases. Lang et al. developed a model to describe temperature dependant blood perfusion variation[68]. They used special functions for fat, muscle and tumour which follow in temperature range of 37-44 °C behaviors introduced by Song et al.[90]. Hence, for blood perfusion, for which we combined the variation at baseline and variation due to temperature increase, i.e. the range of variation for blood perfusion was estimated as 38% which is combination of the uncertainty at baseline (35%) and the uncertainty due to maximum deviation from the optimized temperature (39 °C) in[101] as estimated using the Lang model (16%).

The uncertainty in heat transfer coefficients and blood parameters were derived from[10] and[5].

Table 4.3: Thermal modeling parameters and their studied range of variation as used in the sensitivity analysis. c is the specific heat capacity , k is the thermal conductivity, ρ is the volume density of mass, ω is the volumetric blood perfusion rate, ρ_b blood density, c_b blood-specific heat, T_b blood temperature, $h_{air-skin}$ and $h_{bolus-skin}$ and $h_{internalair-lung}$ heat transfer coefficients, T_{air} surrounding air temperature, T_{bolus} bolus temperature, $T_{internalair}$ internal air temperature. The uncorrelated standard uncertainty (u_c) and the expanded uncertainty (U) is measured with $|\Delta T_{incr,max}|$ in Eye-tissues. k is the coverage factor for the confidence interval.

Parameter	value	studied range	$\lvert\Delta T_{ss}(@T_{max})\rvert(u_i)[\%]$
Source power	SAR profile (W/kg)	±20.3%	21.3
WB-eye connection	-	No - full contact	3.7
Discretization	2 (mm)	1 - 2 (mm)	0.9
Eye-tissue properties			
(a) c	Table 1	±13%[a]	2.3
(b) ρ	Table 1	±6%[a]	1.6
(c) k	Table 1	14%[a]	13.4
(d) ω	Table 1	38%[b]	9.9
Boundaries			
(a) $h_{air-skin}$	20 (W m^{-2})	±30% [d]	<0.1
(b) $h_{bolus-skin}$	82 (W m^{-2})	±30% [d]	<0.1
(c) $h_{internalair-lung}$	50 (W m^{-2})	±30% [d]	<0.1
(d) T_{air}	20 (°C)	1°C [c]	<0.1
(e) T_{bolus}	20 (°C)	1°C [c]	<0.1
(f) $T_{internalair}$	37 (°C)	1°C [c]	0.1
Blood parameters			
(a) Heat capacity ($c_b.\rho_b$)			5.1
ρ_b	1050 (kg m^{-3})	±2%[c]	
c_b	3617 (W m^{-1} °C^{-1})	±8%[c]	
(b) T_b	37 °C	0.5°C [c]	11.8
u_c			30.3
U (k=2)			60.7

[a]Derived from the ITIS Foundation tissue database[48].[b]Derived from[101]. [c]Derived from[10]. [d]Derived from[5].

4.2.6 Correlation between the induced SAR and temperature

To determine the appropriate metric for protecting against RF heating effects, we verified the correlation of high SAR levels with high-temperature levels. To simplify the correlation

analysis, we computed the least-squares regression coefficient (R^2) of the linear fits of $T_{ss}(@T_{max})$ as a function of psSAR_{10g}.

4.2.7 HT-related acute ocular effect

Treatment toxicities are scored by the grading system of the National Cancer Institute [†] to uniformly score the toxic acute and subacute effects of cancer therapy. The Common Toxicity Criteria (CTC) scores are concerned with the physiologic and functional endpoints, many of which are transitory and reversible. A grading (severity) scale is provided for each adverse effect term (Table 4.4).

All HT patients in our clinic are questioned by physicians before a treatment starts (baseline) and after each treatment session, leading to CTC scores for toxicity and pain. In addition, at the beginning of each HT session, patients are asked to describe how the treatment has affected them in the time between treatment sessions (active open questioning). Therefore, we receive patients' feedbacks on any health problem. In the current study, we evaluated the possibility of serious HT-related acute ocular damage by studying the CTC scores of the selected patients. Any treatment-related adverse event experienced by a patient was graded between 0 to 5 with a conservative attention for eye related toxicity using the specific terms in the CTC standard. In addition, for one patient with the worst case exposure, i.e. the highest $psSAR_{10g}$ in the eye, functional changes were investigated by performing a regular ophthalmology test prior to, during and after the HT treatment (immediately and up to 18 months after). This patient had four HT sessions in two weeks and was treated for long duration (70-80 minutes each) with high power (average of the forwarded power during treatment was 400 W).

4.3 Results

4.3.1 Sensitivity of EM and thermal modeling

Tables 4.2 and 4.3 summarize the impact of various EM and thermal modeling parameters on the calculated $psSAR_{10g}$ and $T_{ss}(@T_{max})$. The total expanded uncertainty of the $psSAR_{10g}$ predictions (95% confidence interval) is 40.6%, which is mainly due to the uncertainties of applicator efficiency and electrical conductivity of the eye tissues. Consequently, the critical factor in thermal modeling is the uncertainty in the SAR profile. This factor as well as the variations in eye thermal conductivity and blood parameters are the dominant factors in creating the expanded uncertainty of 60.7% in temperature predictions.

[†] http://ctep.cancer.gov/protocolDevelopment/electronic_application/ctc.htm.

Table 4.4: Observed acute toxicity for the selected HT patients with a conservative attention for eye related toxicity. Note that the number of incidents were counted, i.e. not just one incident per patient, so every treatment session always led to one CTC-score.

Nr of patients: 16
Total Nr of HT sessions:74

	Grade	0	1	2	3	4	5
	Pain in Eye	69	5	0	0	0	0
general CNS	Pns motory	74	0	0	0	0	0
	Pns sensory	73	1	1	0	0	0
	Headache	70	3	1	0	0	0
	Dizziness	73	1	0	0	0	0
	Nausea	71	2	1	0	0	0
	Vomiting	72	2	0	0	0	0
Subcut burns	Subcut skin	70	2	0	2	0	0
	Subcut fat	72	0	2	0	0	0
	Subcut muscle	72	0	2	0	0	0
	Subcut bone	69	1	3	1	0	0

Grade 0: No adverse event or within normal limits.
Grade 1: Mild adverse event; intervention not indicated.
Grade 2: Moderate adverse event; minimal, local or noninvasive intervention indicated.
Grade 3: Severe or medically significant but not immediately life-threatening.
Grade 4: Life-threatening or disabling adverse event; urgent intervention indicated.
Grade 5: Death related to adverse event.

4.3.2 HT-related acute ocular effect

Table 4.4 contains the CTC grades of the observed acute toxicity occurred during all HT treatment sessions for the selected patients. It shows that from 74 HT sessions for the selected patients, no grade 4 or 5 toxicities were observed and the three CTC grade 3 incidents were all subcutaneous burns that healed without any further medical attention. Two incidents of CTC grade 2 were observed regarding nausea and headache which were not associated with the eyes. Hence, eye related toxicities did not exceed CTC grade 1 in any of the patients. In addition, there was no self reported vision loss.
Pre-treatment and post-treatment ophthalmology testing of the patient with the worst case exposure showed that lenses were clear and hence no indication of cataracts was observed. In addition, no feedback on the development of cataract in the long term was

received for any treated patient.

4.3.3 Induced psSAR and temperature rise in the eyes during H&N HT treatment

Figures 4.2 and 4.3 show the scatter plots of the maximum calculated psSAR_{10g} and $T_{ss}(@T_{max})$ in the eyes during H&N HT treatments versus maximum CTC grade for non-burns adverse effects per patient. Square markers represent the scored grades for pain in the eye. Since general CNS-related adverse effects (pns. motory and pns. sensory, headache, dizziness, nausea, vomiting) may stem from eye problems, we also showed the scatter plot of the induced doses versus general CNS responses using circle markers. Note that Figures 4.2 and 4.3 demonstrate only the maximum scored CTC grade per patient whereas Table 4.4 includes grades of all incidents of acute effects for all HT treatment sessions. Since patients are treated under supervision of medical physicians, the results are only compared to the ICNIRP and IEEE basic restrictions for occupational environment (10 W/kg). Figure 4.2 shows that the maximum psSAR_{10g} in the eyes reaches up to 104 W/kg on average and 62 W/kg if considering lower limit of the 95% confidence interval, i.e. the induced EM dose in the eyes exceeds the basic restrictions by at least up to 6.2 times. For the lower uncertainty bound, the basic restrictions are exceeded for 12 of 16 patients.
The calculated temperature increases are compared to the basic restriction of 1°C on peak tissue temperature increase (green dashed-line) and also to the functional threshold of 5.2°C based on[110] (red dotted-line). Figure 4.3 shows that the maximum $T_{ss}(@T_{max})$ on average is 4.2°C and at the lower limit of the 95% confidence interval is 1.8°C. We also found that the predicted peak temperatures were located in vitreous-humor of the eyes. In addition the maximum estimated CEM43°C thermal dose in the lens is 0.56 minutes which is 38 times lower than the functional threshold of 21.3 minutes above which thermal damage has been observed in other studies. Comparison of figure 4.2 and 4.3 demonstrates that exposure exceeding the basic restrictions on psSAR_{10g} may not lead to temperatures exceeding the functional and even basic thresholds, e.g. from 12 patients with excessive eye exposure, 10 cases did not exceed the functional thermal threshold, with 95% confidence.

4.3.4 Correlation between the induced SAR and temperature

Figure 4.4 indicates a strong and positive correlation between $T_{ss}(@T_{max})$ and psSAR_{10g} for the selected patients, which is confirmed by a high correlation coefficient ($R^2 = 0.88$). However, there is a very large uncertainty in the residual error of the linear fit, i.e. 95% confidence interval for the residuals is 129%.

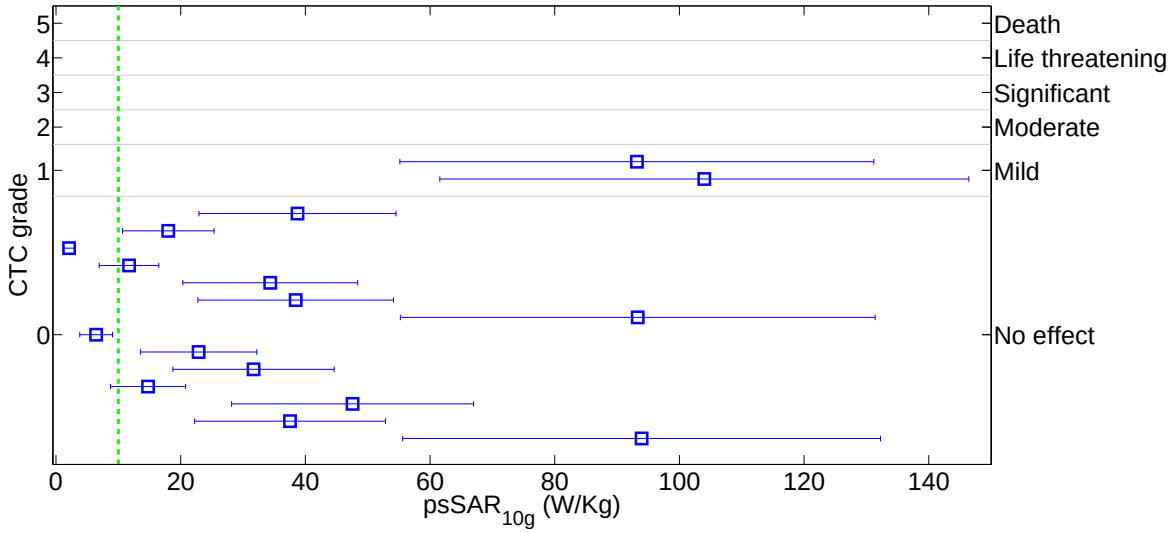

(a)

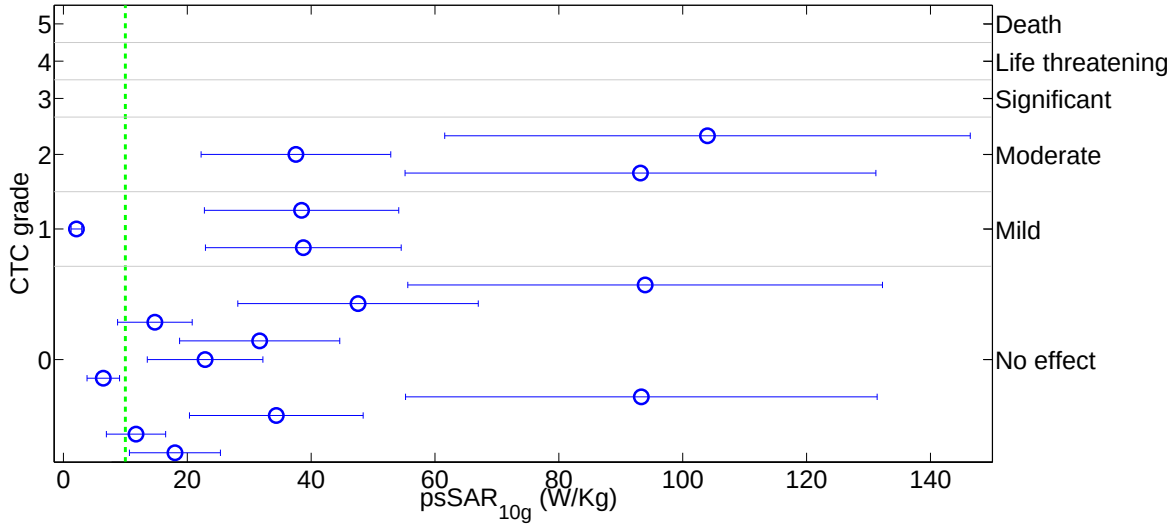

(b)

Figure 4.2: Scatter plot of the maximum induced $psSAR_{10g}$ in the eyes of the selected patients during H&N HT treatment vs the **maximum** CTC grade for pain in eye (a) and general CNS effects (b). The markers display the adverse effects versus $psSAR_{10g}$ in the eyes and the errorbars indicate the calculated 95% confidence interval of the uncertainty. The markers are demonstrated in 5 groups based on their CTC grades. The results are compared to the occupational basic restrictions.

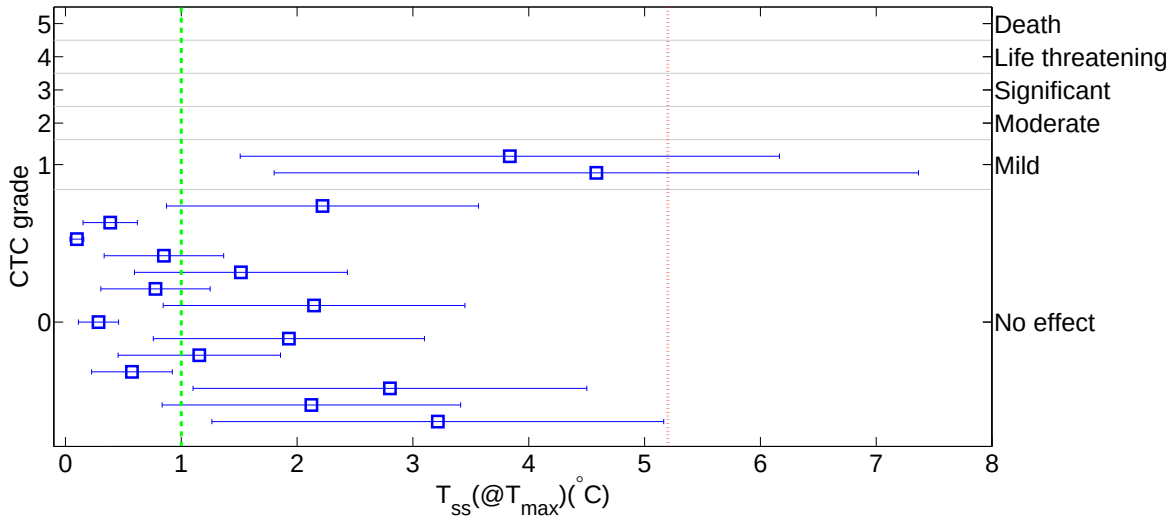

(a)

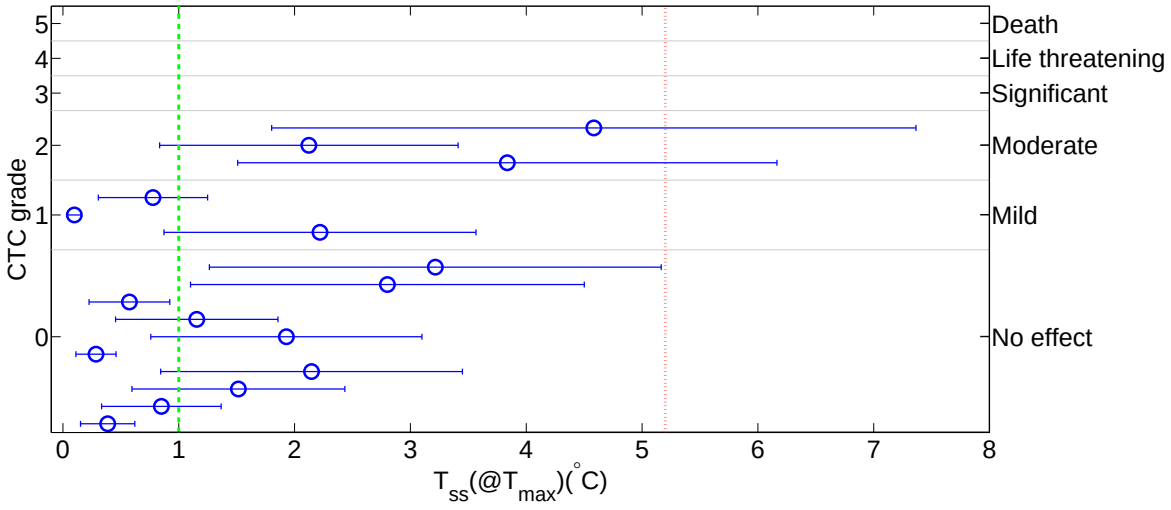

(b)

Figure 4.3: Scatter plot of the $T_{ss}(@T_{max})$ in the eyes of the selected patients during H&N HT treatment vs the **maximum** CTC grade for pain in eye (a) and general CNS effects (b). The markers display the adverse effects versus $T_{ss}(@T_{max})$ in the eyes and the errorbars indicate the calculated 95% confidence interval of the uncertainty. The markers are demonstrated in 5 groups based on their CTC grades. The results are compared to the basic (green dashed-line) and functional (red dotted-line) thermal threshold of the eye.

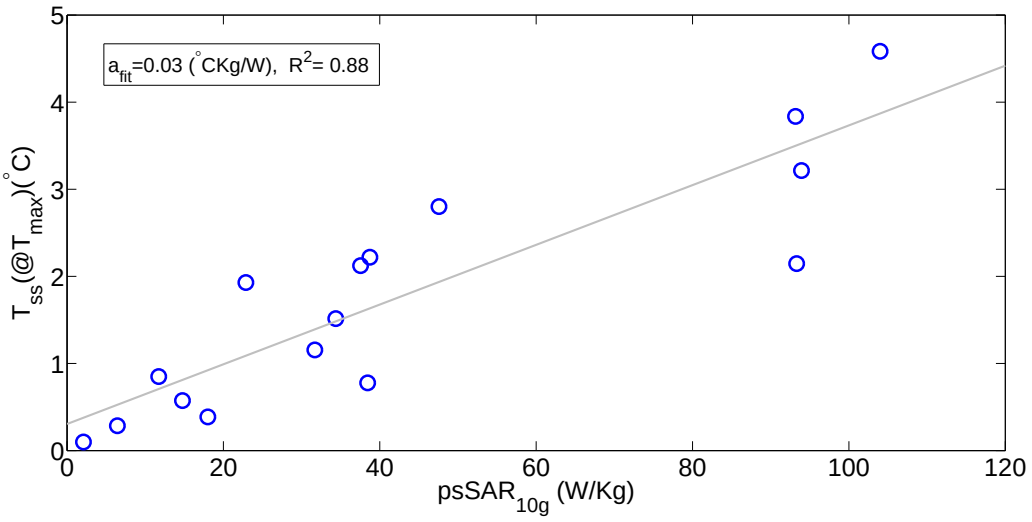

Figure 4.4: Correlation of $T_{ss}(@T_{max})$ to psSAR_{10g} for the selected patients. The linear fit parameters are represented by the slope (a_{fit}=ΔT/ΔSAR) and the goodness of the fit (R^2).

4.4 Discussion

The current guidelines of ICNIRP and IEEE aim at limiting excessive localized tissue heating by providing restrictions on psSAR_{10g}. The eyes are particularly vulnerable to RF heating because of the relative lack of available blood flow to dissipate the excess heat load. Therefore, the sensitivity of the visual organ to RF electromagnetic induced heat was amongst the main concerns when developing the RF safety standards. Clearly, the motivation was to prevent formation of lens opacity: cataracts. However, the current safety guidelines are based on experimental data obtained from animals. In the current study, we analyzed the association of high EM (psSAR_{10g}) and thermal ($T_{ss}(@T_{max})$) dose in the human eye with acute ocular effects. Since the thermal tissue damage is determined by induced temperature and also exposure time, we calculated the thermal dose by averaging the peak temperature increase over 60 minutes of steady state duration in HT treatment. To evaluate the association of HT-induced SAR and temperature increase in the eyes with acute ocular effects, we studied the common toxicity criteria (CTC) data reported for the treated patients. The condition of the patients at baseline, during and after each treatment section were checked by the physicians using the CTC guidelines. Moreover, the worst case patient, with the highest SAR and temperature in the eye, was examined by regular ophthalmology investigations prior, during and up to 18 months after HT treatment. The results show that the maximum predicted induced psSAR_{10g} and $T_{ss}(@T_{max})$ in the eyes of the 16 selected patients during H&N HT treatment exceed the basic restrictions[55,57] for occupational environments on psSAR_{10g} and peak tissue temperature by up to 10.4 and 4.6 times on average. Considering the uncertainties in the model parameters, these values are 6.2 and 1.8 times at the lower limit of the 95% confidence interval ($k = 2$)

(Figure 4.2, Figure 4.3). Analysis of the CTC-scored database indicates that there is no evidence of serious (CTC grade 3 and more) acute HT-related ocular toxicity for any of the selected patients (Figures 4.2, 4.3 and Table 4.4). Pre-treatment and post-treatment ophthalmology testing also showed that there is no indication for cataracts. Therefore, based on the current CTC data, patients report and opthalmology result, we observed no indication for induction of cataracts or any serious acute ocular effect at SAR and temperature levels above the assumed thresholds. Note that the calculated temperature increase can exceed the functional level of 42.2°C[110] for 2/16 patients if considering the higher bound of uncertainty (Figure 4.3) and reach up to 7.4°C in vitreous humor tissue. To assess the influence of WB cooling effect on our results, we have calculated the temperature increase in the eye exposed to the same SAR but without connection to the WB, i.e. under normal environmental conditions where the common guidelines are intended to be applied that were modelled using a convective thermal boundary to air. The result shows that in the absence of WB, the $T_{ss}(@T_{max})$ increases by 7.6% which is within the expanded standard uncertainty. Given this small impact, we still expect that the mean temperature is affected just slightly and that the confidence interval is appropriate. Hence, our results are also valid under normal environmental conditions and not only when the eyes are subject to the WB.

Major problems in temperature assessment are the incorporation of the effect of blood flow and a realistic and detailed implementation of the anatomy with the correct thermal properties for the individual tissues. In this study, we used detailed segmented anatomical model of the eye based on the CT-scans of the patients and the assigned thermal properties of the tissues incorporate the strong thermoregulatory response of H&N tissues under thermal stress. However, a number of limitations may have affected our results. Firstly, we used the Pennes bioheat equation, which uses a homogeneous heat-sink term and does not incorporate vasculature. Many studies attempted to model more complicated mechanisms, such as the impact of discrete vasculature and metabolism effects[8,26,50–52]. Flyckt constructed a DIscrete VAsculature (DIVA) model of the eye and showed that the Pennes bioheat model serves as an appropriate thermal model for predicting low temperature rises. At higher temperature rises, we expect that the DIVA model leads to a lower sclera temperature due to the increase in blood perfusion under thermal stress. Therefore our results will be valid even by inclusion of vasculature because, based on our simulations, the peak temperature rises were located in vitreous humor body of the eyes. Secondly, we did not take the influence of vitreous humor convection into account. Since the calculated temperature for vitreous humor is higher than sclera, we expect that consideration of convection leads to a higher sclera temperature and a lower vitreous humor temperature. Karampatzakis and Samaras[61] showed that the most notable effect of consideration of convective heat transfer of eye fluid is that the coolest area of the cornea moves at a point of 2 mm inferior to its geometric centre. Hence, the effect of humor flow on the amount of the induced temperature was negligible. Finally, we note that, as acute toxicity in this study is scored based on patient responses to physicians, i.e. subjective complaint scores, it does not rule out sub-clinical adverse effect in the eyes. Therefore, further research is required to study more subtle functional changes, e.g. by performing ophthalmological

follow-ups for more patients.
To verify the appropriateness of the $psSAR_{10g}$ as a metric for protecting against RF heating effects, we assessed the correlation of $T_{ss}(@T_{max})$ to $psSAR_{10g}$. The results of linear regression show that they are strongly and positively correlated (R^2=0.88). However, a same SAR level may result in different temperature increases in different eye sizes and anatomies. The uncertainty of predictions using the fit exceeds that of the actual simulated temperatures (129% vs 61%), which advocates using 3D temperature simulations in stead of SAR values. Hence, the best metric for setting the safety guidelines remains the peak temperature increase over a specific duration. In addition, the uncertainty in thermal modeling can be reduced by improving the individual uncertainties, i.e. specifically the EM source by reducing setup errors and improving treatment reproducibility of the HYPERcollar applicator, like in our novel HYPERcollar3D applicator[81,95]. By this step, in future, we will be able to provide even better estimates of the temperature distribution.

4.5 Conclusions

Experimental data on adverse RF heating effects in humans is of great potential value for health and standards agencies to develop safe limits of RF exposure. The current study provides initial data on association between exposure level and functional changes in the human eyes, which is considered as a highly sensitive tissue in setting RF safety guidelines and regulations. We investigated the peak local SAR and temperature increase in the eyes from prolonged exposure to deep RF head and neck hyperthermia. Our data shows that, exposure exceeding the basic restrictions on $psSAR_{10g}$ by at least up to 6.2 folds leads to peak temperature increase of at least up to 1.8°C in the eye averaged over 60 minutes steady state duration of the treatment. No indication for cataracts or any serious acute ocular damage was observed upon this exposure. Therefore, our data confirms that the current guidelines provide adequate protection against excessive temperature increase in the eyes from exposure to RF EMF. The correlation study further shows that the uncertainty in modeling the relationship between temperature increase and $psSAR_{10g}$ is higher than the uncertainty in 3D temperature modeling. Hence in our view, future guidelines require restrictions on peak temperature increase for specific duration of exposure instead of restrictions on $psSAR_{10g}$.

CHAPTER 5

SAR thresholds for electromagnetic exposure using functional thermal dose limits

This chapter is based on:
F Adibzadeh, MM Paulides and GC van Rhoon. SAR thresholds for electromagnetic exposure using functional thermal dose limits.
Submitted to Int J Hyperthermia, 2016.

Abstract

Purpose: *To quantify the magnitude of safety factor included in the current basic restrictions on specific absorption rate (SAR) in tissues for different exposure scenarios based on thermal damage threshold. The current basic restrictions incorporate large safety factors which are generally conservative. The magnitude of safety margin for various radiofrequency localized exposure scenarios is unknown. This shortcoming becomes more critical for medical applications where the safety guidelines are required to be relaxed.* ***Materials and methods:*** *Hereto, for each exposure scenario, we used the lowest thermal dose (TD) required to induce acute local tissue damage reported in literature, calculated the corresponding TD-functional SAR limits (SAR_{TDFL}) and related these limits to the basic restrictions, thereby estimating the respective safety factor.* ***Results:*** *The margin of safety factor in the current basic restrictions on $psSAR_{10g}$ is large, i.e. up to 31.2 depending on exposure duration and hotspot-size.* ***Conclusions:*** *Our analysis can be converted into clear indications of SAR_{TDFL} for different exposure scenarios, e.g. 150 W/kg for hyperthermia applications (60 min exposure and a target size of 4 cm in diameter). The benefit of a quantitative safety factor is that it facilitates decision making on how much the responsible investigator can increase local SAR with an acceptable risk of thermal damage.*

5.1 Introduction

To avoid excessive heating in tissues, ICNIRP and IEEE organizations have defined guidelines for limiting human exposure to electromagnetic fields (EMF)[55,57]. Based on these guidelines for a radiofrequency (RF) range of 100 kHz−3 GHz, exposure should not result in peak spatial average SAR (psSAR) that exceeds 10 W/kg as averaged over any 10 g of tissues ($psSAR_{10g}$). This level applies to exposure of persons in occupational environments, i.e. trained adults under controlled conditions. The foundations of the guidelines are biological RF dose effect studies using rodent and non-human primate models. To account for uncertainties in the data and to provide a large margin of safety for other limiting conditions such as high ambient temperature, humidity, or level of physical activity and also to increase confidence that the standard is below the levels at which adverse effects could occur, the local SAR threshold is lowered by an arbitrary safety factor: at least a safety factor of 10 and probably considerably more if the remarkable tolerance in human studies is accepted as generally valid. Therefore, these guidelines introduced safety factors to assure that any effect, both reversible and irreversible, is avoided. However, in some applications, such as medical imaging or therapy, taking more risk is permissible if this provides a better diagnosis or therapeutic effect. For instance, in hyperthermia

(HT) cancer therapy and magnetic resonance imaging (MRI), the goal is to balance the probability of cure, or the correct diagnosis, versus the probability of side-effects. Furthermore, this exposure is only permitted for a specific duration and under control of medical doctors. In this respect, we recently performed dose-effect relations studies and showed that exceeding the basic restrictions (i.e. 10 W/kg) by up to at least 14 (brain[2]) and 10 (eyes[3]) times during hyperthermia treatment in head and neck (H&N) region, showed no indication for any serious acute effect for any of the treated patients. Clearly, medical applications are very different than the domestic applications with respect to the safety standard guidelines. This difference is reflected in the suitability of a much smaller safety factor. However, the relevance of the magnitude of the safety factor for a certain localized exposure scenario is unknown and might be restrictive for the functionality of the exposure purpose. Especially, in HT and MRI there is a need to more exactly identify the incorporated safety factor and to tailor EM exposure thresholds by expanding the safety limits.
The main objective of the current study was to assess the safety factor incorporated in the current ICNIRP and IEEE basic restrictions for various localized exposure scenarios. To achieve this goal, we first translated the functional thermal dose (TD) required to induce acute local tissue damage reported in literature (Table 5.1) into corresponding TD-based functional SAR limits (SAR_{TDFL}). The ratio between these SAR_{TDFL} values and the basic restrictions, leads to the respective safety factor. Hereto, we calculated the SAR_{TDFL} for localized exposure, i.e. calculated in a hotspot-mimicking sphere, inside tissues based on the Pennes bioheat equation (PBE) (Figure 5.1). Secondly, we performed a sensitivity study to assess the changes in the calculated SAR_{TDFL} due to exposure parameters. Thirdly, we evaluated our results by comparing the SAR_{TDFL} to SAR levels in realistic clinical situations. Finally, we proposed a simple procedure to decide what SAR level would be acceptable under a certain exposure scenario.

5.2 Methods

In the current study, we calculated the lowest SAR_{TDFL} values necessary to induce heating up to T_{thresh} at the centre of the hotspot-representing sphere (focus) within a 37°C medium (Figure 5.1). T_{thresh} is the corresponding temperature to the lowest thermal dose per tissue type, in units of cumulative equivalent minutes at 43°C (CEM43°C), that results in thermal tissue damage, derived from our previous study[97] (Table 5.1). The SAR_{TDFL} was calculated using the partial differential equations (PDE) toolbox in MATLAB to solve the PBE. The PDE toolbox provides functions for solving partial differential equations in 2D, 3D and time using finite element analysis. Secondly, we assessed the sensitivity of SAR_{TDFL} due to changes in the focus diameter (as a result of changes in exposure frequency), exposure duration and thermal tissue properties. We calculated the SAR_{TDFL} for focus diameters of 20, 15, 10, 5, 2, 1 and 0.5 cm using various databases containing thermal baseline and thermo-regulated tissue properties[49,68,72,91]. We compared the value of SAR_{TDFL} among various available tissues in table 5.1, considering the worst case in

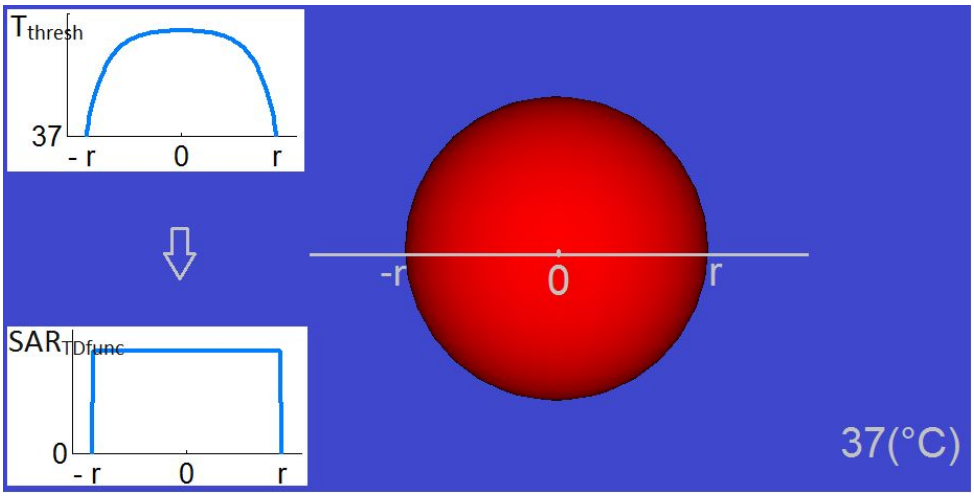

Figure 5.1: Picture of a modelled hotspot-mimicking sphere (focus) inside a tissue at 37(°C). Example of SAR_{TDFL} necessary to induce T_{thresh} (°C) heating, as shown in Table 5.1, at the centre of the sphere.

Table 5.1: Translation of the lowest tissue specific CEM43°C doses that result in thermal tissue damage in large animals and humans, to the corresponding temperature for exposure durations of 60, 30, 15 and 5 minutes.

Tissue	CEM43°C * (min)	T_{thresh}(°C)			
		t=60 (min)	t=30 (min)	t=15 (min)	t=5 (min)
Brain	7.5	41.5	42.0	42.5	43.6
Spinal Cord	30.0	42.5	43.0	44.0	45.6
Peripheral Nerve	45.5	42.8	43.6	44.6	46.2
Skin	288.0	45.3	46.3	47.3	48.8
Esophagus	120.0	44.0	45.0	46.0	47.6
Liver	9.9	41.7	42.2	42.7	44.0
Kidney	70.0	43.2	44.2	45.2	46.8
Bladder	90.5	43.6	44.6	45.6	47.2
Rectum	30.0	42.5	43.0	44.0	45.6
Prostate	30.0	42.5	43.0	44.0	45.6
Muscle	60.0	43.0	44.0	45.0	46.6
Fat	240.0	45.0	46.0	47.0	48.6

* Derived from[97].

which the focus volume is uniformly heated. By this simplification, the conduction term in PBE can be set to zero and hence the PBE can be solved analytically. To evaluate the influence of exposure duration on the results, we compared the SAR_{TDFL} for exposure duration of 60, 30, 15 and 5 minutes in spheres of 20, 5, 2 and 0.5 cm diameters in muscle using McIntosh (resting-condition) and Erasmus MC (thermal stress) databases for tissue properties. Finally, we evaluated our results by comparing the calculated SAR_{TDFL} values in the current study with simulated SAR using SEMCAD X (v.14.8.4, SPEAG, Zurich, Switzerland) inside a realistic anatomical model under exposure of RF EMF from head and neck (H&N) hyperthermia treatment.

5.2.1 CEM43°C thermal dose

The CEM43°C dose model expresses the thermal load on living tissues by estimating the equivalent induced thermal stress in minutes at 43°C. We translated the reported tissue specific CEM43°C thresholds to T_{thresh} based on the CEM43°C definition assuming a constant temperature over the duration of exposure:

$$CEM43°C = \sum_{i=1}^{n} t_i R^{(43-T)} \tag{5.1}$$

Where CEM43°C is the cumulative number of equivalent minutes at 43°C, t_i is the i-th time interval, R is related to the temperature dependence of the rate of cell death (R(T<43 °C)=1/4, R(T>43 °C)=1/2) and T is the average temperature during time interval t_i.

5.2.2 Pennes bioheat equation

Pennes bioheat equation (PBE)[83] is often used by researchers when calculating RF induced tissue temperature.

$$\rho c \frac{\partial T}{\partial t} = \nabla \cdot (k \nabla T) + \rho Q + \rho SAR - \rho_b c_b \rho \omega (T - T_b), \tag{5.2}$$

Here, T is the tissue temperature, t is the time, SAR is the specific absorption rate, ω is the perfusion rate, ρ is the density of the medium the volume, c is the specific heat capacity, k is the thermal conductivity, Q is the metabolic heat generation rate. The subscript $_b$ denotes a blood property, respectively.
The calculated SAR is directly dependent on the tissue property values as inputs for PBE. The dielectric parameters used were taken from the database of Gabriel et al.[34,35]. The thermal parameters were derived from various databases as shown in Table 5.2. For each calculation, we used the values of all the thermal parameters (specific heat capacity, thermal conductivity, density and blood perfusion) from one database. In case that a database, e.g. Lang and Erasmus MC, does not contain values of all parameters we took the missing parameters from the ITIS database.

5.2.3 Baseline and thermo-regulated tissue properties

If we compare thermal parameters with each other, we find small differences for density, specific heat, and thermal conductivity among various databases. For perfusion, however, differences are large because the literature values for blood perfusion are generally at resting condition (baseline temperature: 37°C), while values at high temperatures are completely different due to thermoregulatory response of tissues under thermal stress. For local hotspots above 20 W/kg psSAR10g, thermoregulated local perfusion is the most important parameter determining the RF induced temperature increase[64,71], and is also the major tissue response to hyperthermia[92]. Thermoregulatory processes show typical response times in the order of 10 minutes[43]. In the current study, we did not consider the transient effect of thermoregulation, i.e. always the values of parameters at steady state were used.
To consider the impact of local thermoregulation, data analysis was performed for:

Basal perfusion effectively modelling a completely dysfunctional thermoregulation, using the McIntosh and ITIS databases.

- *Literature summary by McIntosh:* McIntosh et al. standardized tissue thermal parameters by documenting 140 key papers and books and developed a database of the thermal properties for around 50 human tissues[72].

- *ITIS Foundation tissue database:* ITIS foundation took an inclusive approach and incorporated all studies with varying approaches and degrees of accuracy after eliminating studies with major flaws to increase the parameter sample size used. This database provides the average values and information about the variability of parameters[49].

Thermoregulated perfusion for muscle, fat and skin:

- *Sigma Hyperplan tissue database:* These values are provided by the hyperthermia treatment planning system HyperPlan and derived from the clinical application of deep pelvic hyperthermia with the Sigma-60 applicator. Typical values of thermal conductivity and perfusion are listed in Wust et al.[107], and empirically obtained values created by hyperthermia model-treatment comparison are found in Sreenivasa et al.[91], Wust et al.[108].

- *Temperature-dependent model by Lang:* Lang et al.[68] employed a temperature-dependent blood perfusion model based on preclinical measurement data of Song et al.[90] to improve the classical bio-heat term in PBE which assume a constant-rate blood perfusion within each tissue[68]. For each exposure scenario, we calculated the perfusion value based on Lang model using the corresponding T_{thresh} in Table 5.1.

- *Erasmus MC H&N database:* We calculated the effective perfusion for tumor, muscle and fat from the measurement data obtained during deep head and neck (H&N) HT treatments of nine patients that had interstitial catheters in the target region[86]. The effective perfusion was reconstructed based on the thermal washout technique from temperature decay measurements[87,103].

In summary, we assume that at resting condition, the databases of McIntosh and ITIS are more reliable because they are based on a large number of studies whereas, under thermal stress and other conditions that may increase perfusion, the databases/models of Erasmus MC, Hyperplan and Lang provide more reliable data as they take thermoregulated perfusion into account. In the current study, we took the Erasmus MC properties and exposure duration of 60 minutes as reference.

5.3 Results

5.3.1 Functional SAR limits SAR_{TDFL}: Influence of focus diameter, exposure duration and tissue thermal parameters

Figure 5.2 shows the calculated SAR_{TDFL} for various available tissues in table 5.1. The SAR_{TDFL} values were calculated assuming that tissues are uniformly heated. The figure indicates that muscle has the lowest SAR_{TDFL} value among tissues, applying the basal tissue property databases which are more comprehensive compared to thermoregulated databases. The thermoregulated databases are limited for this comparison. It also indicates that the SAR_{TDFL} increases significantly if the thermoregulated perfusion is applied. The maximum variation in calculated SAR_{TDFL} is seen in muscle, which shows a 10 fold increase in allowable SAR using the Erasmus MC tissue parameters rather than the lower perfusion McIntosh database. Figure 5.3 shows the impact of focus diameter and thermal tissue properties on the calculated SAR_{TDFL} in the muscle, fat and skin. These three tissues were selected as thermal hotspots occur most commonly in them during medical applications such as hyperthermia and MRI[74] and literature values are more abundant. The figures demonstrate the exponential increase in SAR_{TDFL} with decreasing sphere diameter, ie. the threshold allowable SAR increases 180 fold as spherical hotspot region decreases from 20 cm to 0.5 cm diameter. The figures also indicate that the variations in the calculated SAR due to the differences in thermal tissue properties among various databases are larger for bigger spheres, where the tissue blood perfusion is the dominant parameter, and decreases in small spheres, where the blood perfusion dominance disappears at the benefit of thermal conduction (figure 5.3). The maximum variation in the calculated SAR_{TDFL} due to differences in thermal parameters over various databases is in a sphere of 20 cm diameter in muscle, with a 12.5 fold increase using thermoregulated perfusion (Erasmus MC database) vs. basal perfusion (McIntosh database). The impact of surrounding tissue on the temperature at the center of sphere is less for bigger spheres and by using thermoregulated perfusion. Figure 5.4 shows the impact of exposure duration

Table 5.2: Thermal tissue properties based on McIntosch[72], ITIS[49], Hyperplan[91], Lang[68] and Erasmus MC[86] databases.

Tissue	Specific heat capacity, c (J/kg/°C)			Thermal conductivity, K (W/m/°C)			Density, ρ (kg/m^3)			Blood flow, ω (ml/min/kg)				
	Mc	ITIS	Hyper	Mc	ITIS	Hyper	Mc	ITIS	Hyper	Mc	ITIS	Hyper	Lang	Erasmus
Bladder	3514	-	3500	0.47	-	0.60	1132	-	1000	30	-	150	300	-
Brain	3653	3630	-	0.51	0.51	-	1046	1046	-	530	559	-	-	-
Eye cornea	3615	3615	-	0.50	0.54	-	1174	1051	-	0	0	-	-	-
Fat	2301	2348	3500	0.19	0.21	0.21	909	911	900	30	33	200	48	309
Kidneys	3786	3763	3500	0.54	0.53	0.58	1072	1066	1000	3960	3795	4000	4000	-
Liver	3507	3540	3500	0.51	0.52	0.64	1088	1079	1000	420	860	1000	1000	-
Muscle skeletal	3514	3421	3500	0.51	0.49	0.64	1102	1090	1000	30	37	300	180-240	457
Nerve	3452	3613	-	0.46	0.49	-	1112	1075	-	160	160	-	-	-
Skin	3310	3391	-	0.41	0.37	-	1114	1109	-	60	106	-	275*	-
Spinal cord	3452	3630	-	0.46	0.51	-	1112	1075	-	160	160	-	-	-
Esophagus	-	3500	-	-	0.53	-	-	1040	-	-	190	-	-	-
Rectum	-	-	-	-	-	-	-	-	-	-	-	-	-	-
Prostate	-	3760	-	-	0.51	-	-	1045	-	-	394	-	-	-

*Derived from[22] by overlapping the curve from Lang model[90] by the similar analytical expression as used for fat and muscle.

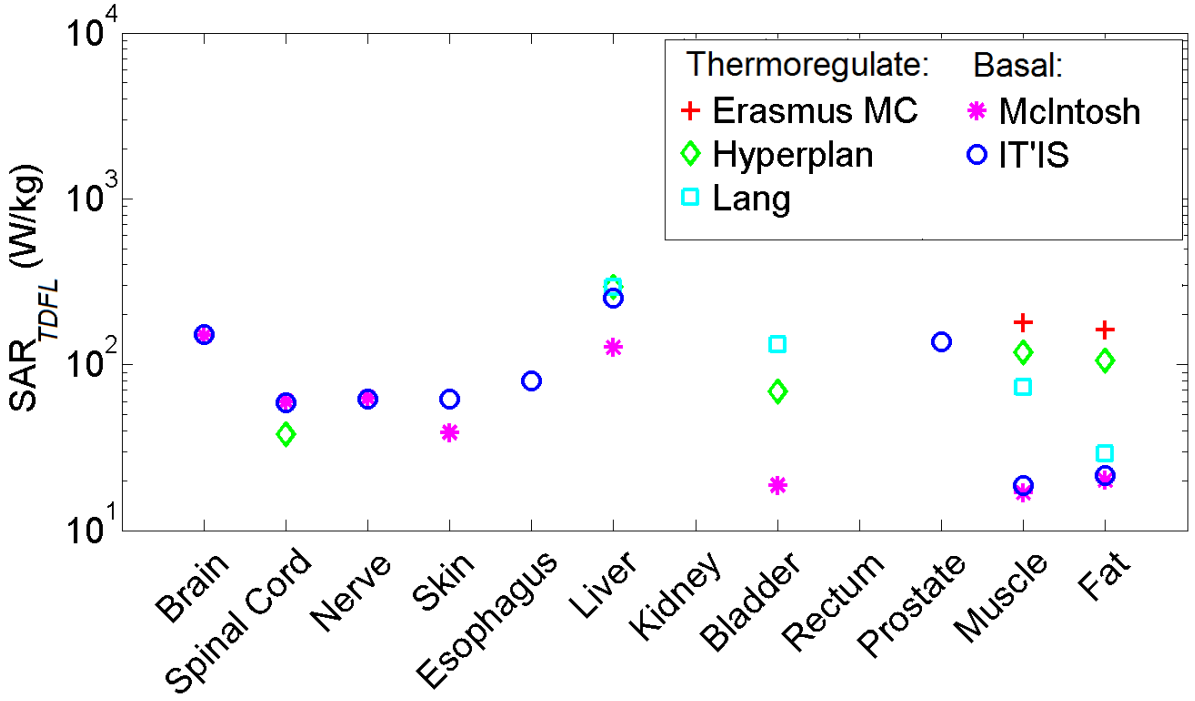

Figure 5.2: Comparison of SAR_{TDFL} among various tissues after 60 minutes exposure, using various tissue property databases. The SAR_{TDFL} values were calculated in the worst case assuming that the focus volume is uniformly heated.

on the calculated SAR threshold. It indicates that by reduction of exposure duration, the calculated SAR_{TDFL} in spheres increases, which is caused by the higher thresholds of temperature increase in tissues, i.e. according to the CEM43°C definition, shorter exposure duration requires higher temperature for the same CEM43°C thermal dose (equation 5.1). This increase is more pronounced in larger spheres than in small spheres. For exposure duration less than 10 min (thermoregulatory response time) only the basal thermal tissue properties were applied, i.e. McIntosh. The calculated SAR limit for muscle using McIntosh database increases by 10 fold by reducing the exposure duration from 60 to 5 min in a sphere of 20 cm diameter. This increase is lower for smaller spheres.

5.3.2 Validation of the SAR limits using clinical conditions

To validate the calculated SAR against clinical data, we compared our results to the simulated SAR for a realistic scenario in hyperthermia application. In our previous study we used detailed numerical EM and thermal simulations and showed that $psSAR_{10g}$=191.5

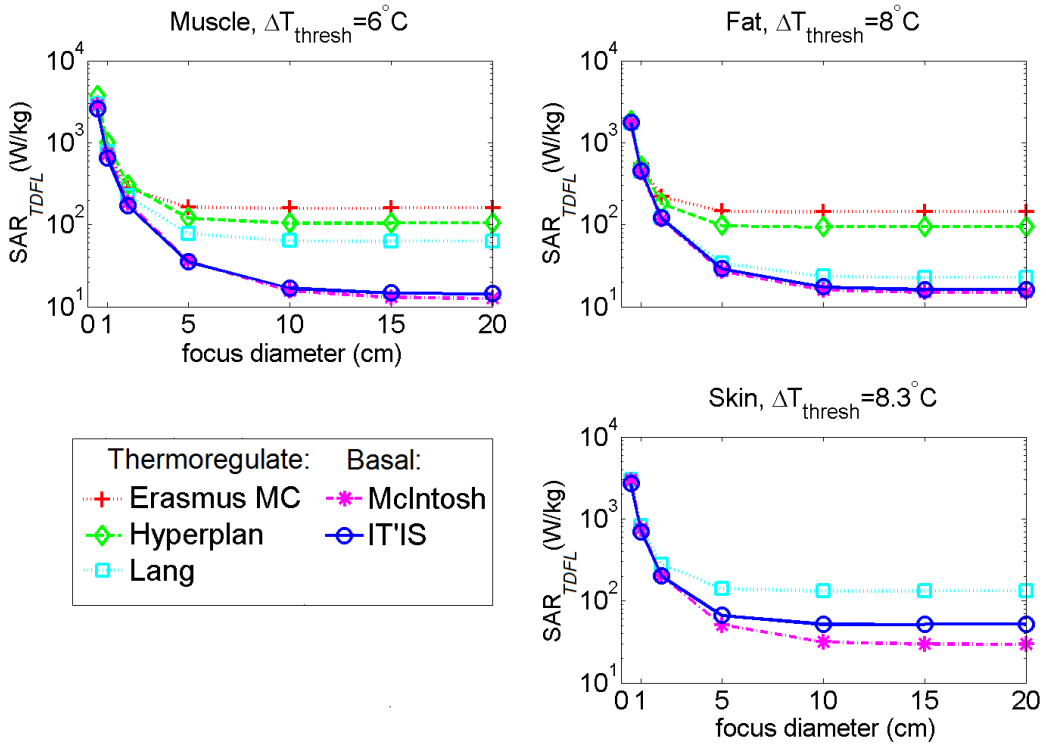

Figure 5.3: Impact of focus diameter on the SAR_{TDFL} for muscle, fat and skin using various databases for thermal tissue properties. The SAR_{TDFL} values were calculated for exposure duration of 60 minutes.

W/kg is required to induce a 6°C temperature increase in 10 g of muscle during 60 min of hyperthermia treatment in H&N[3]. 10 g of muscle is equivalent to a sphere of 2.6 cm diameter. The calculated SAR in a sphere of 2.6 cm using thermoregulated Erasmus MC database is 218.3 W/kg, which nicely matched the simulated $psSAR_{10g}$ (12% difference). The expanded uncertainty of the simulated result due to uncertainties in the modeling parameters was 23%. This indicates that the differences between the calculated versus simulated SAR (12%) is less than the uncertainty of numerical modeling (23%). We therefore conclude that our calculated SAR limits provide valid values.

5.3.3 Thermal-dose-based basic restriction definition procedure

Finally, we provide a decision making flowchart that demonstrates instructions to calculate the SAR limit (figure 5.5). Hereto we first need to determine the size of hotspot volume in a specific tissue which is estimated by the RF wavelength in a lossy dielectric or tissue[106]. For hotspots with diameter larger than 5 cm, the blood perfusion is

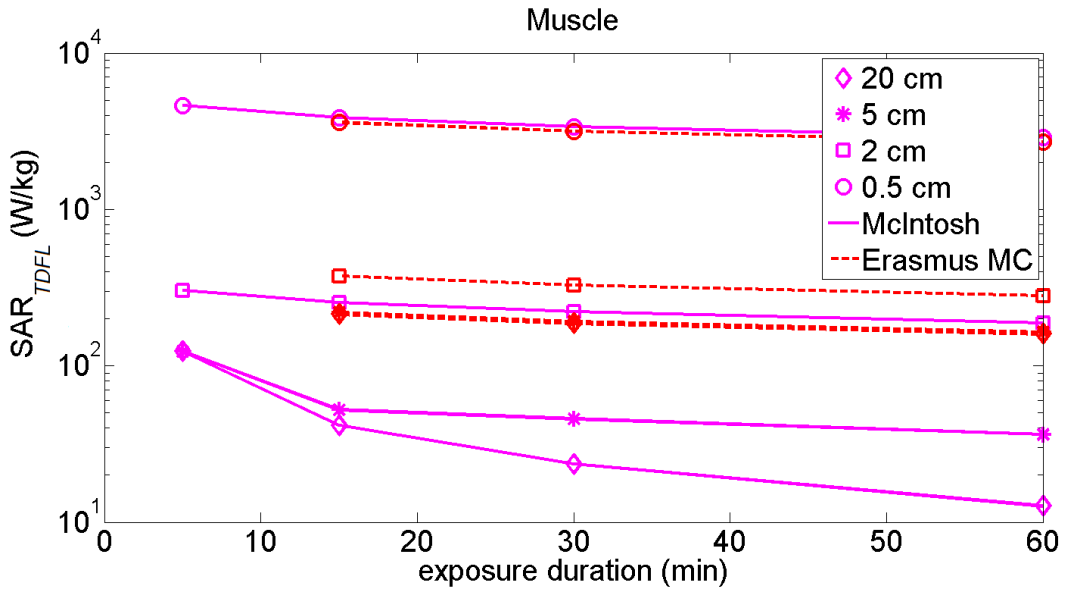

Figure 5.4: Impact of exposure duration on the SAR_{TDFL} after 60, 30, 15 and 5 minutes exposure in spheres of 20, 5, 1 and 0.5 cm diameter in muscle. The results are calculated for only basal (McIntosh) and thermoregulated (Erasmus MC) perfusions, considering 10 minutes delay in thermoregulatory process of tissue, i.e. there is no thermoregulated perfusion for exposure duration <10 min.

the most influential parameter. Therefore, thermal tissue properties under thermal stress (e.g., ErasmusMC, Hyperplan and Lang databases) should be used to calculate SAR when the exposure duration is longer than 10 minutes, and the thermoregulatory response of tissue is activated[43]. This excludes hotspots with a diameter less than 5 cm, since thermal conductivity is the determinant parameter that has similar values amongst the property databases. If the exposure duration is shorter than 10 minutes, we propose to use the databases for basal/resting conditions (e.g., McIntosh and ITIS).

5.4 Discussion

The current ICNIRP[55] and IEEE[57] safety guidelines on human exposure to RF EMF, incorporate large safety factors to protect against any potential adverse health effect. The

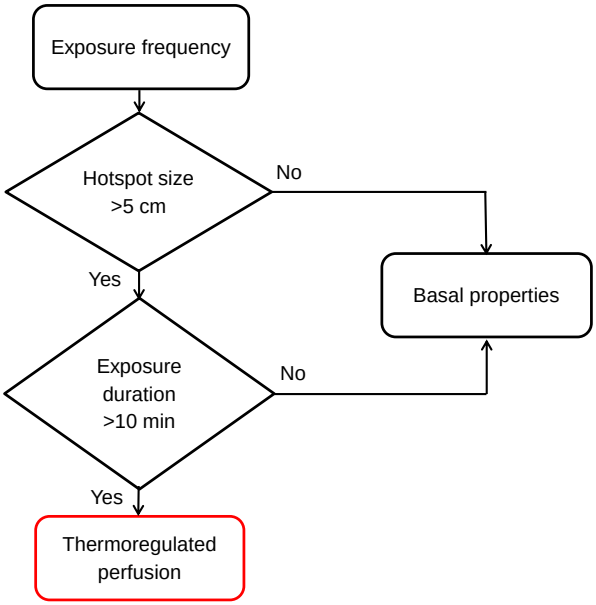

Figure 5.5: Instructions to calculate SAR_{TDFL} limit.

selection of a safety factor is based on informed expert opinion rather than a rigorous quantitative process. Therefore, the magnitude of safety for a certain localized exposure condition is unknown. The main objective of the current study was to assess and evaluate the relevance of the incorporated safety factor in the current basic restriction for various local exposure scenarios. To achieve this goal, we calculated the functional SAR limits (SAR_{TDFL}) based on the lowest thermal dose, in units of CEM43°C, that result in local acute tissue damage, derived from our recent study[97]. We translated these tissue specific CEM43°C limits into SAR_{TDFL} by solving the Pennes bioheat equation using MATLAB PDE solver. SAR_{TDFL} was calculated in a sphere of different diameters (0.5, 1, 2, 5, 10, 15, 20 cm) which represents localized RF hotspot for various exposure durations (60, 30, 15 and 5 min) and various databases of thermal tissue properties. Our results show that in order to arrive at the basic restrictions in the common generic guidelines, SAR_{TDFL} values for muscle are lowered by safety factors shown in table 5.3. Muscle was selected because comparison of the calculated SAR_{TDFL} among various tissues shows that muscle has the lowest limit (figure 5.2). In addition, thermal hotspots occur most commonly in muscle during medical applications such as hyperthermia and MRI. The magnitude of the safety factor in table 5.3 ranges from 10.9 to 31.2 for localized $psSAR_{10g}$. The lower and upper bounds of the range were obtained for exposure durations of 60 min and 10 min (= typical delay of the thermoregulatory process) using thermoregulated perfusion from the Erasmus MC database, i.e. the reference database in this study. Therefore, the real incorporated safety factor between the functional SAR limits and the basic restrictions

varies significantly depending on the size of thermal hotspot and exposure duration. Table 5.3 also shows the ratio between SAR_{TDFL} and MRI guidelines (as an important guideline for a EMF-based medical application). The results obtained can even be regarded as conservative estimates since we employed the lowest CEM43°C value that has been reported for thermal tissue damage amongst all available data for human and animal species.

We also assessed the sensitivity of the calculated SAR_{TDFL} to exposure parameters, i.e. the size of hotspot, exposure duration and thermal tissue properties for muscle, fat and skin (the tissues where thermal hotspots are most commonly located). Our results show that the size of hotspot has an essential role on the SAR, i.e. the calculated SAR_{TDFL} increases exponentially by decreasing the focus diameter (figure 5.3). The reason for this is the increasing surface-to-volume ratio with decreasing sphere diameter which leads to a stronger dissipation of the generated heat into surrounding tissue and thus a higher required SAR for inducing temperature inside the sphere. In addition, the temperature increases more rapidly in smaller spheres, which leads to a larger $\frac{\partial T}{\partial t}$ in PBE (equation 5.2) and consequently to a higher SAR_{TDFL} value. This finding explains and confirms the higher delivered SAR level of deep hyperthermia treatment in head and neck (H&N) region (75 W/kg) compared to pelvic region (16 W/kg) which is mainly due to smaller size of tumor/target in H&N region[82]. This finding also confirms the relationship between the SAR and tumor size in magnetic nanoparticle hyperthermia reported in Dutz and Hergt[24]. To assess sensitivity of the results to the tissue properties, we used various available tissue property databases. The results show that thermoregulated perfusion under thermal stress significantly raises SAR_{TDFL} compared to basal perfusion at resting condition. In a sphere of 20 cm in muscle, it is a factor of 12.5 fold increase in SAR_{TDFL} (maximum variation). In smaller heating volumes, where the surface-to-volume ratio is big, perfusive effects are almost non-existent, and thus thermal conductivity becomes the primary mechanism of heat transport (figure 5.3). Reduction of exposure duration results in higher thresholds of safe temperature-increase and consequently to a maximum of 10 fold increase in SAR_{TDFL} (figure 5.4).

Comparison of the calculated SAR_{TDFL} values in the current study with the simulated SAR from numerical calculations and experimental investigations in hyperthermia application shows that the calculated results in the current study are consistent with the simulations.

To examine whether our results are in an acceptable range, we investigated whether the calculated SAR_{TDFL} limits in the current study are exceeded by SAR values obtained in medical applications such as hyperthermia treatment and MRI scanning. A retrospective study based on the treatment reports of 35 patients treated with deep hyperthermia in pelvic region, controlled by extensive treatment planning showed that apart from a few outliers, the average SAR level at patient pain complaints (hotspots) appears to be relatively constant at approximately 230 W/kg[9]. The SAR peak volume was around 35 ml for an average patient and covers most SAR peak locations in the patient model. This 35 ml, in the worst case, is equal to an integrated sphere with diameter of 4 cm. The calculated SAR threshold for a sphere of 4 cm diameter in muscle for 60 minutes exposure is 172.9 W/kg. However, the authors stated that the peak SAR volume is distributed over mul-

Table 5.3: Safety factor between functional local SAR limits (SAR_{TDFL}) in muscle and the basic restrictions in the common generic guidelines (ICNIRP [55], IEEE [57]) and also the restrictions in MRI guideline for the first level controlled operation mode (OM) (IEC [56]). The lower and upper bounds of the range of safety factor were obtained for exposure durations of 60 and 10 minutes.

	Basic restrictions (ICNIRP, IEEE): Persons in controlled environments SAR (W/kg)	MRI guideline: First level controlled OM SAR (W/kg)	TD-based Functional limit (current study): SAR_{TDFL} (W/kg)	**Safety factor** (SAR_{TDFL}/ Basic restrictions)	(SAR_{TDFL}/ MRI guideline)
Localized (peak spatial-average)*	10	20	218.4 - 312.3 (sphere = 2.6 cm)	21.8 - 31.2	10.9 - 15.6
Extremities and pinnae**	20	40	218.4 - 312.3 (sphere = 2.6 cm)	10.9 - 15.6	5.4 - 7.8

*Averaged over any 10 g of tissue (defined as a tissue volume in the shape of a cube).
**The extremities are the arms and legs distal from the elbows and knees, respectively.

tiple sub volumes, which are spread over multiple regions, thereby resulting in a higher SAR_{TDFL}. Therefore, depending on how the peak SAR volumes are distributed over the patients body, the calculated SAR_{TDFL} might still be in agreement with the clinical observed maximum. If the hotspot volume would be divided into sub-regions equivalent to spheres with diameters $\leq$2.4 cm, the SAR_{TDFL} thresholds would not be exceeded in the clinic. Furthermore, the absorbed energy in six human models in different Z-positions (head to knees) within a 1.5T bodycoil MRI system, was assessed by performing a detailed simulation study. The results show that local SAR in terms of psSAR10g in the normal and first-level controlled MRI operation mode may exceed the limits as defined in[56] for local transmit coils by more than a factor of three, i.e. reach 120 W/kg[73]. This SAR level was obtained in obese adult models, i.e. in fat tissue. 10g of fat is equal to a sphere of 2.7 cm diameter, for which the calculated SAR_{TDFL} threshold is 255.7 W/kg from 5 minutes RF exposure during MRI exam (Note that only a small part of the MRI exam is devoted to RF exposure and the rest is for scanning). Therefore, the simulated induced SAR during MRI application is well below (by a factor of 2) the calculated SAR threshold which is associated to thermal damage in tissues.
In the current study we had a number of assumptions. Firstly, we assumed a constant temperature over 60 minutes of treatment. It is a conservative approach (worst case) because heating is not expected to be either spatially or temporally constant during the entire hyperthermia session. In case of shorter exposure duration, the temperature and also the calculated SAR will be higher according to the CEM43°C definition 5.2. Secondly, the rate of cell death (R) for temperature below the breakpoint (43(°C)) was assumed to be 1/4 for calculation of thermal dose according to CEM43°C definition. However, there is uncertainty about the slope of the Arrhenius plot below the breakpoint. Most rodent data, however, suggest that the R-value below the breakpoint is between 1/4 and 1/6[20]. We investigated the influence of the R-value on the calculated SAR by performing the thermal dose calculation using R=1/2 (assuming the same value as above the breakpoint) and 1/6 (the lowest reported value for rodent). $|\Delta SAR_{TDfunc\_limit}|$ was obtained by comparing the results using R=1/4 as reference. The result of our investigation shows 2.1% reduction (R=1/6) and 12.1 % (R=1/2) increase in the calculated SAR_{TDFL}, averaged over tissues indicated in Table5.1. Thirdly, no other temperature related effects were considered, for example, change of SAR-distribution due to thermoregulation dependent dielectric parameter. Finally, at diameters of 5 cm and exposure duration of 10 min, a transition zone from basal to thermoregulated properties is present, resulting in more uncertainty in the SAR_{TDFL} at this zone.

5.5 Conclusions

Based on the available data on CEM43°C thermal thresholds for tissue damage, we calculated the safety factor between the established functional SAR limits (SAR_{TDFL}) and the common basic restrictions in ICNIRP and IEEE guidelines for various localized exposure

scenarios. We found that the margin of safety factor for localized SAR averaged over any 10 g of tissue (psSAR_{10g}) is in the range of (10.9 - 31.2), depending on the size of thermal hotspot and exposure duration. The benefit of changing from subjective to objective safety factor is that it facilitates decision making on how much the responsible investigator can increase local SAR exposure with an acceptable risk of thermal damage. Our analysis provides clear indications of functional SAR limit for different exposure scenarios, for instance 150 W/kg in muscle for hyperthermia (60 min exposure and a target of 4 cm in diameter). This value change exponentially with the size of heating volume; hence, the smaller the target is, the higher SAR is needed to induce the same heat. The impact of (delayed) temperature-regulated perfusion is essential and raises SAR limits up to 12.5 fold compared to the value based on basal perfusion in a resting condition. More research on local thermoregulatory and tissue damage processes is therefore of high importance. The current study can form the basis for further discussion on the use of functional localized SAR limits that are more exposure derived than the current generic limits. Such an approach might be beneficial for patients undergoing MRI to detect abnormalities in anatomy. In hyperthermia treatments the calculated limitations have potential to be used for improved control of RF-delivery to reduce the probability of thermal toxicity, while maintaining maximum probability of tumor control.

CHAPTER 6

General discussion and perspectives

6.1 General discussion

The basic restrictions (BRs) on localized exposure to RF EMF have been developed to avoid excessive adverse tissue heating ($< 1°C$) in humans since until now thermal effects are the only established adverse health effect at RF frequency range of EMF exposure[55,57]. These guidelines are currently based on the limited data, e.g. experimental assessments in animals or epidemiological studies using approximated human anatomical models. To account for uncertainties in the data, the BRs are defined by applying large, conservative, safety factors. In this thesis, the quality of the BRs was verified by exploiting the unique opportunity that medical applications provide. The applied fields in medical applications such as hyperthermia treatment of cancer are in general orders of magnitude higher than those defined in the guidelines even for the upper tier, i.e. occupational environment. Therefore, there is a special possibility to establish dose-response relationship for humans exposed to prolonged intense RF EMF during hyperthermia. The results presented in this thesis confirm that the BRs are indeed conservative. Hence, below the exposure limits of the guidelines no adverse effect was noted. Moreover, also no indication of a serious acute effect was observed upon exceeding the guidelines during hyperthermia. This data encouraged us to investigate the possibility of introducing functional SAR limits which are associated to the lowest thermal dose above which thermal tissue damage take place.
This thesis provides knowledge that could contribute to the international ongoing discussion for tailoring the existing BRs based on the human data available for thermal dose thresholds to induce tissue toxicity. The experience obtained during the medical application of tissue heating provides an excellent and unique source of human data on the dose thresholds for thermal damage. Subsequently, the enhanced understanding of the thermal tissue damaging process can be exploited to derive EMF exposure guidelines based on actual functional SAR limits observed in humans, which will enable safe use of diagnostic and therapeutic application of EMF at optimized (higher) SAR levels required in, for instance, high intensity MR imaging.
Within the scope of this thesis, *four* main shortcomings in the development of the localized BRs have been addressed aimed at providing stronger foundations:

1. The BRs have been derived from numerical simulations that approximated the human morphology with generic phantoms. In Chapter 2, we demonstrated that morphology is an important source of uncertainty in RF dosimetric studies. Therefore, dosimetric analysis dealing with RF dose at a specific region in the brain must be based upon the individual morphology.
In order to define general local BRs, it is essential to extend the sample of the selected head models in this thesis to a representative group of anatomies for the general population that covers the full range of personal features such as age, race, weight and head size. An additional valuable use of this data would be to determine the influence of the personal features of individuals on SAR variations which would help, in particular, epidemiological researchers to reduce uncertainty by applying appropriate matching variables between cases and controls. In addition, this research

should be extended for modern mobile phone models and other RF exposure sources, or generic sources such as plane waves.

2. The BRs have been developed based on established thermal effects from animal experiments. Translation of the results from animals to humans is difficult, contributing to a rather unsystematic approach in setting the safety factors. This thesis provides pioneering *human* data on EMF and thermal dose-response relationships in the brain and the eyes, as the most critical organs, when humans are exposed to prolonged intense RF EMF during hyperthermia treatment.
The induced local SAR in tissues during hyperthermia can reach levels of 200-300 W/kg at which a substantial probability exists that thermal tissue damage occurs. Evaluations of acute effects by the common toxicity criteria (CTC) scores revealed no indication of a serious acute effect upon exceeding the BRs (i.e. 10 W/kg) by up to 14 (brain) and 10 (eyes) times. Such rare and initial dose-response data is of great potential value for health and standards agencies to tailor the BRs based on the functional change in humans that is to be prevented and the level of safety to ensure prevention. Expanding upon this data, a unique library of associations between exposure-level and effect-level for human exposure conditions can be created for continuously tailoring the localized BRs. The CTC scores in this thesis were used as quantitative assessment of humans well-being and functional changes after exposure to very high EMF, i.e. subjective complaint scores. Nevertheless, since acute toxicity is scored based on patient responses to physicians, it does not rule out sub-clinical adverse health effects. Therefore, additional research is required to objectively study the more subtle functional changes in a prospective and protocolized way.

3. The BRs are lowered by conservative safety factors which were selected based on informed expert opinion rather than a rigorous quantitative process. The magnitude of safety factor for various localized exposure scenarios and various tissues is unknown. This thesis provides clear guidelines for quantifying the incorporated safety factor for various exposure scenarios and various tissues. In Chapter 5 we showed that in order to arrive at the exposure level of the localized BRs, the functional SAR limits are lowered by large safety factors, i.e. up to 31.2 depending on exposure duration and frequency. The functional SAR limits in this research are calculated using the Pennes bioheat equation based on the lowest thermal dose that leads to tissue damage available in literature for humans and animal species. Incorporation of the thermoregulated perfusion is the most influential parameter for local temperature increase assessment and related thermal tissue damage. More research on local thermoregulatory and tissue damage processes is therefore of high importance. Special attention must be paid on people with disabled or partially dysfunctional perfusion abilities (e.g., the elderly, diabetics) or heat sensation. Experimental validation of the presented results on the functional SAR values is required in future work.

4. The BRs for localized exposure have been originally derived from the established BRs for whole-body exposure[55,57]. The underlying process of this derivation of the loc-

alized BRs in the common guidelines is very weak, lacks details and is unclear. In Chapter 5 this thesis describes that local exposures guidelines should not be derived from whole body exposure guidelines because the size of the applied averaging volume has an essential impact on the SAR limits. This outcome clearly shows the relevance for calculating the functional exposure levels and on the choice of the mathematical model. Since the averaging volume over 10 g of tissue (as defined in the localized BRs) is much smaller than the whole-body volume, the required SAR for inducing the same heating in a tissue is dramatically different in localized versus whole-body exposure. Thus, localized SAR values can be much larger than whole-body SAR not only because of the higher heat tolerance of tissues under localized exposure, but also because of the smaller size of the averaging volume. Therefore, the principles for defining the whole-body BRs cannot be applied as the basis for defining the localized BRs. Moreover, the results of this thesis stress the high impact of the averaging size for the localized BRs, which is a part of an ongoing discussion with respect to 1 gram or 10 gram averaging mass.

6.2 Outlook and Future work

For future safety concepts, we suggest to use thermal dose models rather than SAR limits. Hence, we advise defining limits on the localized peak temperature increase for specified durations of exposure. Such an approach may be challenging due to the complexity and uncertainty in the thermal parameter space. Nevertheless, we believe that having a better surrogate for actual tissue damage outweighs this larger uncertainty and may become more useful in the future than SAR limitations, which have very limited correlation to tissue temperature and tissue damage. In this respect, Chapter 4 shows that there is a larger uncertainty in the linear correlation between SAR and temperature than in temperature assessment. This approach has been applied to some extend in the last version of the magnetic resonance (MR) guidelines IEC[56]: to prevent local tissue damage in the body, the tolerated local tissue temperature rise of the patient is restricted to maximum 40°C by the MR equipment in the first level controlled operating mode. However, there are no guidelines on how to control these limits and also not on exposure duration at 40°C. Compliance to the temperature limits is reached by limiting the SAR. Major problem in temperature assessments is the implementation of the effect of thermoregulation. Special attention should be given to fill the existing gaps in modeling the local tissue thermoregulation, i.e. temperature-dependent blood perfusion and heat conduction models. Improvement of these models requires measurement of thermal data to tune the models to measurements to improve the reliability of predictions. Unfortunately, experimental assessments in humans are rare and usually date back some decades. Recent advances in non-invasive MR thermometry (MRT) provide great opportunities to identify heterogeneities, anisotropies, and temperature dependent tissue properties in various anatomies. Thermal tissue property values can be derived from this data by application of optimization techniques to invasive temperature measurement data of patients treated with

hyperthermia[100]. Obtaining such valuable inter- and intra-individual human data would enable assessment and improvement of the uncertainty of modelling results.
The analysis in this thesis was restricted to macroscopic, i.e. tissue-specific exposure assessments. Various numerical approaches can be used at a microscopic scale to identify and assess possible interaction mechanisms between biological cells and an incident EMF. Although a considerable number of research groups worldwide have worked on the physiological effects of EMF and their influence in the biological response, relatively little is known about the possible interaction mechanisms and the underlying modified biological processes by an incident field. In fact, it is unclear which exposure conditions can trigger a certain positive response and avoid possible damage in cells and tissues. Detailed dosimetry combined with experimental validation is crucial to fill this knowledge gap on the biological explanation of EMF effects. Similarly, rigorous dosimetry is crucial in experimental biological cell exposure studies to report not only the external incident fields to Petri-dishes but also the induced internal, local field strengths, current densities, absorbed energy, and temperature increase to identify the biological interaction with EMF. In recent years, the advance in computer power has provided extraordinary capabilities for the progress of numerical computational simulations to support identification of interaction mechanisms, which are mostly identified by experimental research so far.
The availability of advanced modeling tools suitable to investigate the health effects of RF exposure enables us to define more refined BRs to allow safe and beneficial use of EM. After decades of searching for possible harmful effects, more attention should be paid to explore the potentially beneficial effects of EM exposures on humans and to the development of (medical) applications that take advantage of the well-identified beneficial effects such as bone formation[46,54], wound healing[32,62] and nerve regeneration[18,69].
Investigating "potential" adverse effects of EMF is like searching for a needle in a haystack, while not knowing whether there is a needle in the haystack. It is nearly impossible to find an effect which is not well-identified under un-controlled conditions. Fortunately, EMF-based medical applications such as hyperthermia, MRI and TMS, in which huge number of people are being exposed to high intensity EMF and are monitored by medical experts long time after the exposure, provide the unique opportunity to capture "potential" adverse health effects and to create a very valuable library of human data for tailoring the EM safety guidelines. Therefore, EMF-based medical applications may well be the best field to advance in the tailoring of the BRs by relying on serendipity of experts to at least start looking in the right haystack.

Summary

Exposure to radio-frequency (RF) electromagnetic fields (EMF) is unavoidable in today's modern life. This exposure is growing mainly because of rapid growth in telecommunication systems. Awareness of the possible risks of exposure to EMF has raised public concern. To avoid any potential adverse health effect, international organizations of ICNIRP[55] and IEEE[57] have developed basic restrictions (BRs) on specific absorption rate (SAR) for human exposure to RF EMF. These restrictions were derived based on limited data, i.e. experimental assessments (almost entirely) in animals or dose assessment using generic phantoms (approximated human anatomy). In order to account for uncertainties in the data and to provide a sufficient level of safety, the limits are lowered by large safety factors which were selected based on expert opinion rather than a rigorous quantitative process. The safety factors are not quantified for various exposure scenarios.
In view of the lack of knowledge on the incorporated safety factor, and in the light of unique opportunity that medical applications can provide to establish dose-response relationship for humans, the aim of this thesis is to explore the relevance of the current BRs for functional tissue changes and to tailor SAR limits for localized exposure above which tissue damage takes place. This thesis, by means of advanced simulation tools, shows that the current restrictions on local exposure to RF EMF are conservative and should be more refined based on accurate dosimetry and useful data on experimental assessments in humans.

Chapter 1 starts with a general introduction on the interaction of RF EMF with human tissues and on the established adverse health effects. It describes the basic restrictions and incorporated safety factors in the common guidelines and ends with the outline of this thesis.

Chapter 2 indicates that RF dose calculation in the brain is considerably influenced by head morphology. Therefore, the reported association between the risk for brain tumor induction and the (cumulative) absorbed RF dose in the brain calculated for exposure to a mobile phone to a generic head phantom, as reported in the recent epidemiological Interphone studies, is subject of a large uncertainty (max: 16.8 dB). From the work reported in this chapter it follows that estimation of local absorbed dose in the brain *must* be on the basis of the real morphology and not on generic phantoms in RF dosimetric studies.

In **Chapter 3, 4**, we took the unique advantage of medical applications in applying high EMF on humans to build pioneering quantitative human data on the dose-response relationship in the brain and the eyes, as the most critical organs for the safety guidelines. We analysed the association of high induced EM (brain and eyes) and thermal (eyes) dose with reported acute effects in patients treated with hyperthermia for cancer in the head and neck region. The calculated doses were subsequently related to the recorded functional adverse effects based on the Common Toxicity Criteria (CTC) scores, i.e. a standardized classification of adverse effects used in cancer therapy evaluation. Evaluations of acute effects revealed no indication of a serious acute effect upon exceeding the BRs (i.e. 10

W/kg) by up to 14 (brain) and 10 (eyes) times. At present, human data is very scarce and standards rely almost entirely on much less satisfactory animal experimental data. Such initial human dose-response data is of great potential value for health and standards agencies to tailor the BRs based on the functional change in humans that is to be prevented and the level of safety to ensure prevention.

The basis for the localized BRs is to keep local tissue temperature rises under 1°C in humans. However, thermal tissue damage occurs at much higher thermal doses. Literature values for maximum tolerable thermal doses of various tissues are available[110]. Therefore, in **Chapter 5** we explored how much the SAR limits can be increased before thermal tissue damage occurs. This Chapter provides clear indications of functional SAR limits for various exposure scenarios based on the lowest thermal dose that result in local acute tissue damage available in literature. The calculated safety factor as a ratio between the functional SAR limits and the local BRs can be up to 31.2 depending on the exposure duration and exposure frequency which determines the size of the heated volume. Thermoregulated local perfusion, as the major tissue response to heat, is the most important parameter for RF induced temperature increase assessment. This research presents an approach to establish the guidelines dedicated to a specific exposure scenario, i.e. exposure-specific SAR limits, to improve the functionality of exposure purpose.

All in all, the numerical results obtained in this thesis provide additional support to refine the localized BRs based on the functional change in humans to allow safe and beneficial use of RF EMF. This thesis provides knowledge that contributes to further discussion on the use of functional localized SAR limits that are more exposure derived than the current generic limits.

Samenvatting

In de hedendaagse samenleving is blootstelling aan radiofrequentie (RF) elektromagnetische velden (EMV) is onvermijdelijk. Daarbij neemt de blootstelling nog steeds toe als gevolg van de snelle toename van het telecommunicatie gebruik. De gedwongen blootstelling aan EMV gekoppeld aan onduidelijkheid over het wel of niet bestaan van schadelijke effecten, heeft bij de bevolking geleid (en leidt nog steeds) tot bezorgheid over mogelijke ongewenste gezondheidsrisico's. Om nadelige gevolgen voor de gezondheid te voorkomen, zijn door internationale organisaties (ICNIRPICNIRP[55] en IEEEIEEE[57]) blootstellingsnormen ontwikkeld. Deze zogenoemde basisrestricties (BRs) geven aan hoeveel RF-EMV energie in W/kg door menselijk lichaam geabsorbeerd mag worden en wordt aangegeven als "specic absorption rate"(SAR). De absolute SAR-waarden van de toegestane blootstelling zijn gebaseerd op beperkte experimentele gegevens, die grotendeels verkregen zijn uit experimentele bij dieren of modelberekeningen en metingen met behulp van generieke fantomen. De aldus vastgestelde basisrestricties kennen een grote mate van onzekerheid. Om toch een hoog niveau van betrouwbare veilighed te bieden, worden de limieten verlaagd met grote veiligheidsfactoren, waarbij de grootte van de veiligheidsfactor vooral gebaseerd is op de mening van experts en niet kwantitief is vastgesteld via een rigorous risico analyse. Daarnaast wordt geen onderscheid gemaakt tussen verschillende blootstellingscondities.
Het onderzoek gerapporteerd binnen dit proefschrift gaat in op de unieke kans die medische toepassingen van RF-EMV bieden om de dosis-respons relatie voor de mens vast te stellen, en op basis van deze bij mensen verkregen gegevens een veiligheidsfactor vast te stellen die effectief beschermd, maar niet overbeschermd. In het proefschrift wordt de relevantie van de huidige BRs aan de hand van functionele veranderingen van menselijk weefsel verkend. Daarnaast is voor lokale blootstelling gekeken hoeveel ruimte er bestaat tussen de bestaande SAR limieten en de berekende SAR grenswaarde voor weefselbeschadiging zoals gevonden bij medische toepassing. Het onderzoek binnen dit proefschrift laat zien dat de huidige beperkingen voor lokale blootstelling aan RF-EMV conservatief zijn en meer accuraat en speficifiek kunnen worden, als zij worden gebaseerd op nauwkeurige dosimetrie en analyse van bijwerkingen bij RF-EMV blootstelling van medische toepas-

singen bij de mens.

Hoofdstuk 1 begint met een algemene inleiding over EMV en op de interactie van RF-EMV met het menselijke lichaam en de vastgestelde schadelijke gezondheidseffecten. Het beschrijft de basisrestricties en benoemt de vastgestelde veiligheid factoren zoals vermeldt in de internationale richtlijnen voor blootstelling aan RF-EMV. Het eindigt met indeling van dit proefschrift.

Hoofdstuk 2 laat zien dat RF berekening van de dosis in de hersenen sterk wordt beinvloed door de morfologie van het hoofd. De consequentie van deze bevinding is dat het mogelijk verband tussen geabsorbeerde RF dosis in de hersenen en het risico op inductie van een hersentumor zoals gerapporteerd voor de recente Intercom epidemiologische studies, een hoge mate van onzekerheid kent. De RF-EMV dosis berekend voor een algemene hoofd fantoom bij blootstelling aan een mobiele telefoon en kan tot max 16.8 dB afwijken. Schatting van de lokale geabsorbeerde RF-EMV dosis in de hersenen kan alleen nauwkeurig op basis van de werkelijke morfologie en kan niet bepaald worden met RF dosimetrische onderzoek op generieke fantomen.

In **Hoofdstuk 3, 4** is de toegang die wij hebben tot de medische toepassing van hyperthermie benut om data te analyseren van patienten die blootgesteld zijn aan zeer hoge RF-EMV intentsiteiten voor de behandeling van kanker. Deze patient gegevens bieden een unieke mogelijkheid op kwantitatieve analyse van een mogelijke dosis-responsrelatie in de meest gevoelige organen van een mens, namelijk hersenen en ogen. In de richtlijnen voor veilige blootstellingslimieten worden hersenen en ogen als de meest kritische organen beschouwd. In beide hoofdstukken zijn de gegevens geanalyseerd op een mogelijke correlatie tussen geinduceerde RF-EMV (hersenen en de ogen) en thermische (ogen) dosis met de gerapporteerde acute effect bij patienten tijdens hun behandeling met hyperthermie voor kanker in het hoofd-halsgebied. De berekende doses werden vervolgens gerelateerd aan de geregistreerde functionele nadelige bijwerkingen volgens de Common Toxicity Criteria (CTC) scores, d.w.z. een gestandaardiseerde classificatie waarmee bijwerkingen van een kankerbehandeling wordt geevalueerd. Uit de evaluatie van de verkregen patient gegevens volgde dat de BRs (d.w.z. 10 W/kg) overschreden kan worden tot ten minste een factor 10 (hersenen) dan wel 14 (ogen) Zonder dat een ernstige acute bijwerking (CTC3)werd geconstateerd. Nog steeds zijn gegevens over de dosis-effect relatie bij blootsteling van een mens aan hoge dosis RF-EMV zeer schaars. Dientengevolge zijn alle richtlijnen voor RF-EMV blootstelling bijna volledig gebaseerd dierexperimentele gegevens met de daarbijbehorende onzekerheid. De **Hoofdstuk 3, 4** gerapporteerde initiele dosis-respons gegevens geeft nieuwe inzichten voor de vaststelling van nieuwe op humane gegevens gebaseerde richtlijnen door gezondheidsorganisaties en overheidsagentschappen, waarbij de BRs specifiek kan zijn voor de beoogde functionele veranderingen bij de mens en een effectief niveau van veiligen geboden wordt.

Het doel van de gelokaliseerde BRs is om de lokale weefsel temperatuur stijging te be-

perken tot maximaal 1°C. Echter, uit de beschikbare wetenschappelijk literatuur volgt dat weefselbeschadiging als gevolg van verwarming pas bij een veel hogere thermische dosis ontstaat, en verschild per weefseltype[110]. Daarom is in **Hoofdstuk 5** is een andere benadering voor het bepalen van de SAR-limieten gevolgd. Per weefseltype is de, in de literatuur, laagst gerapporteerde thermische dosis voor lokaal acute weefselschade, vastgesteld. Vervolgens is deze thermisch dosis vertaald naar de maximaal toegestane SAR waarde, waarbij rekening wordt gehouden met de specifieke RF-EMV blootstellingscondities. De uitkomst is dan een functionele SAR limiet die variabel is en afhangt van de precieze blootstellingsduur en de frequentie van het RF-EMV (de frequentie bepaalt de grootte van het verhitte volume). Het onderzoek toont aan dat de op deze wijze berekende functionele SAR limiet tot een factor 31.2 hoger kan zijn dan de SAR limiet bepaalt volgens de conventionele BRs methodiek. Voor het vaststellen van de functionele SAR limiet, is warmte afvoer via de, temperatuur afhankelijke, weefsel doorbloeding, bepalend voor de uiteindelijke temperatuurstijging. Het model van een functionele SAR limiet is een eerste aanzet om richtlijnen voor RF-EMV blootstelling op te stellen die specieke gericht zijn op een toepassing zoals hyperthermie of MRI, dat wil zeggen blootstelling aan specieke SAR limieten vast te stellen, met als doel de functionaliteit van de blootstelling te maximaliseren.

Het onderzoek in dit proefschrift laat zien dat de veiligheidsfactor in de bestaande BRs voor lokale blootstelling weinig specifiek is. Door rekening te houden met de blootstellingsconditie kan de limiet voor de toegestane SAR waarde voor veilig en nuttig gebruik van RF EMV, veel specifieker bepaald worden. Hopenlijk stimuleert dit proefschrift vervolg onderzoek naar functionele gelokaliseerde SAR limieten die meer blootstellings speficiek zijn dan de huidige generieke richtlijnen.

PhD portfolio

List of publications

F Adibzadeh, JF Bakker, MM Paulides, RF Verhaart and GC van Rhoon Impact of Head Morphology on the Local Brain Specific Absorption Rate from Exposure to Mobile Phone Radiation. . *Bioelectromagnetics*, 36(1):66–76 2015.

F Adibzadeh, RF Verhaart, GM Verduijn, V Fortunati, Z Rijn, M Franckena, GC van Rhoon and MM Paulides Association of acute adverse effects with relatively high local induced SAR in the brain from prolonged RF head and neck hyperthermia *Phys Med Biol*, 60:995–1006 2015.

F Adibzadeh, GC van Rhoon, GM Verduijn, NC Naus-Postema and MM Paulides Absence of acute ocular damage in humans after prolonged exposure to intense RF EMF *Phys Med Biol*, 61:488–504 2016.

F Adibzadeh, MM Paulides and GC van Rhoon SAR thresholds for electromagnetic exposure using functional thermal dose limits *Int J Hyperthermia*, submitted.

Presentations at international conferences

F Adibzadeh, JF Bakker, MM Paulides and GC van Rhoon. The impact of anatomical differences on absorbed energy from exposure to mobile phone at different regions in the brain. *34th Annual Meeting of the Bioelectromagnetics Society (BEMS), Brisbane, Australia*, 2012

F Adibzadeh, GM Velde-Verduijn, GC van Rhoon and MM Paulides. Towards accurate dosimetry in organs at risk during deep hyperthermia in Head and Neck region.. *28th Annual Meeting of the European Society for Hyperthermic Oncology (ESHO), Munich, Germany*, 2013

F Adibzadeh, RF Verhaart, V Fortunati, M Franckena, GM Verduijn, GC van Rhoon and MM Paulides. Assessment of the induced SAR in the brain during deep microwave hyperthermia in the head and neck region to investigate the stringency of the basic restrictions.. *36th Annual Meeting of the Bioelectromagnetic Society (BEMS), Cape Town, South Africa*, 2014

RF Verhaart, V Fortunati, F Adibzadeh, GM Verduijn, JF Veenland, T van Walsum, MM Paulides. Patient modelling in head and neck hyperthermia treatment planning: is CT-based auto-segmentation sufficient?. *33th annual meeting of the European Society for Radiotheray & Oncology (ESTRO), Vienna, Austria*, 2014

F. Adibzadeh, GM Verduijn, GC van Rhoon and MM Paulides. Association of maximum SAR exposure in the eyes with acute ocular effects during prolonged RF exposure.. *37th Annual Meeting of the Bioelectromagnetic Society (BEMS), Asilomar, USA*, 2015

F Adibzadeh, GC van Rhoon and MM Paulides. Association of maximum SAR exposure in the eyes with acute ocular effects during prolonged RF exposure.. *the joint URSI-Benelux / IEEE AP-S / NARF symposium, Enschede, Netherlands*, 2015

Honors

Travel grant for the 34th annual meeting of the Bioelectromagnetic Society (BEMS), Brisbane, Australia, 2012

Travel grant for the 36th annual meeting of the Bioelectromagnetic Society (BEMS), Cape town, South Africa, 2014

Travel grant for the 37th annual meeting of the Bioelectromagnetic Society (BEMS), Asilomar, California, USA, 2015

Summary of PhD training and teaching activities

Name PhD student: F. Adibzadeh Erasmus MC Department: Radiation Oncology Research School: Postgraduate School of Molecular Medicine	PhD period: April 2011 - July 2016 Promotor: Prof. dr. G.C. van Rhoon Supervisor: Dr. M.M. Paulides

1. PhD training

	Year	**Workload (Hours/ECTS)**
General courses		
• Biomedical English Writting and Communication	2013	4 ECTS
• Dutch Course	2013	7 weeks
In-depth courses		
• How to deal with magnetic fields at workplace (Utrecht)	2011	14 hrs
• SEMCAD LF solver and modelling ELF coils (Zurich)	2014	50 hrs
Presentations		
• The impact of anatomical differences on the exposure from mobile phone of different regions in brain	2012	
• Towards accurate dosimetry in organs at risk during deep hyperthermia in Head and Neck region	2013	
• Segmentation in Head and neck hyperthermia treatment planning: is CT based auto-segmentation sufficient?	2014	
• Exposure of the brain during deep microwave hyperthermia in the Head and Neck region	2014	
• Association of maximum SAR exposure in the eyes with acute ocular effects during prolonged RF exposure	2015	
International conferences		
• 34th annual meeting of the Bioelectromagnetics Society (BEMS), Brisbane, Australia	2012	
• 28th annual meeting of the European Society for Hyperthermic Oncology (ESHO), Munich, Germany	2013	
• 33th annual meeting of the European Society for Radiotheray & Oncology (ESTRO), Vienna, Austria	2014	
• 36th annual meeting of the Bioelectromagnetics Society (BEMS), Cape town, South Africa	2014	
• 37th annual meeting of the Bioelectromagnetics Society (BEMS), Asilomar, California, USA	2015	

	Year	Workload (Hours/ECTS)
Seminars and workshops		
• KWF Werkgemeenschaps dag Hyperthermie, Amsterdam	2011	1 day
• Monte Verita workshop for 'EMF & Health Risk Research: update'	2012	1 week
• KWF Werkgemeenschaps dag Hyperthermie, Maastricht	2012	1 day
• ZonMw symposium on EMF dosimetry, Den Haag	2013	1 day
• KWF Werkgemeenschaps dag Hyperthermie, Amsterdam	2014	1 day
• Department journal club and werkbespreking	2011-2015	50 hrs
• EMF project meeting	2011-2014	40 hrs
2. Teaching activities		
• Introduction to SEMCAD X, python scripting	2013	6 hrs
• ELF modeling and dosimetry for Transcranial magnetic stimulation (TMS) in SEMCAD X	2013	14 hrs
• Department educational hour on SEMCAD X LF solver	2014	2 hrs
• Introduction to Hyperthermia	2014	2 hrs

Curriculum Vitae

Fatemeh Adibzadeh was born on February 9th, 1984 in Tehran, Iran.

2002-2006 Bachelor of Engineering degree in Biomedical Engineering, Amirkabir University of Technology (Tehran Polythechnic). Thesis: "Fuzzy Control of Servo Motors with FPGA"

2006-2008 Master of Science degree in Biomedical Engineering, Amirkabir University of Technology (Tehran Polythechnic). Thesis: "Combination of Multiple classifiers for lie detection application"

2009-2010 PhD student at Technical University of Eindhoven, Eindhiven. Euphoria project: "Effects of pricing strategies on dynamic repertoires of activity-travel behaviour"

2011-2016 PhD student at Erasmus MC - Daniel den Hoed Cancer Center, Rotterdam. The Netherlands Organisation for Health Research and Development (ZonMw) project: "Electromagnetic Fields and Health"

Dankwoord

About five years ago I started my Ph.D. research at Erasmus MC, University Medical Center Rotterdam (EMC). During these years hyperthermia group in Rotterdam was my second home. I would like to thank all the hyperthermia group members for their support and the knowledge that they share with me. They made my working days educational, pleasant and enjoyable.

I would like to express my sincere gratitude to my promotor Prof. Gerard van Rhoon and my copromotor Dr.ir Maarten Paulides for the continuous support of my research, for their patience, motivation, and knowledge. Their guidance helped me in all the time.

The inner committee members Prof. Roland Kanaar, Prof. Peter Zwamborn and Prof. Alex Burdorf; the plenary committee members Prof Anton Tijhuis, Prof. Saskia Cessie and Prof. Gabriel Krestin; thank you for accepting to be in my doctoral committee and attend to my defence.

My Ph.D. project was carried out in collaboration with Molecular Radiation Biology group at Erasmus MC and Electrmagnetics group at Technical university of Eindhoven (TU/e); Special thanks to Prof Roland Kanaar and Prof. Peter Zwamborn for their dedication to have regular progress meetings and sharing knowledge.

Last but not the least, I would like to thank my family: my parents, my husband and my two children for their cordial mutual understanding and for supporting me spiritually throughout writing this thesis and my life in general. I started my Ph.D. when my daughter was one year old and ended when my son was one year old. So, the completion of this thesis is owed in part to my children finally going to bed! Thank you.

References

1. E.R. Adair and B.W. Adams. Microwaves modify thermoregulatory behavior in squirrel monkey. *Bioelectromagnetics*, 1:1–20, 1980.

2. F. Adibzadeh, R.F. Verhaart, G.M. Verduijn, V. Fortunati, Z. Rijnen, M. Franckena, G.C. van Rhoon, and M.M. Paulides. Association of acute adverse effects with high local SAR induced in the brain from prolonged RF head and neck hyperthermia. *Phys Med Biol*, 60(3):995–1006, 2015.

3. F. Adibzadeh, GC. van Rhoon, GM. Verduijn, NC. Naus-Postema, and MM. Paulides. Absence of acute ocular damage in humans after prolonged exposure to intense RF EMF. . *Phy*, 61(2):488–504, 2016.

4. JS. Allen, H. Damasio, and J. Grabowski. Normal Neuroanatomical Variation in the Human brain: An MRI-volumetric study. *Am J Phys Anthropol*, 118(4):341–58, 2002.

5. J. F. Bakker, M. M. Paulides, E. Neufeld, A. Christ, X. L. Chen, N. Kuster, and GC. van Rhoon. Children and adults exposed to low-frequency magnetic fields at the ICNIRP reference levels: theoretical assessment of the induced electric fields. *Phys Med Biol*, 56(7):49674989, Apr 2011.

6. J.F. Bakker, M.M. Paulides, A. Christ, N. Kuster, and G.C. van Rhoon. Assessment of induced SAR in children exposed to electromagnetic plane waves between 10 MHz and 5.6 GHz. *Phys Med Biol*, 55:3115–3130, 2010.

7. J.G. Bollemeijer, J.J. Lagendijk, J.A. van Best, A.A. de Leeuw, J.L. van Delft, and D. de Wolff-Rouendaal. Effects of microwave-induced hyperthermia on the anterior segment of healthy rabbit eyes. *Graefes Arch Clin Exp Ophthalmol*, 227(3):271–276, 1989.

8. C. Buccella, V. De Santis, and M. Feliziani. Prediction of temperature increase in human eyes due to RF sources. *IEEE Trans. Electromagn. Compat.*, 49:825–832, 2007.

9. R.A.M. Canters, M. Franckena, J. van der Zee, and G.C. van Rhoon. Optimizing deep hyperthermia treatments: are locations of patient pain complaints correlated with modelled SAR peak locations? *Phys Med Biol*, 56:439451, 2011.

10. R.A.M. Canters, M.M. Paulides, M. Franckena, J. W. Mens, and G.C. van Rhoon. Benefit of replacing the Sigma-60 by the Sigma-Eye applicator. *Radiation Oncology Biology Physics*, 189:74–80, 2013.

11. E. Cardis, B. K. Armstrong, J. D. Bowman, G. G. Giles, M. Hours, D. Krewski, M. McBride, M. E. Parent, S. Sadetzki, A. Woodward, J. Brown, A. Chetrit, J. Figuerola, C. Hoffmann, A. Jarus-Hakak, L. Montestruq, L. Nadon, L. Richardson, R. Villegas, and M. Vrijheid. Risk of brain tumours in relation to estimated RF dose from mobile phones: results from five Interphone countries. *Occup Environ Med*, 68:631–640, 2011a.

12. E. Cardis, N. Varsier, J. D. Bowman, I. Deltour, J. Figuerola, S. Mann, M. Moissonnier, M. Taki, P. Vecchia, R. Villegas, M. Vrijheid, K. Wake, and J. Wiart. Estimation of RF energy absorbed in the brain from mobile phones in the Interphone Study. *Occup Environ Med*, 68:686–693, 2011b.

13. A. Christ, M-C. Gosselin, M. Christopoulou, S. Kuhn, and N. Kuster. Age-dependent tissue-specific exposure of cell phone users. *Phys. Med. Biol.*, 55:1767–1783, 2010.

14. A. Christ, M-C. Gosselin, S. Kuhn, and N. Kuster. Impact of Pinna Compression on the RF Absorption in the Heads of Adult and Juvenile Cell Phone Users. *Bioelectromagnetics*, 31:406–412, 2010b.

15. Chris a Cocosco, Alex P Zijdenbos, and Alan C Evans. A fully automatic and robust brain MRI tissue classification method. *Medical image analysis*, 7:513–527, 2003.

16. P. Crespo-Valero, M. Christopoulou, M. Zefferer, A. Christ, P. Achermann, K-S. Nikita, and N. Kuster. Novel methodology to characterize electromagnetic exposure of the brain. *Phys. Med. Biol.*, 56:383–396, 2011.

17. Renske de Boer, Henri a Vrooman, Fedde van der Lijn, Meike W Vernooij, M Arfan Ikram, Aad van der Lugt, Monique M B Breteler, and Wiro J Niessen. White matter lesion extension to automatic brain tissue segmentation on MRI. *NeuroImage*, 45: 1151–1161, 2009.

18. J.A. De Pedro, A.J. Prez-Caballer, J. Dominguez, F. Colla, J. Blanco, and M. Salvado. Pulsed electromagnetic fields induce peripheral nerve regeneration and endplate enzymatic changes. *Bioelectromagnetics*, 26:20–27, 2005.

19. M. W. Dewhirst, B. L. Viglianti, M. Lora-Michiels, M. Hanson, and P. J. Hoopes. Basic principles of thermal dosimetry and thermal thresholds for tissue damage from hyperthermia. *Int J Hyperthermia*, 19:267–294, 2003.

20. M.W. Dewhirst, Z. Vujaskovic, E. Jones, and D. Thrall. Re-setting the biologic rationale for thermal therapy. *Int J Hyperthermia*, 21:779790, 2005.

21. P. J. Dimbylow, A. Hirata, and T. Nagaoka. Intercomparison of whole-body averaged SAR in European and Japanese voxel phantoms. *Phys Med Biol*, 53:5883–5897, 2008.

22. T. Drizdal, P. Togni, L. Visek, and J. Vrba. Comparison of Constant and Temperature Dependent Blood Perfusion in Temperature Prediction for Superficial Hyperthermia. *RADIOENGINEERING*, 19:281–289, 2010.

23. C.H. Durney. *Basic Introduction to Bioelectromagnetics*. CRC Press, 1999. ISBN 0-8493-1198-5.

24. S. Dutz and R. Hergt. Magnetic nanoparticle heating and heat transfer on a microscale: Basic principles, realities and physical limitations of hyperthermia for tumour therapy. *Int J Hyperthermia*, 29 (8):790–800, 2013.

25. J. A. Elder. Ocular effects of radiofrequency energy. *Bioelectromagnetics*, 6:S148–161, 2003.

26. V.M.M. Flyckt, B.W. Raaymakers, and J.J. Lagendijk. Modelling the impact of blood flow on the temperature distribution in the human eye and the orbit: fixed heat transfer coefficients versus the Pennes bioheat model versus discrete blood vessels. *Phys Med Biol*, 51:50075021, 2006.

27. International Agency for Research on Cancer (IARC). Non-ionizing Radiation, Part 2: Radiofrequency Electromagnetic Fields. Volume 102, 2013. IARC monographs on the evaluation of carcinogenic risks to humans.

28. V. Fortunati, R.F. Verhaart, F. van der Lijn, W.J. Niessen, J.F. Veenland, M.M. Paulides, and T. van Walsum. Tissue segmentation of head and neck CT images for treatment planning: a multi-atlas approach combined with intensity modeling. *Medical Physics*, 40:071905–1–14, 2013.

29. V. Fortunati, R. F. Verhaart, F. Angeloni, A. van der Lugt, W. J. Niessen, J.F. Veenland, M. M. Paulides, and T. van Walsum. Feasibility of multi-modal deformable registration for head and neck tumor treatment planning. *Int. J. Radiation Oncology Biol. Phys*, In press, 2014.

30. K. R. Foster and J. J. Morrissey. Thermal aspects of exposure to radiofrequency energy: report of a workshop. *Int J Hyperthermia*, 27:307–319, 2011.

31. M. Franckena, R. Canters, F. Termorshuizen, J.V.D. Zee, and G. van Rhoon. Clinical implementation of hyperthermia treatment planning guided steering: a cross over trial to assess its current contribution to treatment quality. *Int J Hyperthermia*, 26: 145–157, 2010.

32. R. Funk, T. Monsees, and O. zkucur. Electromagnetic effects: From cell biology to medicine. *Progress in Histochemistry and Cytochemistry*, 43:177–264, 2009.

33. C. Gabriel, S. Gabriel, and E. Corthout. The dielectric properties of biological tissues: I. Literature survey. *Phys. Med. Biol.*, 41:2231–49, 1996a.

34. S. Gabriel, R.W. Lau, and C. Gabriel. The dielectric properties of biological tissues: II. Measurements in the frequency range 10 Hz to 20 GHz. *Phys Med Biol*, 41: 22512269, 1996.

35. S. Gabriel, R.W. Lau, and C. Gabriel. The dielectric properties of biological tissues: III. parametric models for the dielectric spectrum of tissues. *Phys Med Biol*, 41: 2271–2293, 1996.

36. S. Gabriel, R-W. Lau, and C. Gabriel. The dielectric properties of biological tissues: II. Measurements in the frequency range 10 Hz to 20 GHz. *Phys. Med. Biol.*, 41: 2251–69, 1996b.

37. S. Gabriel, R-W. Lau, and C. Gabriel. The dielectric properties of biological tissues: III. Parametric models for the dielectric spectrum of tissues. *Phys. Med. Biol.*, 41: 2271–93, 1996c.

38. O.P. Gandhi, K. Sedigh, G.S. Beck, and E.L. Hunt. Distribution of Electromagnetic Energy Deposition in Models of Man with Frequencies near Resonance. *Biological Effects of Electromagnetic Waves*, 2:44–67, 1976.

39. A. Ghanmi, N. Varsier, A. Hadjem, Y. Pinto, E. Conil, A. Gati, O. Picon, and J. Wiart. Statistical Analysis of the influence of the position of a phone on the exposure of brain tissues. *33rd Annual Meeting of the Bioelectromagnetic Society, Jun 12 - 17, 2011, Halifax, Canada*, 2011.

40. M. C. Gosselin, S. Kuhn, P. Crespo-Valero, E. Cherubini, M. Zefferer, A. Christ, and N. Kuster. Estimation of Head Tissue-Specific Exposure From Mobile Phones Based on Measurements in the Homogeneous SAM Head. *Bioelectromagnetics*, 32: 493–505, 2011.

41. M. C. Gosselin, S. Kuhn, A. Christ, M. Zefferer, E. Cherubini, J. F. Bakker, G. C. van Rhoon, and N. Kuster. Experimental Evaluation of the SAR Induced in Head Phantoms of Three- and Eight-Year-Old Children. *The Institude of Electronics, Information and Communication Engineers*, E95-B:3215–3223, 2012.

42. A. Guy. Quantification of Induced Electromagnetic Field Patterns in Tissue and Associated Biological Effects. *Biologic Effects and Health Hazards of Microwave Radiation*, Czerski, P., Ed.; Polish Medical Publisher, Warsaw:203–216, 1974.

43. A.W. Guy and C.K Chou. ELECTROMAGNETIC HEATING FOR THERAPY. Technical report, University of Washington, 1983.

44. A.W. Guy, C.K. Chou, and B. Neuhaus. Average SAR and SAR Distribution in Man Exposed to 450 MHz Radio-frequency Radiation. *IEEE Transactions on Microwave Theory and Techniques*, 32(8):752–763, 1984.

45. A.W.L J. C. Guy, P.O. Kramar, and A.F. Emery. Effect of 2450-Mhz Radiation on the Rabbit Eye. . *IEEE Transactions on Microwave Theory and Techniques*, 23(6): 492–498, 1975.

46. J. Haddad, A. Obolensky, and P. Shinnick. The biological effects and therapeutic mechanism of action of electric and electromagnetic field stimulatation on bone and cartilage: New findings and a review of earlier work. *The Journal of Alternative and Complementary Medicine*, 13:485–490, 2007.

47. J.W. Hand, Y. Li, and J.V. Hajnal. Numerical study of RF exposure and the resulting temperature rise in the foetus during a magnetic resonance procedure. *Phys Med Biol*, 55:913–930, 2010.

48. P.A. Hasgall, E. Neufeld, M.C. Gosselin, A. Klingenbck, and N. Kuster. ITIS Database for thermal and electromagnetic parameters of biological tissues. www.itis.ethz.ch/database, 2012. Version 2.2.

49. P.A. Hasgall, E. Neufeld, M.C. Gosselin, A. Klingenbck, and N. Kuster. ITIS Database for thermal and electromagnetic parameters of biological tissues. www.itis.ethz.ch/database, 2015. Version 3.0.

50. A. Hirata. Temperature increase in human eyes due to near field-field and far-field exposures at 900 MHz, 1.5 GHz, and 1.9 GHz. *IEEE Trans. Electromagn. Compat.*, 47:6876, 2005.

51. A. Hirata, S. Matsuyama, and T. Shiozawa. Temperature rises in the human eye exposed to EM waves in the frequency range 0.66 GHz. *IEEE Trans. Electromagn. Compat*, 42:386393, 2000a.

52. A. Hirata, G. Ushio, and T. Shiozawa. Calculation of temperature rises in the human eye exposed to EM waves in the ISM frequency bands. *IEICE Trans. Commun.*, E 83-B:541548, 2000b.

53. A. Hirata, K. Caputa, T. W. Dawson, and M. A. Stuchly. Dosimetry in models of child and adult for low-frequency electric field. *IEEE Trans. Biomed. Eng.*, 48: 1007–1012, 2001.

54. S. Hwang, J. Song, T. Cho, Y. Song, T. Lee, S. Choung, J. Jang, I. Kim, and J. Kim. Enhanced bone formation around dental implant using electrical stimulation, , pp. 11 12, 2008. In *Bioengineering Conference, 2007. NEBC 07. IEEE 33rd Annual Northeast*, 2008.

55. ICNIRP. Guidelines for limiting exposure to time-varying electric, magnetic, and electromagnetic fields (up to 300 GHz). *Health Phys.*, 74:494–522, 1998.

56. International Electrotechnical Commission. IEC. International standard, Medical equipment IEC 60601-2-33: particular requirements for the safety of Magnetic resonance equipment, 3rd edition; Geneva: IEC, 2010.

57. IEEE. Standard for safety levels with respect to human exposure to radio frequency electromagnetic fields, 3 kHz to 300 GHz, Std C95.1, 2005.

58. IEEE/IEC62704-1. Recommended Practice for Determining the Peak Spatial-Average Specific Absorption Rate (SAR) in the Human Body from Wireless Communications Devices, 30MHz-6 GHz: General Requirements for using the Finite Difference Time Domain (FDTD) Method for SAR Calculations, Draft. *general Technical Report IEEE*, 2011.

59. R.D. Issels, L.H. Lindner, J. Verweij, P. Wust, P. Reichardt, B.C. Schem, S. Abdel-Rahman, S. Daugaard, C. Salat, C.M. Wendtner, Z. Vujaskovic, R. Wessalowski, K.W. Jauch, H.R. Drr, F. Ploner, A. Baur-Melnyk, U. Mansmann, W. Hiddemann, J.Y. Blay, P. Hohenberger, European Organisation for Research, Treatment of Cancer Soft Tissue, Bone Sarcoma Group (EORTC-STBSG), and European Society for Hyperthermic Oncology (ESHO). Neo-adjuvant chemotherapy alone or with regional hyperthermia for localised high-risk soft-tissue sarcoma: a randomised phase 3 multicentre study. *Lancet Oncol.*, 11:561–570, 2010.

60. W. Kainz, A. Christ, T. Kellom, S. Seidman, N. Nikoloski, B. Beard, and N. Kuster. Dosimetric comparison of the specific anthropomorphic mannequin (SAM) to 14 anatomical head models using a novel definition for the mobile phone positioning. *Phys. Med. Biol.*, 50:3423–3445, 2005.

61. A. Karampatzakis and T. Samaras. Numerical model of heat transfer in the human eye with consideration of fluid dynamics of the aqueous humour. *Phys Med Biol*, 55: 56535665, 2010.

62. L. Kloth. Electrical stimulation for wound healing: A review of evidence from in vitro studies, animal experiments, and clinical trials. *Lower Extremity Wounds*, 4: 23–44, 2005.

63. P. O. Kramar, A. F. Emery, A. W Guy, and J. C. Lin. The ocular effects of microwaves on hypothermic rabbits: a study of microwave cataractogenic mechanisms. *Ann N Y Acad Sci.*, 28;247:155–165, 1975.

64. I. Laakso and A. Hirata. Dominant factors affecting temperature rise in simulations of human thermoregulation during RF exposure. *Phys Med Biol*, 56:74497471, 2011.

65. J.J. Lagendijk. A microwave heating technique for the hyperthermic treatment of tumours in the eye, especially retinoblastoma. *Phys Med Biol*, 27(11):1313–1324, 1982.

66. S. Lajavaara, R. Mantyla, T. Salminen, H. Haapasalo, J. Raitanen, J. Jaaskelainen, and A. Auvinen. Incidence of gliomas by anatomic location. *Neuro-Oncology*, 9: 319–325, 2007.

67. J.L. Lancaster, M.G. Woldorff, L.M. Parsons, M. Liotti, C.S. Freitas, L. Rainey, P.V. Kochunov, D. Nickerson, S.A. Mikiten, and P.T. Fox. Automated Talairach atlas labels for functional brain mapping. *Hum. Brain Mapp*, 10:120–31, 2000.

68. J Lang, B Erdmann, and M Seebass. Impact of nonlinear heat transfer on temperature control in regional hyperthermia. *IEEE Trans Biomed Eng*, 46(9):1129–1138, 1999.

69. M. Levin. Bioelectric mechanisms in regeneration: Unique aspects and future perspectives. *Seminars in Cell & Developmental Biology*, 20:543–556, 2009.

70. J. C. Lin. Telecommunications Health and Safety: Cataracts and Cell Phone Radiation. *IEEE Antennas and Propagation Magazine*, 45(1):171–174, 2003.

71. R. L. Magin, R. P. Liburdy, and B. Persson. Biological effects and safety aspects of nuclear magnetic resonance imaging and spectroscopy. *Ann N Y Acad Sci.*, 649: 1–398, 1992.

72. R.L. McIntosh and V. Anderson. Comprehensive tissue properties database provided for the ther-mal assessment of a human at rest. *Biophys Rev Lett*, 5:129–151, 2010.

73. M. Murbach, E. Neufeld, W. Kainz, K.P. Pruessmann, and N. Kuster. Whole-Body and Local RF Absorption in Human Models as a Function of Anatomy and Position within 1.5T MR Body Coil. *Magnetic Resonance in Medicine*, 71:839845, 2013.

74. M. Murbach, E. Neufeld, M. Capstick, W. Kainz, D. Brunner, T. Samaras, K. Prssmann, and N. Kuster. Thermal Tissue Damage Model Analyzed for Different Whole-Body SAR and Scan Durations for Standard MR Body Coils. *Magnetic Resonance in Medicine*, 71(1):421–431, 2014.

75. T. Nagaoka, E. Kunieda, and S. Watanabe. Proportion-corrected scaled voxel models for Japanese children and their application to the numerical dosimetry of specific absorption rate for frequencies from 30 MHz to 3 GHz. *Phys Med Biol*, 53:6695–6711, 2008.

76. American Conference of Government Industrial Hygienists. Threshold limit values for chemical substances and physical agents and biological exposure indices. *Cincinnati, OH: American Conference of Governmental Industrial Hygienists*, 1996.

77. M. Paulides, Bakker J. F., and van Rhoon G. C. Electromagnetic head-and-neck hyperthermia applicator: experimental phantom verification and FDTD model. *Int. J. Radiation Oncology Biol. Phys*, 68:612–620, 2007b.

78. M. M. Paulides, J. F. Bakker, E. Neufeld, J. van der Zee, P. P. Jansen, P. C. Levendag, and G. C. van Rhoon. The HYPERcollar: a novel applicator for hyperthermia in the head and neck. *Int J Hyperthermia*, 23(7):567–576, 2007a.

79. M. M. Paulides, J. F. Bakker, M. Linthorst, J. van der Zee, Z. Rijnen, E. Neufeld, Pattynama P.M.T., P.P. Jansen, Levendag P.C., and G. C. van Rhoon. The clinical feasibility of deep hyperthermia treatment in the head and neck: new challenges for positioning and temperature measurement. *Phys Med Biol*, 55:2465–2480, 2010.

80. M. M. Paulides, P. R. Stauffer, E. Neufeld, P. F. Maccarini, A. Kyriakou, Canters RAM., Diederich C. J., Bakker J. F., and van Rhoon G. C. Simulation techniques in hyperthermia treatment planning. *Int J Hyperthermia*, 29:346–357, 2013.

81. M.M. Paulides, Z. Rijnen, P. Togni, R.F. Verhaart, T. Drizdal, D. de Jong, M. Franckena, G.M. Verduijn, and G.C. Van Rhoon. Clinical Introduction of Novel Microwave Hyperthermia Technology: the HYPERcollar3D Applicator for Head and Neck Hyperthermia. In *EuCAP'2015: The 9th European Conference on Antennas and Propagation (Lisbon, Portugal)*, 2015.

82. M.M Paulides, G. Verduijn, and N. Van Holthe. Status quo and directions in deep head and neck hyperthermia. *Radiat Oncol.*, 11:21, 2016.

83. H.H Pennes. Analysis of tissue and arterial blood temperatures in the resting human forearm. *J Appl Physiol*, 1:93–122, 1948.

84. A. Poston. Static adult human physical characteristics of the adult head. *Department of Defense Human Factors Engineering Technical Advisory Group (DOD-HDBK-743A)*, pages 72–75, 2000.

85. Z. Rijnen, J. F. Bakker, RAM. Canters, P. Togni, G. M. Verduijn, P.C. Levendag, and et al. Clinical integration of software tool VEDO for adaptive and quantitative application of phased array hyperthermia in the head and neck. *Int J Hyperthermia*, 29:181–193., 2013.

86. Z. Rijnen, G.M. Verduijn, P. Togni, R.F. Verhaart, G.C. van Rhoon, and M.M. Paulides. Are effective perfusion and SAR requirements tumor-type specific? reconstruction from measured temperatures during head and neck hyperthermia. *Phys Med Biol*, Submitted, 2014.

87. R. Roemer, A. Fletcher, and T. Cetas. Obtaining local SAR and blood perfusion data from temperature measurements: steady state and transient techniques compared. *Int J Radiat Oncol Biol Phys*, 11:1539–1550, 1985.

88. SCENIHR. Potential health effects of exposure to electromagnetic fields (EMF), January 2015. Doi: 10.2772/75635.

89. A.R. Sheppard, M.L. Swicord, and Q. Balzano. Quantitative evaluations of mechanisms of radiofrequency interactions with biological molecules and processes. *Health Phys.*, 95(4):365–396, 2008.

90. C.H.W. Song, A. Lokshina, J.G. Rhee, M. Patten, and S.H. Levitt. Implication of blood flow in hyperthermia treatment of tumours. *IEEE Trans. Biomed. Eng.*, 31: 9–16, 1984.

91. G. Sreenivasa, J. Gellermann, B. Rau, and et al. Clinical use of the hyperthermia treatment planning system HyperPlan to predict effectiveness and toxicity. *Int J Radiat Oncol Biol Phys*, 55:407 419, 2003.

92. J.A.J. Stolwijk. Mathematical models of thermal regulation. *Ann N Y Acad Sci.*, 335:98106, 1980.

93. T. Takebayashi, N. Varsier, and Y. Kikuchi. Mobile phone use, exposure to radiofrequency electromagnetic field, and brain tumor: a case-control study. *Br J Cancer*, 98:652–9, 2008.

94. B.N. Taylor and C.E. Kuyatt. Guidelines for Evaluating and Expressing the Uncertainty of NIST Measurement Results. *National Institute of Standards and Technology*, Tech. Note 1297, 1994.

95. P. Togni, Z. Rijnen, W. C .M. Numan, R. F. Verhaart, Bakker J. F., van Rhoon G. C., and M. M. Paulides. Electromagnetic redesign of the HYPERcollar applicator: toward improved deep local head-and-neck hyperthermia. *Phys Med Biol*, 58:5997–6009, 2013.

96. J. van der Zee, M. De Bruijne, J. W. Mens, and et al. Reirradiation combined with hyperthermia in breast cancer recurrences: overview of experience in Erasmus MC. *Int J Hyperthermia*, 26:638–648, 2010.

97. G.C. van Rhoon, T. Samaras, P.S. Yarmolenko, M.W. Dewhirst, E. Neufeld, and N. Kuster. CEM43C thermal dose thresholds: a potential guide for magnetic resonance radiofrequency exposure levels? *Eur Radiol*, 23(8):2215–27, 2013.

98. R. F. Verhaart, V. Fortunati, T. van Walsum, J. F. Veenland, A. van der Lugt, G. C. van Rhoon, W. J. Niessen, and M. M. Paulides. Accurate Patient Modeling for Planning-Guided Deep Head and Neck Hyperthermia: Variation in Tissue Delineation. *16th Molecular Medicine Day, February 29, 2012, Rotterdam, The Netherlands*, 2012.

99. R. F. Verhaart, V. Fortunati, G. M. Verduijn, T. van Walsum, J. F. Veenland, and M. M. Paulides. CT-Based Patient Modelling for Head and Neck Hyperthermia Treatment Planning: Manual versus Automatic Normal-Tissue-Segmenation. *Radiotherapy and Oncology*, 111:158–163, 2014a.

100. R. F. Verhaart, Z. Rijnen, V. Fortunati, G. M. Verduijn, T. van Walsum, J. F. Veenland, and M. M. Paulides. Temperature simulations in head and neck hyperthermia treatment planning: a rigorous tissue property optimization. *Radiation Oncology Biology Physics*, 190(12):1117–24, 2014b.

101. R. F. Verhaart, G. M. Verduijn, V. Fortunati, Z. Rijnen, T. van Walsum, J. F. Veenland, and M. M. Paulides. Accurate 3D temperature dosimetry during hyperthermia therapy by combining invasive measurements and patient-specific simulations. *Int J Hyperthermia*, 31(6):686–92, 2015.

102. G. Vermeeren, M. C. Gosselin, S. Khn, V. Kellerman, A. Hadjem, A. Gati, W. Joseph, J. Wiart, F. Meyer, N. Kuster, and L. Martens. The influence of the reflective environment on the absorption of a human male exposed to representative base station antennas from 300 MHz to 5 GHz. *Phys Med Biol*, 55:5541–5555, 2010.

103. F. Waterman and L. Tupchong. Blood flow in human tumors during local hyperthermia. *Int J Radiat Oncol Biol Phys*, 20:1255–1262, 1991.

104. R. Wessalowski, D.T. Schneider, O. Mils, V. Friemann, O. Kyrillopoulou, J. Schaper, C. Matuschek, K. Rothe, I. Leuschner, R. Willers, S. Schnberger, U. Gbel, G. Calaminus, and MAKEI study group. Regional deep hyperthermia for salvage treatment of children and adolescents with refractory or recurrent non-testicular malignant germ-cell tumours: an open-label, non-randomised, single-institution, phase 2 study. *Lancet Oncol.*, 14:843–852, 2013.

105. J. Wiart, A. Hadjem, M. F. Wong, and I. Bloch. Analysis of RF exposure in the head tissues of children and adults. *Phys. Med. Biol.*, 53:3681–3695, 2008.

106. Hoffmann W van de Lindt T. Winter L, Oezerdem C, J. Periquito, Y. Ji, P. Ghadjar, V. Budach, P. Wust, and T. Niendorf. Thermal magnetic resonance: physics considerations and electromagnetic field simulations up to 23.5 Tesla (1GHz). . *Radiation Oncology*, 10:201, 2015.

107. P. Wust, H. Stahl, J. Loffel, M. Seebass, H. Riess, and R. Felix. Clinical, physiological and anatomical determinants for radiofrequency hyperthermia. *Int J Hyperthermia*, 11:151167, 1995.

108. P Wust, M Seebass, J Nadobny, P Deuflhard, G Moenich, and R Felix. Simulation studies promote technological development of radiofrequency phased array hyperthermia. *Int J Hyperthermia*, 12:477–494, 1996.

109. Blystoen C Elmore S Foster P Hooth M Kissling G Malarkey D Sills R Stout M et al Wyde M, Cesta M. Report of partial findings from the National Toxicology Program carcinogenesis studies of cell phone radiofrequency radiation in Hsd: Sprague Dawley SD rats (whole body exposure). *bioRxiv*, doi: http://dx.doi.org/10.1101/055699, 2016.

110. P. S. Yarmolenko, E. J. Moon, C. Landon, A. Manzoor, D. W. Hochman, B. L. Viglianti, and M. W. Dewhirst. Thresholds for thermal damage to normal tissues: an update. *Int J Hyperthermia*, 26:1–26, 2011.